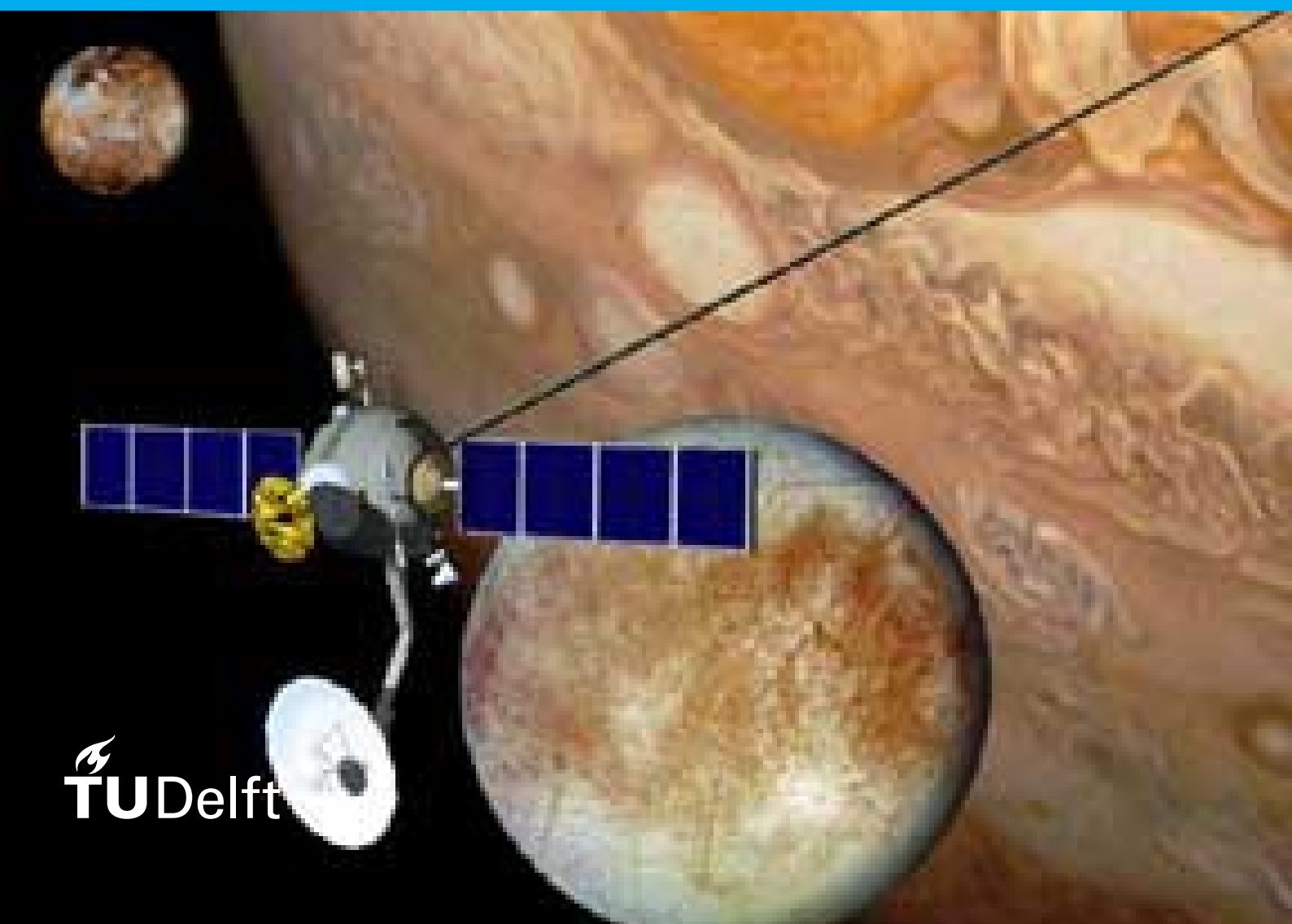# Electrodynamic Tethers For Deep Space Missions

A Feasibility Study

Matthew Turnock

Electrodynamic Tethers
For Deep Space Missions

A Feasibility Study

by

Matthew Turnock

Spaceflight Track, MSc Aerospace Engineering

Student number: 4430913
July 23, 2021
Version 1.1

TUDelft

Summary

As efforts to understand space and the wider universe continue to advance, it is also necessary for spacecraft to be sent to further reaches of the Solar System and beyond, in order to make measurements that cannot be done from (the vicinity of) Earth. With current technology, it has been found that the feasibility of long-term adaptable exploration missions at the far reaches of the Solar System and beyond is limited, as chemical propulsion systems simply do not have the required performance, spacecraft using high-power electric propulsion systems such as ion drives struggle to provide the required energy at long Solar distances, and other novel systems such as Solar sails are also ineffective at long Solar distances.

Electrodynamic tether (EDT) propulsion methods may provide a viable alternative to such ineffective systems, utilising either the interplanetary magnetic field (IMF) generated by the Sun, or even the interstellar magnetic field (ISMF) which is present beyond the Solar System, to provide propellantless yet continuous thrust. The primary reason to explore the use of the IMF as a means of propulsion at extreme Solar distances, is that IMF strength decays linearly with Solar distance, whereas both Solar radiation and gravity decay with the square of Solar distance; meaning it could be possible to achieve good thrust at extreme distances when compared to other propulsion means.

The objective of this research is to assess the feasibility of an EDT propulsion system, applied to deep space missions, which can be summed up in the following research questions:

What is the feasibility of electrodynamic space tethers as a means of propulsion applied to possible future interplanetary and/or interstellar missions? Also what is the viability of a transient-current solution for the electrodynamic tether?

The research questions were assessed by creating a simulation environment using the Tudat toolbox, into which several different EDT configuration and mission profile concepts were applied, to determine which (if any) combinations of concepts would provide a feasible solution. It was found that the best-case EDT utilises a bare-tether current generation concept, has a mass of 1412 kg with an operating current of 305 mA. Overall, the application of an EDT to deep space propulsion has significant limitations to overcome, providing spacecraft accelerations in the 1 nm/s^2 range at 1 AU, causing a maximum change in aphelion height over a 100 year simulation period of only 0.0001 AU, for SSO+ and InO mission profiles. The system has similar performance limitations when applied at further Solar ranges, with the SOKGA mission profile, providing a mission time of flight improvement of only 45 days over a journey of around 30 years.

Preface

This report represents the culmination of my Master thesis in Aerospace Engineering at TU Delft. It has been a long journey and I have learned a lot over this period, for which a number of people are responsible.

First and foremost I would like to thank my thesis supervisor Ron Noomen for his support both during this project and my time at TU Delft generally, without his enthusiasm and advice I would not be in the position I am today. I would also like to thank the other staff and students of space exploration at TU Delft and in particular Dominic Dirkx and Erwin Mooij for introducing me to (and helping wrap my head around) the Tudat software toolbox, which provided the basis for this entire thesis project.

The past year or so working on my thesis has been a challenge, but an enjoyable one; even while dealing with delays and setbacks due to both Covid and personal circumstances, which caused the average number of days I was able to work on the project to be approximately halved. It is for this reason I would finally like to thank all my friends and family for their support and companionship.

M. Turnock
Delft, July 2021

Contents

Nomenclature

List of Abbreviations

AOP	Argument Of Perihelion
Ap	Aphelion
AU	Astronomical Unit
CHB	Composite Hoytether Bare (tether)
CHTr	Composite Hoytether Transitional (tether)
DE	Differential Evolution
DP	Dormand-Prince
ED	ElectroDynamic
EDT	ElectroDynamic Tether
GA	Gravity Assist
HI	Heliospheric Interface
IM	Interstellar Medium
IMF	Interplanetary Magnetic Field
InO	Inner Solar System Out
ISMF	InterStellar Magnetic Field
ISS	International Space Station
LEO	Low Earth Orbit
MAST	Multi-Application Survivable Tether
MOEAD	Multi Objective Differential Evolution
NASA	National Aeronautics and Space Administration
NRL	Naval Research Laboratory
OEDIPUS	Observations of Electric-field Distribution in the Ionospheric Plasma - a Unique Strategy
OML	Orbital-Motion-Limited
Pe	Perihelion
PMG	Plasma Motor Generator
PROPEL	PROPulsion using ELectrodynamics
RK	Runge-Kutta
RTG	Radioisostope Thermolectric Generator
SEDS	Small Expendable Deployer System
SLS	Space Launch System
SOI	Sphere Of Influence
SOKGA	Straight Out with Kickstage and Gravity Assist
SRP	Solar Radiation Pressure
SSO	Simple-Straight-Out
STARS	Space Tethered Autonomous Robotic Satellite
TiPS	Tether Physics and Survivability
T-REX	Tether technologies Rocket EXperiment
TOF	Time Of Flight
TRL	Technology Readiness Level

TSS		Tethered Satellite System

List of Symbols

Latin Symbols

A	[m^2]	(Cross sectional) Area
a	[m]	Primary line separation
a_x	[T]	Sinusoidal amplitude fitting parameter
$\mathbf{B}$	[T]	Magnetic field vector
B_0	[T]	Reference magnetic field strength
B_R	[T]	Radial component of magnetic field
$B_{R,0}$	[T]	Reference radial component of magnetic field
B_ϕ	[T]	Azimuthal component of magnetic field
$B_{\phi,0}$	[T]	Reference azimuthal component of magnetic field
B_z	[T]	Z-component of magnetic field
b_x	[T]	Sinusoidal frequency fitting parameter
c_x	[T]	Sinusoidal phase shift fitting parameter
D	[m]	Tether diameter
DV	[m/s]	Change in spacecraft velocity
d	[T]	Sinusoidal displacement fitting parameter
E_m	[V]	Motional electromotive potential difference
e	[C]	Electron charge
$\mathbf{F}$	[N]	Lorentz force vector
F_g	[N]	Gravitational force
F_t	[N]	Tether (average) tension force
G	[m^3/kgs^2]	Universal gravitational constant
g	[m/s^2]	Gravitational acceleration
h	[-]	Number of Hoytether segments
h_t	[m]	Tape tether height
i	[-]	Dimensionless current
$\mathbf{I}$	[A]	Current vector
I	[A]	Current
I_0	[A]	Unit EDT current
k_a	[-]	Primary line separation ratio
k_A	[-]	Tether area ratio (primary)
$k_{A,s}$	[-]	Secondary tether area ratio
k_{l_p}	[-]	Primary segment length ratio
k_{occ}	[-]	Occultation coefficient
k_{rad}	[-]	Radiation coefficient
k_{rot}	[-]	SRP rotation coefficient
k_s	[-]	Slack coefficient
$k_{T,rot}$	[-]	Tether thrust correction coefficient for rotation
L	[m]	Length of EDT
L_0	[m]	Unit EDT length
L_p	[m]	Total length of primary lines

L_s	[m]	Total length of secondary lines
$\mathbf{1}$	[m]	Unit vector along tether length
l	[m]	Position along length of EDT
l_p	[m]	Primary segment length
l_s	[m]	Secondary segment length
M	[kg]	Mass of central or third body
m	[-]	Number of secondary links
m_1	[kg]	Mass of body 1
m_2	[kg]	Mass of body 2
m_E	[kg]	Electron mass
m_e	[kg]	Endmass (individual)
m_p	[kg]	Total primary line mass
m_s	[kg]	Total secondary line mass
m_{tot}	[kg]	Total vehicle mass
m_t	[kg]	Tether mass
n	[-]	Total number of primary lines
n_l	[-]	Number of primary links
n_∞	[m^{-3}]	Unperturbed plasma density
R	[m]	Radius from central body
R_0	[m]	Reference Solar distance
r	[m]	Radius from central body
s	[m]	Distance along the EDT
T	[s]	Period
T_t	[s]	Tether rotational period
t	[s]	Time
V_0	[V]	Unit EDT voltage
V_P	[V]	Motion induced voltage
V_p	[m^3]	Total primary line volume
$\mathbf{V_{rel}}$	[m/s]	Spacecraft relative velocity vector
V_p	[m^3]	Total secondary line volume
V_t	[V]	EDT voltage due to ohmic loss
V_{SW}	[m/s]	Solar wind speed
w	[m]	Tape tether width

Greek Symbols

β	[rad]	Heliocentric ecliptic latitude
β_∞	[rad]	Heliocentric ecliptic latitude of the ISMF
ΔV	[V]	Potential bias
ϵ	[-]	Dimensionless tether length
λ	[rad]	Heliocentric ecliptic longitude
λ	[-]	Unit voltage
λ_∞	[rad]	Heliocentric ecliptic longitude of the ISMF
ρ	[kg/m^3]	Mass density
ρ_p	[kg/m^3]	Composite primary line density
ρ_r	[Ωm]	Resistivity
ρ_s	[kg/m^3]	Composite secondary line density
ϕ	[rad]	Magnetic field azimuth angle
ϕ_0	[rad]	Reference magnetic field azimuth

σ	[S/m]	Tether conductivity
ω_t	[rad/s]	EDT angular velocity

1

Introduction

For decades, tethers have been present in the space industry, dating all the way back to NASA's Gemini programme [12]. More recently however, the electrodynamic tether (EDT) has been employed to utilise magnetic fields in space to provide spacecraft with both power generation [38], and (near) propellantless propulsion opportunities [25]. A brief summary of the history of EDT development, missions and paper studies can be seen in Table 1.1, which takes heavily from the historic analysis conducted in the literature study which preceeds this thesis report, which should be referred to for a more in-depth analysis of the history of EDTs [46].

Table 1.1: Summary of EDT missions, including historical, planned, and paper studies. The mission goals for each are also specified [46].

Mission	(Planned) Launch Date	Mission Goals
TSS-1 and TSS-1R (NASA) [42]	1992 and 1996	Technology demonstrators (general tether)
SEDS-I and SEDS-II (NASA) [27] [4]	1993 and 1994	Technology demonstrators (general tether)
PMG (NASA) [19]	1993	Technology demonstrators (ED tether)
OEDIPUS (NASA) [4]	1995	Scientific experimentation (tether dynamics)
TiPS (NRL) [35]	1996	Scientific experimentation (tether dynamics and long-term survivability)
MAST (Tethers Unlimited + Stanford Uni.) [21]	2007	Scientific experimentation (tether long-term survivability)
T-Rex (JAXA) [49]	2010	Technology demonstrator (OML theory)
STARS missions (Shizuoka Uni.) [40] [47]	2009 - 2014	Technology demonstrator (tether extension and dynamic motion analysis)
PROPEL (NASA) [6]	-	Technology demonstrator (ED tether)
ISS Reboost [22]	-	ISS stationkeeping concept study
Jovian Capture [39]	-	Concept for capture into Jovian System

In the past, particular focus has naturally been directed towards the use of an EDT in a planetary magnetic field such as around Earth [22] or Jupiter [38]; little attention however has been paid to the application of an EDT to deep space travel. Currently and in past decades, more attention has been paid to attempting the direct study of the Solar system and interstellar space, but progress has been slow due to the limitations of propulsion and power generation; conventional chemical propulsion suffers from the "tyranny of the rocket equation", meaning that performance is mass-limited. Similarly, alternative propulsion means such as Solar sails [28] or high specific impulse electric propulsion methods such as ion drives suffer from the lack of Solar radiation intensity in deep space to run their equipment; other alternative propulsion methods such as high-efficiency nuclear propulsion suffer from being unproven in space, while EDTs have a high Technology Readiness Level (TRL) of around 8, having been demonstrated in space missions.

Figure 1.1: Artist's impression of a theoretical space tether system anchored to the Space Shuttle, in the same way as the TSS missions [32].

It is in this scenario in which an EDT could prove useful, as it is able to run without the use of propellant, since thrust generation is only dependant on a current and the ambient magnetic field. It is also conceivable for an EDT to run without a net power consumption, and so could facilitate a means of propulsion in deep space.

1.1. Problem Statement

An EDT could prove to be a capable means of propulsion in deep space, and so this project has the aim of assessing the feasibility of the concept, and to ascertain if it should be further explored. Since the amount of study into EDT usages in deep space is relatively small, the approach is quite broad, but in order to effectively focus the study, the following research question is to be answered:

What is the feasibility of electrodynamic space tethers as a means of propulsion applied to possible future interplanetary and/or interstellar missions? Also what is the viability of a transient-current solution for the electrodynamic tether?

This is made up of the following subquestions, which are used to fully answer the question:

- *What level of performance can realistically be achieved by an EDT in interplanetary and/or interstellar space?*

- *Which regions of space would an EDT spacecraft be suited to operating, and on what kinds of missions?*

- *What design concepts of an EDT are best suited to the above-mentioned operating regions?*

- *How competitive is the EDT as a means of propulsion when compared against both conventional chemical propulsion, and other alternative propulsion means?*

1.2. Scope of Study

Due to the early stages of research into the use of an EDT in deep space, the scope of this project is relatively limited. Most of the models implemented are quite elementary, and any optimisation procedures are also simple, without thorough analysis of the absolute optimal outcomes; this is done in order to reduce time spent on extensive feature implementation and analysis, which would not provide additional information in the context of a feasibility study, where the goal is mainly to assess the general potential performance of a more rigorous analysis that could be performed in the future.

1.3. Research Method

To answer the previously described research questions, a simulation environment has been established, using the Tudat simulation toolbox as its base; into which a number of additional custom environment models were implemented, namely to model the IMF strength and direction, as well as the current generated through the EDT, which interacts with the IMF to provide thrust. In addition to these environmental models, the EDT itself was parameterised to allow changes to for instance tether length to alter the operating properties and performance of the spacecraft overall; on top of this a simple guidance logic was also implemented, allowing the system to raise or lower its orbit, depending on the chosen mission profile.

Three different mission profiles were then defined, namely Simple-Straight-Out (SSO) which evolved during development into SSO+, Inner Solar System Out (InO), and SOKGA (Straight-Out with Kickstage and Gravity Assist). These were used to quantify EDT performance for interplanetary missions and beyond.
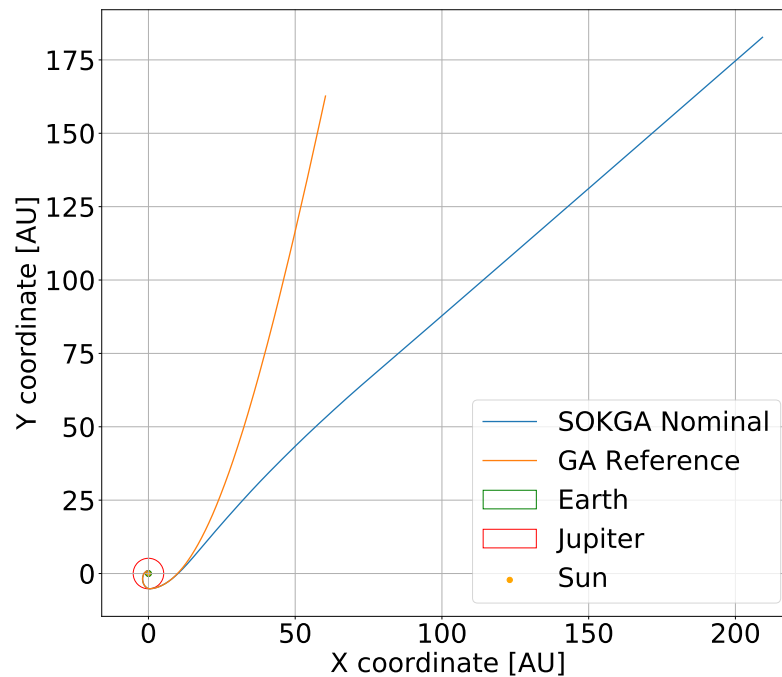
Figure 1.2: Example of what a SOKGA mission profile trajectory could look like, in this case using a Jupiter gravity assist, and comparing against a reference ballistic trajectory, both run with equal propagation time.

The performance analysis was then split into two stages: firstly the EDT configuration parameters were assessed, using a relatively short simulation period of 1 year, in a simple circular orbit at 1 AU, with any orbital perturbations removed; it should be noted that in this stage no optimisation took place, and only a simple grid-search analysis was done. This first stage established a baseline EDT spacecraft, with its physical properties such as length and materials established, which would then be taken forward for use in the second stage, the mission profile assessment.

The second stage analysis considered how each of the described mission profiles could be varied in order to give an idea for the best performance achievable given the baseline spacecraft, which employed the Differential Evolution (DE) optimisation scheme used by Pagmo and Pygmo for the SSO+ and InO mission profiles, using the maximum achieved change in aphelion over a simulation period of 100 years as the optimisation goal.

For the SOKGA case, the analysis was further split into two parts, the first using a Lambert solver (first stage analysis) as a basis to employ the Multi-Objective-Differential-Evolution (MOEAD) optimisation scheme used by Pagmo and Pygmo, to identify ballistic trajectories that could be used as potential candidates for further analysis with an EDT enabled. This optimisation scheme used launch DV and the final achieved Solar distance after a fixed time of flight (TOF) as overall optimisation parameters, the results from which formed a Pareto front of trajectories that were carried forward into the main analysis with the EDT thrust implemented.

This main (second) analysis stage then needed no (further) optimisation, as all trajectories found in the Pareto front from the first stage could be directly run and assessed; to determine performance in this analysis phase, the TOF to reach 100 AU (i.e., the edge of the Solar system), and the velocity at this point, were used.

After the results of the analysis were made, a sensitivity analysis was also conducted, to assess which parameters the solutions are heavily dependent on, as well as highlighting the areas to focus on, to achieve possible performance gains.

1.4. Relevance and Novelty

The aim of this research is to ascertain the feasibility of using an EDT in deep space; this effort could provide the basis for a new avenue of research, opening up the possibility of more capable deep-space research spacecraft. This can be achieved by potentially highlighting a novel propulsion method, which is limited neither by reliance on Solar energy, nor the use of physical propellants like many conventional propulsion systems; similarly the limitations of an EDT to deep-space applications can be highlighted, so that future work can be focused on applications that may yield good results.

The novelty of this research is quite clear, as little to no literature currently exists on the use of EDTs for propulsion in deep space.

1.5. Thesis Outline

Firstly, Chapter 2 covers the models used in the developed simulation environment, which provides the basis for all further analysis; subsequently, Chapter 3 covers how each element of the simulations is set up, covering optimisation procedures and specific simulation settings. Following this Chapter 4 covers the verification and validation efforts to ensure the implemented models and simulations are running as intended and reflect reality. Chapter 5 covers some preliminary results from simulations such as the EDT configuration analysis, which support the final results but do not directly contribute to answering the research question; following this of course is Chapter 6, which covers the results for each mission profile, which directly provides data to answer the research questions. Chapter 7 covers the results of the sensitivity analyses, and Chapter 8 is a general discussion of various subjects, with the knowledge gained throughout the rest of the report. Finally, Chapter 9 presents the final conclusions of the study, as well as recommendations for future research.

2

Simulation Modelling

In order to properly create the simulation environment, various models were used for each portion of the simulation; this chapter describes the implementation of each of these components in more detail. Either the settings for certain existing models are described here, such as which third-body perturbations are included, or entirely new models required for this research are introduced.

2.1. Orbit Simulation Modelling

The simulation of spacecraft trajectories was implemented using Tudat in C++ [14], which has extensive modelling features for various orbit simulations. All simulation propagations are conducted in the ECLIPJ2000 reference frame, with the Sun at its centre, using Cartesian coordinates. The reasoning for the reference frame and centre point are quite clear as this study focuses on interplanetary travel; Cartesian coordinates are used since they are conceptually simple, and do not adversely effect the simulation quality, speed, or achieved results. A simple diagram of the simulation reference frame is shown in Figure 2.1 [52].
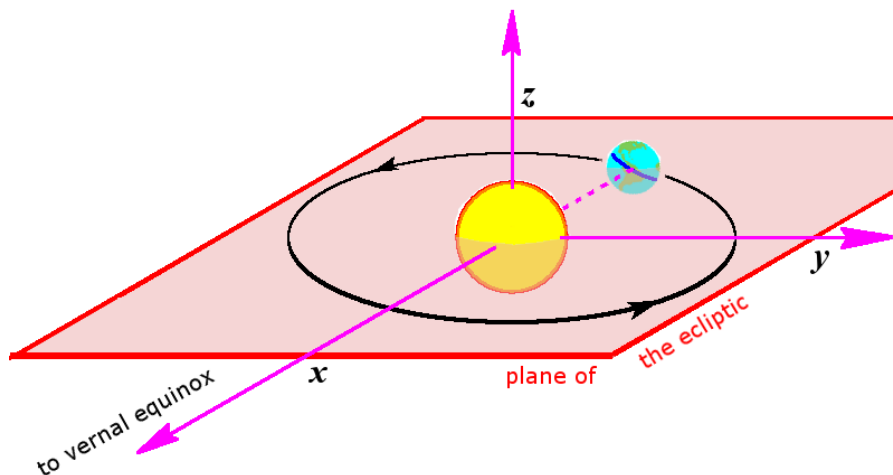

Figure 2.1: Diagram of the heliocentric simulation reference frame with Cartesian coordinates [52].

For models that are newly implemented into the simulation environment however, it is often easier to use a different reference frame or coordinate system, which is then converted to the simulation system; when this is the case it will be described where appropriate.

2.2. Integrator and Propagator Choice

Various integrators are readily implemented into Tudat, and so it makes sense to use one of these for project simulations; the question then becomes which one to use. It was quickly decided to make use of a variable order and step-size integrator over a simpler fixed step-size one such as RK4, since variable integrators offer the advantages of improved fidelity and runtime for applications such as orbit simulation where the step-size needs to change drastically, which is expected to be the case here due to the expected high eccentricity orbits. Therefore it was decided to use the RK87DP integrator [45], since it is part of the RK4 family of integrators, which are simple but effective. Ultimately the specific integrator choice is not key to obtaining good results in this research, since the simulation time is relatively short, and so an easy to use solution is favourable over the most efficient one. It should also be noted that integrator tuning was only roughly done, with absolute and relative tolerance values of 10^{-5}, which are verified in Chapter 4.

The Cowell propagator was chosen as the method to utilise in the simulation environment; it is already implemented in Tudat [45], and can be used with any kind of propagation, making it easy to use. Additionally, the number and fidelity of simulations required to be run for this study is not expected to be high, therefore the potentially lower performance of the Cowell propagator compared to others such as a unified state model is a much less important consideration than the ease of use. Similarly to the integrator choice, the propagator is not essential to the study outcome, for the same reason.
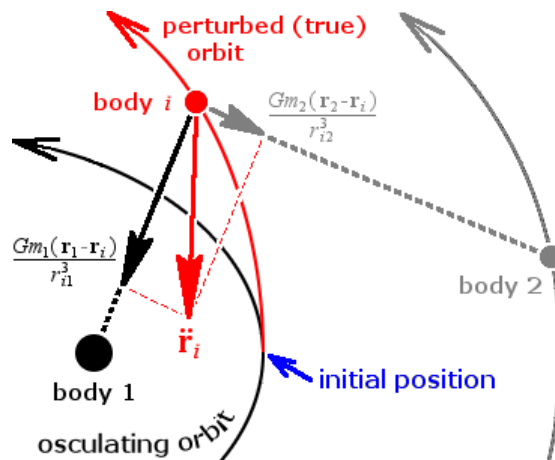
Figure 2.2: Cowell's method of orbit propagation, using numerical integration of all perturbing forces acting on the body. In this example the forces resulting from body 1 and body 2 are summed up so that the acceleration modelled on body i is $\ddot{r}_i$ [50].

For a full description of the available integrators and propagators in Tudat and the considerations that went into these decisions, one can refer back to the literature study associated with this thesis [46].

2.3. Magnetic Field Modelling

Since it is theoretically possible for the EDT to operate both in the interplanetary magnetic field (IMF) and the interstellar magnetic field (ISMF) in the scope of this project, the magnetic field modelling is split into these two distinct efforts. It should be noted that originally a model for the transitional magnetic field was also considered, but since the spacecraft would be crossing this boundary relatively quickly, it was decided not to go forward with this effort.

2.3.1. Interplanetary Magnetic Field Model

For the IMF region it was decided to use a simple Parker spiral magnetic field model [34], modulated to account for the Solar cycle; this model is two-dimensional (i.e., no z-component of the magnetic field). This decision can be justified by the fact that the mission profiles assessed in this study take place at very low inclinations, where the z-component of magnetic field is negligible [41]; the Parker magnetic field model is generally the basis for IMF models, with more complex ones adding extra terms to account for other factors such as the dependence on latitude [26]. For a more full description of the Parker model itself and other ancillary information, one can refer to the predecessor literature study of this report [46].

In this model, the magnetic field is characterised by its radial and azimuthal components B_R and B_ϕ respectively, with ϕ referring to the azimuthal angle of the local heliospheric magnetic field. A diagram of the Parker spiral with these IMF parameters can be seen in Figure 2.3, which is a modified image from Wolfram Alpha [3]
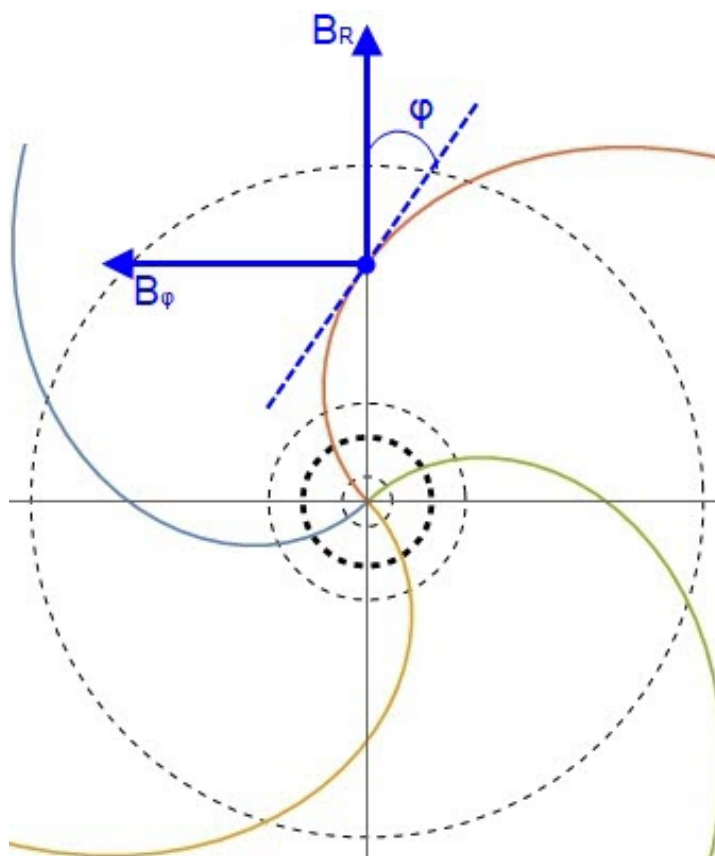

Figure 2.3: Parker spiral model of the IMF, with radial and azimuthal components indicated. The diagram is a modified version of [3].

Assuming that the magnitude B_0 and direction ϕ_0 of the magnetic field at a particular distance R_0 are known, then the radial magnetic field $B_{R,0}$ and azimuthal component $B_{\phi,0}$ can be found using Equations 2.1 and 2.2 respectively [33], in which B_0 and ϕ_0 refer to the magnetic field strength and azimuthal angle of the HMF to the radial direction respectively, at distance R_0.

$$B_{R,0} = B_0 \cos(\phi_0) \tag{2.1}$$

$$B_{\phi,0} = B_0 \sin(\phi_0) \tag{2.2}$$

Equations 2.3 and 2.4 can then be used to find the radial and azimuthal magnetic field components respectively, at an arbitrary distance R [33].

$$B_R = B_{R,0} \left(\frac{R_0}{R} \right)^2 \tag{2.3}$$

$$B_\phi = B_{\phi,0} \left(\frac{R_0}{R} \right) \tag{2.4}$$

Combining the above equations into a single vector equation, and using the assumption that the z-component of the magnetic field strength is zero, allows the use of Equation 2.5 to find the full magnetic field vector **B** at arbitrary distance R. This equation clearly shows that the radial component decays with R^2, while the transverse component decays with R; this implies that at greater Solar distances, the magnetic field become predominantly in the transverse direction, creating a mostly radial force generated by the EDT. It is this magnetic field decay with R that inspired some hope that an EDT could be a viable alternative to the use of Solar radiation as a propulsion source in deep space (either directly or via power generation), which decays uniformly with R^2.

$$\mathbf{B} = \begin{pmatrix} B_R \\ B_\phi \\ B_z \end{pmatrix} = \begin{pmatrix} B_0 \cos(\phi_0) \left(\frac{R0}{R} \right)^2 \\ B_0 \sin(\phi_0) \left(\frac{R0}{R} \right) \\ 0 \end{pmatrix} \tag{2.5}$$

In order to approximately account for how the magnetic field conditions change over time, data collected by spacecraft at around 1 AU can be used, and extrapolated into the future; the magnetic field strength B_0 at $R_0 = 1$ AU can be directly found from OMNI2 spacecraft data provided by NASA [23]. This data can be used to apply a least-squares approximation (using Python) which extrapolates the trend into the future.

Since the magnetic field activity of the Sun is linked to the general Solar activity [33], the base function used to fit the data to is composed of two sinusoidal signals. The first of these signals represents the well-known 11-year Solar cycle [29], while the second signal represents the less well-known Wolf-Gleissberg Solar cycle with a period of 60 to 150 years [29]. It should be noted that a fitting function like this does not already directly exist in literature, but its simplicity makes its implementation quite straightforward.

In the fitting process, Equation 2.6, a custom model, is used, in which a_1, a_2, b_1. b_2, c_1, c_2 and d are adjustable parameters of the sinusoidal function for fitting, whereas B_0 and t represent the magnetic field strength at 1 AU and time respectively. The lower and upper bound for the regular Solar cycle are 10 and 12 years respectively, while the lower and upper bounds for the Wolf-Gleissberg cycle are 60 and 150 years respectively; these bounds affect parameters b_1 and b_2, while the other parameters remain unbound.

$$B_0 = a_1 \sin(b_1 t + c_1) + a_2 \sin(b_2 t + c_2) + d \qquad (2.6)$$

The approximation uses a non-linear least-squares method to fit the data to the provided function. The specific least-squares method used is the "optimize.curve_fit" function found in the scipy Python package [1]; since the extrapolation of magnetic field data into the future is already quite uncertain using this method, it was deemed default values would be sufficient for any optional parameters, with the exception of using relevant bounds where required.

Applying the least-squares approximation, with B_0 and t in units of nT and calendar years respectively, the adjustable parameters are found to be as shown in Table 2.1. For easier understanding, instead of b_1 and b_2, the parameters T_1 and T_2 are introduced, referring to the periods of each sinusoidal signal, which can be related to b_1 and b_2 using Equation 2.7.

$$b_x = \frac{2\pi}{T_x} \qquad (2.7)$$

Table 2.1: Values determined for fitting parameters of B_0 in Equation 2.6, using a least-squares method.

Parameter	Value	Unit	Bounds
a_1	1.00	nT	unbounded
a_2	1.50	nT	unbounded
b_1	0.10	-	(0.1, 0.4)
b_2	0.57	-	(0.5, 0.6)
T_1	62.8	years	(60, 150)
T_2	11.0	years	(10, 12)
c_1	4	-	unbounded
c_2	-2.9	-	unbounded
d	6.2	nT	unbounded

The produced sinusoidal fit curve can then be overlayed on the satellite data, and extrapolated to the year 2060, as shown in Figure 2.4; it was chosen to extrapolate to 2060 fairly arbitrarily, just to get a good sense of what the future trend could look like.
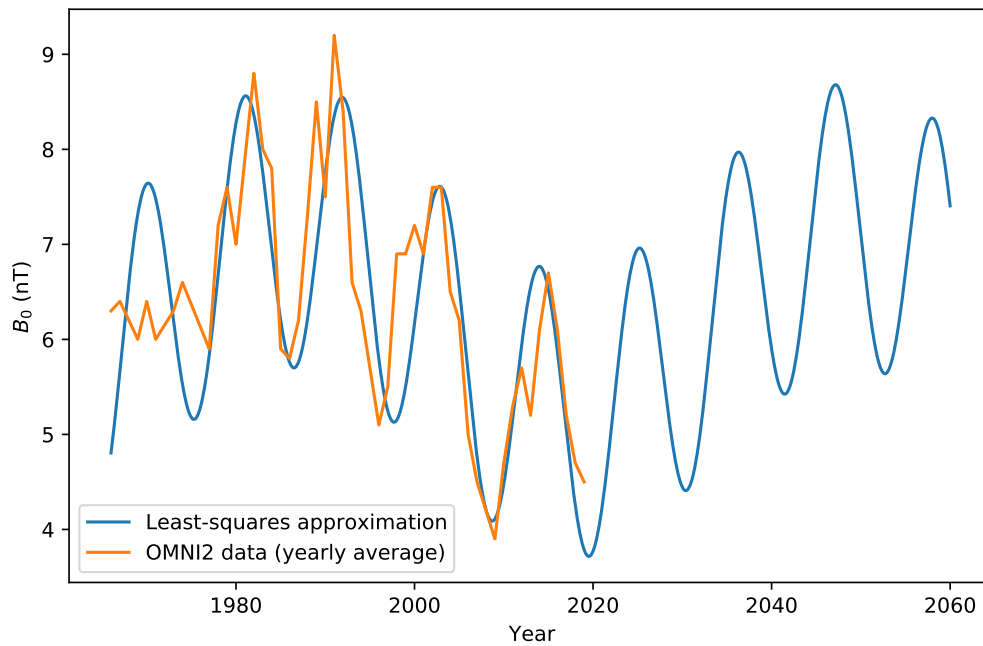
Figure 2.4: Least-squares approximation and extrapolation of magnetic field strength data at 1 AU, using OMNI2 data [23].

Figure 2.4 shows that the fit function approximates the trend in the satellite data reasonably well, with the exception of the early regions of data from around 1970 - 1980, which is known to be an anomalous time. As can be seen from historically reconstructed data in Figure 2.5 [33], the fit function described in Figure 2.4 does indeed trend well with both modern and historic data well enough for the purposes of simulations in this project. It should be noted that the spacecraft observations in Figure 2.5 come from the OMNI2 data set, encompassing measurements from a number of spacecraft in various high-Earth and interplanetary orbits, primarily spacecraft in Geocentric or L1 Earth-Sun Lagrange point orbits; more information can be found in the OMNI2 documentation [23]

Figure 2.5: Historic magnetic field strength data. The red line refers to spacecraft observations, whereas the yellow and white lines refer to reconstructions from geomagnetic activity data; sunspot data is also included shown by the black lines, scaled to the same axes [33].
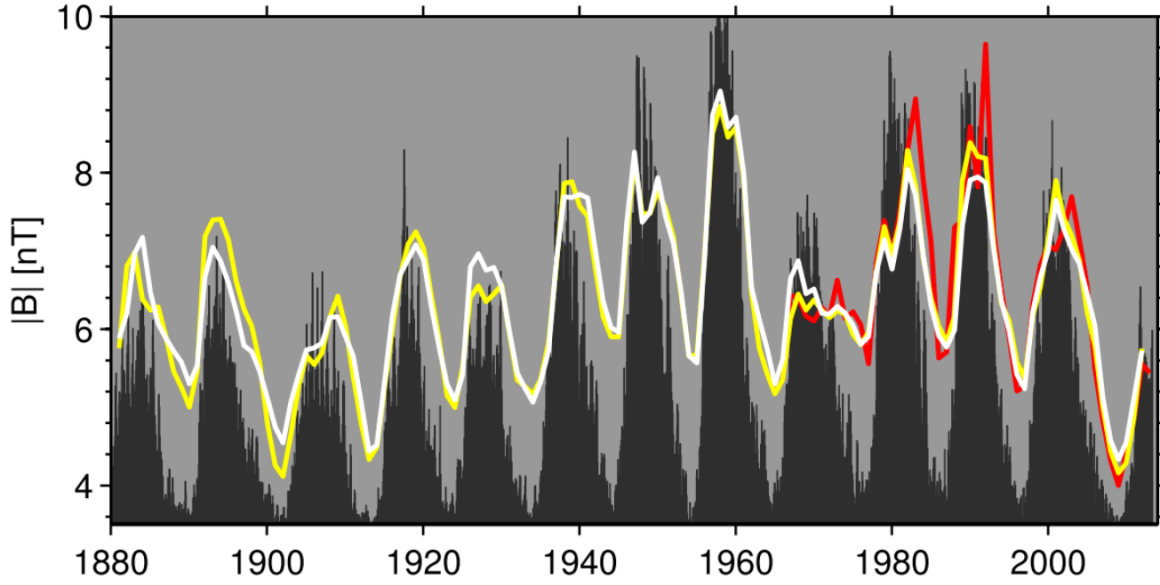
Unlike B_0, the azimuthal angle ϕ_0 must be derived from other values, in this case from the Solar wind speed V_{sw}, also taken from OMNI2 data [23]. With the assumption that the z-component of the magnetic field is zero, then according to the Parker model the (non-normalised) direction vector of the magnetic field $\mathbf{B}^*$ is approximately given by Equation 2.8 [9], in which V_{sw} must be given in km/s.

$$\mathbf{B}^* = \begin{pmatrix} B_R^* \\ B_\phi^* \\ B_z^* \end{pmatrix} = \begin{pmatrix} 1 \\ -405/V_{sw} \\ 0 \end{pmatrix} \tag{2.8}$$

Using the values in Equation 2.8, ϕ_0 can then be calculated by using Equation 2.9 [9].

$$\phi_0 = \arctan\left(-\frac{\hat{\mathbf{B}}_\phi}{\hat{\mathbf{B}}_R}\right) = \arctan\left(\frac{405}{V_{sw}}\right) \tag{2.9}$$

Performing the above calculations using V_{sw}, the azimuthal angle can be found, fitted and plotted in much the same way as was done for B_0, since V_{sw} is provided in the OMNI2 data [23]. Using V_{sw} to calculate ϕ_0 over time, it can then be modelled as a sinusoid with two signals, as shown in Equation 2.10, which is analogous to Equation 2.6.

$$\phi_0 = a_1 \sin(b_1 t + c_1) + a_2 \sin(b_2 t + c_2) + d \tag{2.10}$$

The OMNI2 data can then be fitted to Equation 2.10 using the same least-squares approximation method as for B_0, specifically from the Scipy Python package [1], using relevant bounds where required. The results from the fitting are shown in Figure 2.6, along with the estimation

parameters used to arrive at the fit function in Table 2.2. Also shown in the plot are the global average, and a sinusoidal fit function similar to the one used to extrapolate B_0, but this time only with a single sinusoidal component. This is done because the ϕ_0 data appears only to track with the 11-year Solar cycle, rather than also with the Wolf-Gleissberg cycle.
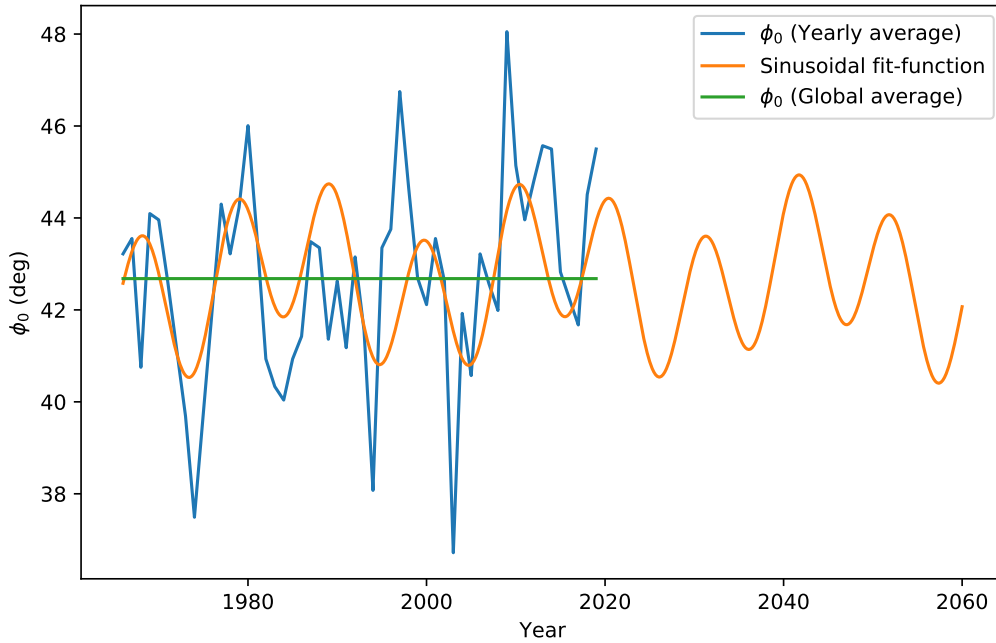

Figure 2.6: Least-squares approximation and extrapolation of magnetic field direction data at 1 AU (in orange), using yearly average ϕ_0 (in blue) derived from OMNI2 data [23]. Also shown is the global average of ϕ_0 in green.

Table 2.2: Values determined for fitting parameters of ϕ_0, using a least-squares method.

Parameter	Value	Unit	Bounds
a_1	0.738	deg	unbounded
b_1	0.216	years	(0.1, 0.4)
c_1	76.3	-	unbounded
d_1	42.7	deg	unbounded

It can be seen quite clearly from Figure 2.6 that the sinusoid generated by the least-squares solution does not appear to match well with the OMNI2 data, indicating that there is something that this simple model is unable to fully appreciate, in particular the sharp spikes present in the data (which are not replicated by the model) should be noted. It can be seen however that the oscillations in ϕ_0 do not appear to have a positive or negative overall trend, therefore instead of more fully investigating a better model, the simple global average of ϕ_0 is used instead; this can be justified as the angle mismatch is only 4° at most. The sensitivity study of Chapter 7 will show that the overall results are not particularly sensitive to the value of ϕ_0 over the range of a few degrees shown here, and so the global average is a good-enough approximation. This global average value that will be used is $\phi_0 = 42.7°$.

2.3.2. Interstellar Magnetic Field Modelling

The modelling of the interstellar magnetic field is relatively straightforward; in the vicinity of the Sun and beyond, the ISMF is effectively homogeneous over the time and space scales considered for this study [36], meaning a simple single magnetic field vector can be used in the modelling. In many academic publications, values are given in the J2000 heliocentric ecliptic reference frame, in spherical coordinates; therefore these will be used before being converted to Cartesian coordinates for simulation. A diagram of such a coordinate system is shown in Figure 2.7 [?], showing the heliocentric ecliptic latitude and longitude β and λ.
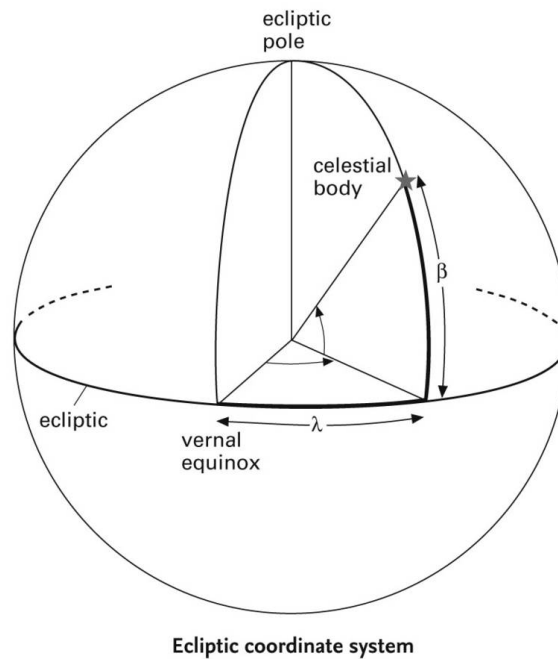
Figure 2.7: Heliocentric Ecliptic coordinate system diagram [?]

Values to characterise the ISMF are shown in Table 2.3 [55]; the values are taken at a distance of around 1000 AU, and are assumed to be constant for the purposes of simulations in this project.

Table 2.3: Characteristic values for ISMF [55].

Description	Symbol	Value	Unit
ISMF magnitude	$|\mathbf{B}_\infty|$	0.293 ± 0.08	nT
ISMF longitude direction	λ_∞	227.28 ± 0.69	deg
ISMF latitude direction	β_∞	34.62 ± 0.45	deg

The base values in Table 2.3 can be converted to Cartesian coordinates of the same reference frame using Equation 2.11.

$$\mathbf{B}_\infty = |\mathbf{B}_\infty| \begin{pmatrix} B_x \\ B_z \\ B_y \end{pmatrix} = \begin{pmatrix} \cos\left(\beta_\infty\right)\cos\left(\lambda_\infty\right) \\ \cos\left(\beta_\infty\right)\sin\left(\lambda_\infty\right) \\ \sin\left(\beta_\infty\right) \end{pmatrix} \tag{2.11}$$

It should be noted that already it can be seen the ISMF magnitude is weaker than the IMF at 1 AU, being around 0.3 nT compared to around 7nT; however at larger Solar distances the ISMF actually tends to become stronger than the IMF, as shown in Subsection 4.1.3.

2.4. Current Modelling

Depending on the situation and EDT configuration, the current magnitude carried through the EDT can change; however its orientation is determined by the orientation of the spacecraft, which is addressed in Section 2.8.

2.4.1. Bare-Tether Current Model

The current behaviour for a bare-tether configuration has highly non-linear governing equations, and is dependent on the external ionosphere. The procedure and equations used in this model are primarily taken from Zhu [54], unless otherwise stated, which presents a good model for an EDT in LEO, with some additional assumptions and simplifications which can also be used for an interplanetary model. Figure 2.8 shows a diagram of electron and ion collection along the bare tether, and also that electrons are actively emitted at the cathodic end C. Also shown are graphs of how the voltage and current vary; V_p, V_t, and I refer to the motion-induced voltage, EDT voltage due to ohmic loss, and the current respectively.

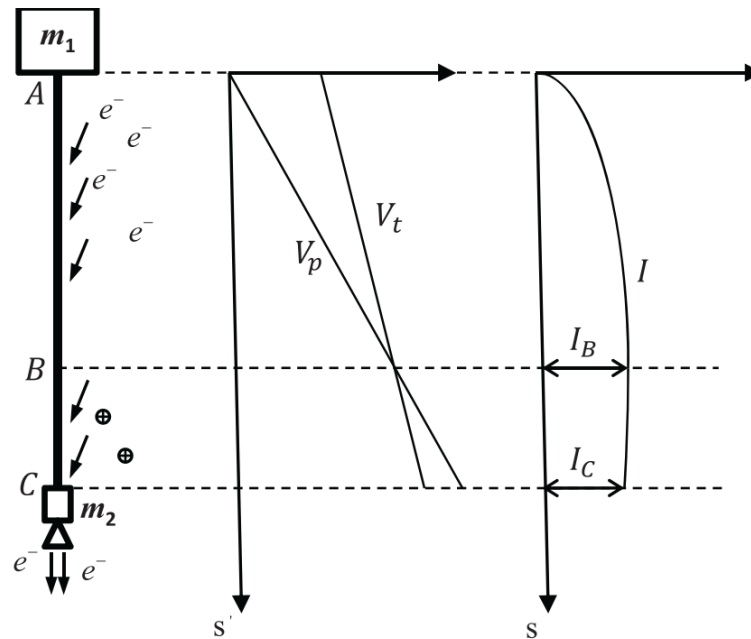Figure 2.8: An EDT which uses a bare-tether configuration, with the voltage and current variation across the tether. A and C denote the anodic and cathodic ends respectively, and B is the point where the potential bias ΔV is equal to zero [54].

Firstly a number of dimensionless variables are defined, for later convenience, as shown in Equations 2.12, 2.13 and 2.14 [54], in which s refers to the distance along the EDT.

$$\epsilon = s/L_0 \tag{2.12}$$

$$i = \frac{I(s)}{I_0} \tag{2.13}$$

$$\lambda = \frac{\Delta V}{V_0} \tag{2.14}$$

In the above equations L_0, I_0 and V_0 are the unit values for length, current, and voltage, defined respectively in Equations 2.15, 2.16 and 2.17. m_E, σ, E_m, A, e, and n_∞ refer respectively to the electron mass, tether conductivity, motional electromotive potential difference across the EDT, tether (conducting) cross-sectional area, electron charge, and unperturbed plasma density.

$$L_0 = \left(\frac{9\pi m_E \sigma^2 E_m A}{128 e^2 n_\infty^2} \right)^{1/3} \tag{2.15}$$

$$I_0 = \sigma E_m A \tag{2.16}$$

$$V_0 = E_m L_0 \tag{2.17}$$

It should be noted that in order to calculate E_m in the above equations, Equation 2.18 can be used, in which $\mathbf{V_{rel}}$, $\mathbf{B}$, L, and $\mathbf{1}$ refer to the spacecraft velocity relative to the magnetic field strength, the magnetic field strength vector, the tether length, and the unit vector along the tether length respectively.

$$E_m = L \cdot \mathbf{1} \cdot (\mathbf{V_{rel}} \times \mathbf{B}) \tag{2.18}$$

The tether conductivity σ is a fundamental material property, however for a composite tether with a core and shell, which can be trivially modelled as two conductors in parallel, it can be calculated as an average value using Equation 2.19 in combination with Equation 2.20, in which the subscript "tot" refers to the total composite value of that parameter; R refers to the tether resistance.

$$\sigma_{tot} = \frac{R_{tot} A_{tot}}{L} \tag{2.19}$$

$$R_{tot} = \left(\frac{1}{R_1} + \frac{1}{R_2} \right)^{-1} \tag{2.20}$$

In order to speed up simulation time, Zhu [54] introduces a procedure in which the voltage-current relationship, which would normally have to be integrated at every timestep, can be simplified to an analytical solution, under the assumption that the overall dimensionless current is very small, i.e. $i \ll 1$. This assumption essentially corresponds to the situation where the electromotive force is weak (such as in interplanetary and interstellar regions), or where the

tether is short. This allows the average dimensionless current across the tether i_{avg} to be derived, as shown in Equation 2.21; L refers to the tether length, and λ_A to the dimensionless voltage at point A (refer to Figure 2.8).

$$i_{avg} = -\frac{1}{5L}\lambda_A^{5/2} + \frac{1}{2}\lambda_A^{3/2} \tag{2.21}$$

The dimensionless voltage at A can be calculated using Equation 2.22, in which i_C refers to the dimensionless current at point C (refer to Figure 2.8). It should be noted that the current at point C I_C is assumed to be known, as it is a design parameter driven by the electron discharge rate at the EDT cathode end, and can be converted to a dimensionless current using Equation 2.13.

$$\lambda_A = \left(2i_C - i_C^2\right)^{2/3} \tag{2.22}$$

The dimensionless average current i_{avg} can then be converted to the true average current I_{avg} using Equation 2.13, which can then be used in thrust equations of Section 2.8. It should be noted that according to Equation 2.22, λ_A is always positive, and so i_c must always be positive.

2.4.2. Transient-Current Model
It was discussed in the literature study [46], as well as being expanded on in Chapter 8 that there is a potential transient-current-type solution that could be implemented to an EDT tether. This model encompasses methods that apply current transiently in one direction along the tether, which would then have to be regularly reversed to attain constant thrust. This could be done by using alternating current, with frequency in-time with the spacecraft's physical rotation, or single-line power transmission methods to provide a current as power is transmitting between storage devices at each end of the tether.

After more thorough research into the topic it has been discovered that any solution like this would either work only on a short time frame (for example a few minutes or hours at most), or would rely on some form of single-line power transmission, which has not yet been shown to be viable (for use in space).

Despite this, it was decided to include a transient-current-type model, to fully explore the possibility that a form of single-line power transmission in space would be able to facilitate the use of an EDT. Since a spacecraft operating in this manner is currently beyond the reach of current research and development, only a very simple implementation has been considered: the current is provided at a constant value along the length of the EDT, which is then carried directly through to the simulation environment in the same way as I_{avg} in the bare-tether case.

2.5. EDT Configuration
This section covers the variables used to parameterise the EDT configuration, which are then varied to assess its performance. It has been decided that a Hoytether configuration [16] will be employed over a tape tether or other type of EDT, especially since a special case of the Hoytether is a single-line tether. The justification for this is essentially that a Hoytether provides advantages for survivability, without significantly hampering performance [16]; a more thorough explanation of this can be found in the literature study [46]. It should also be noted that the section is further split into two main sections covering the Hoytether parameters, followed by the mass model for the vehicle.

2.5.1. Hoytether Configuration Parameters

A Hoytether is essentially made up of a number of primary lines connected by supporting secondary lines, as shown in Figure 2.9 [16], in which L, l_p, a and l_s refer to tether length, primary segment length, primary line separation and secondary segment length respectively.
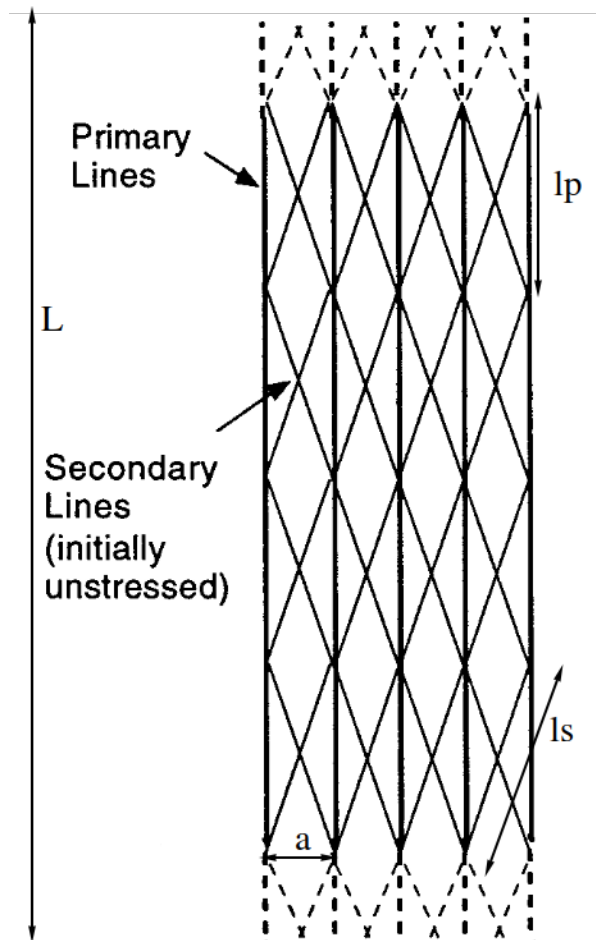

Figure 2.9: Section of a Hoytether design, with some parameters illustrated. Edited from diagrams in Forward 1995 [16].

A number of parameters can be calculated to help in characterising the Hoytether, as shown in the following equations [16]. These equations function both for tubular Hoytethers, and for tape-like Hoytethers; in this report only tubular Hoytethers are used. By defining a few characteristic variables, many of these useful derived parameters can be found; the characteristic variables are the tether length L, length of a primary line segment l_p, primary line separation distance a, and the total number of primary lines n.

A Hoytether can be split into multiple tether segments, each as long as one segment of primary line; the number of segments h can be found using Equation 2.23. respectively.

$$h = L/l_p \qquad (2.23)$$

The length of an individual secondary line l_s can be found using Equation 2.24, in which k_s refers to the slack coefficient (typically around 1.005 [16]), and a refers to the primary line

separation distance. It should be noted that the slack coefficient is the factor increasing secondary tether segment length, to account for some slack in the system.

$$l_s = k_s \sqrt{a^2 + l_p^2} \tag{2.24}$$

Equations 2.25 and 2.26 allow the calculation of the total number of primary links n_l and total number of secondary links m respectively.

$$n_l = nh \tag{2.25}$$

$$m = 2n_l = 2nh \tag{2.26}$$

Also the total length of primary lines L_p and total length of secondary lines L_s can be calculated with Equations 2.27 and 2.28.

$$L_p = Ln \tag{2.27}$$

$$L_s = ml_s \tag{2.28}$$

It should also be noted that in general each tether line is modelled as a composite material, with an inner core, surrounded by a shell material. This is done to allow the core to be made of a more conducting copper material, while the shell is made of a stronger lighter material, namely aluminium.
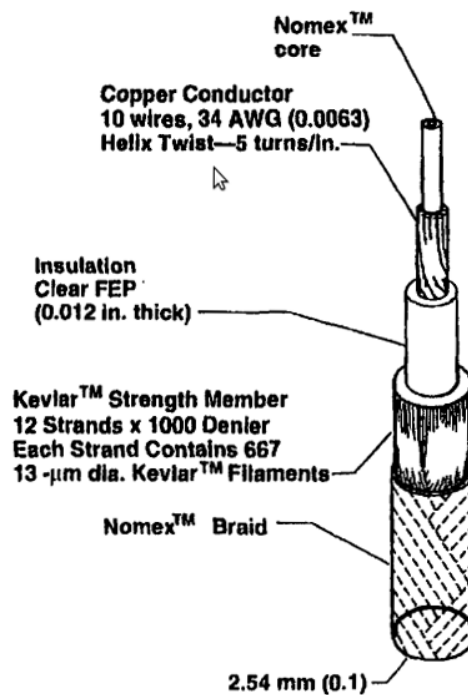

Figure 2.10: Example of a composite tether [31].

2.5.2. Vehicle Mass Modelling

Using the previously defined Hoytether parameters, calculating the vehicle mass m_{tot} is quite straightforward. The total mass is made up of the tether mass and endmasses, this is shown in Equation 2.29 in which m_t and m_e refer to the tether mass and individual end mass respectively; it should be noted that it is assumed the endmasses are equal.

$$m_{tot} = m_t + 2m_e \tag{2.29}$$

The end mass m_e is directly defined, however some further calculations must be made to determine the tether mass. First the mass is split up into the primary and secondary Hoytether lines, as shown in Equation 2.30, in which m_p and m_s refer to the total mass of primary and secondary tether lines respectively.

$$m_t = m_p + m_s \tag{2.30}$$

The total primary and tether line masses are calculated in much the same way, therefore only the primary line equations are included in the following descriptions. Firstly the total primary mass can be calculated using Equation 2.31, in which V_p and ρ_p refer to the total primary line material volume, and primary line composite density respectively.

$$m_p = V_p \rho_p \tag{2.31}$$

V_p can be calculated using Equation 2.32, in which A_p and L_p refer to the individual primary line tether cross sectional area, and the total length of primary line respectively; L_p is a known value calculated using Equation 2.27.

$$V_p = A_p L_p \tag{2.32}$$

A_p can then be calculated using Equation 2.33, in which $A_{p,inner}$ and $A_{p,outer}$ refer to the inner and outer cross sectional areas respectively; these areas are be directly defined for each simulation.

$$A_p = A_{p,inner} + A_{p,outer} \tag{2.33}$$

To complete the set of equations, ρ_p can be found with Equation 2.34, which is a simple weighted average of the primary line inner and outer area densities $\rho_{p,inner}$ and $\rho_{p,outer}$.

$$\rho_p = \frac{\rho_{p.inner} A_{p,inner} + \rho_{p,outer} A_{p,outer}}{A_{p,inner} + A_{p,outer}} \tag{2.34}$$

As stated previously, this series of operations can be completed in exactly the same way for the secondary line mass, but replacing relevant primary line parameters with their secondary line counterparts (for example L_p should be replaced by L_s).

2.6. Gravitational Modelling

There are two sources of gravitational force modelled in the simulation environment: central body point-mass, as well as 3rd body point-mass. It was chosen to ignore any spherical harmonic gravitational effects, as the central body is the Sun and these effects can safely be neglected. There are some mission profiles that utilise gravity assists, and so the modelling for those is also described here.

2.6.1. Nominal Point-Mass Modelling

The gravitational force F_g between two point-mass bodies is given by Equation 2.35 [13], in which G, m_1, m_2, and r refer to the universal gravitational constant, mass of body one, mass of body 2, and the distance between them respectively.

$$F_g = G \frac{m_1 m_2}{r^2} \tag{2.35}$$

For a spacecraft, whose mass can be neglected compared to planetary-mass bodies, this can be simplified down to the spacecraft acceleration g, as shown in Equation 2.36, in which M refers to the mass of the massive object in question.

$$g = \frac{GM}{r^2} \tag{2.36}$$

This modelling is then implemented internally within Tudat [14], allowing all planetary bodies (as third bodies) in the Solar System, as well as the Sun (as the central body), to be modelled, and can be turned on or off easily in the simulation settings. All these bodies are simply modelled as point-mass objects, with default parameters defined by Tudat [14]; the full DE430 SPICE ephemerides are used [2], since longer simulation times are required than the Tudat defaults.

2.6.2. Gravity-Assist Modelling

Some mission profiles described in later sections utilise a gravity-assist to help the EDT space-craft more quickly achieve large Solar distances. These assists work by using a massive body such as Jupiter or Saturn to accelerate the spacecraft, imparting some of the planets momentum onto it, altering the velocity by changing its heliocentric direction of travel, rather than magnitude of velocity [48]. In the simulation environment itself (and more specifically within Tudat), this effect is not explicitly modelled, but rather is manifests itself from the numerical propagation of the equations of motion. Figure 2.11 shows the in-plane geometry of a gravity assist, centred on the assisting planet [48].
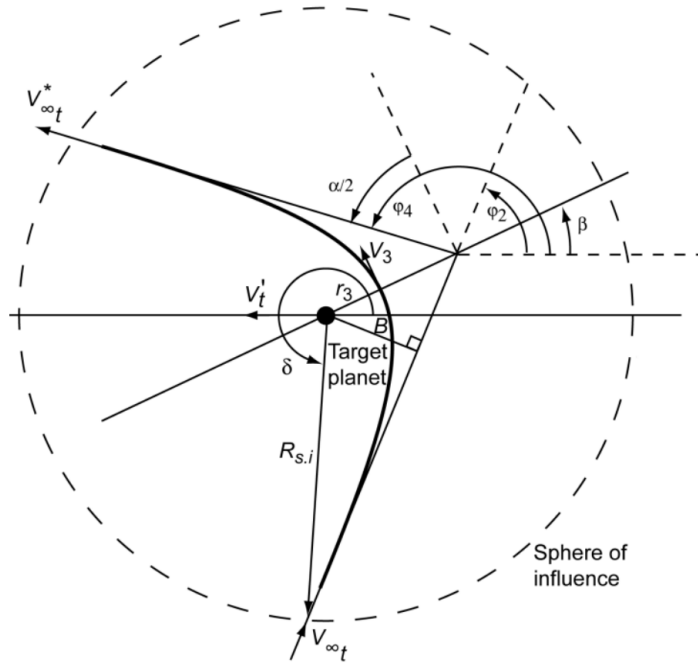
Figure 2.11: In-plane geometry of a hyperbolic encounter trajectory, with incoming and outgoing spacecraft velocity shown by $V_{\infty t}^*$ and $V_{\infty t}^*$, as well as the deflection angle α [48].

2.7. Solar Radiation Pressure

Solar Radiation Pressure (SRP) is implemented using the cannonball radiation pressure model already present in Tudat. To account for the unusual shape of an EDT spacecraft, the model is split into 3 major components: the two end masses, and the tether itself, which are together used to create the parameters required for a cannonball radiation pressure model.

2.7.1. SRP Effective Area Calculations

The total SRP area A_{SRP} of a general EDT spacecraft can be calculated as shown in Equation 2.37; in which $A_{end,1}$ and $A_{end,2}$ refer to the two endmass areas (assumed to be simple spheres), and $A_{eff,teth}$ refers to the effective tether area.

$$A_{SRP} = A_{end,1} + A_{end,2} + A_{eff,teth} \tag{2.37}$$

To account for the rotation of the spacecraft during operation, a simple rotation factor k_{rot} is introduced to calculate the effective area as shown in Equation 2.38, in which A_{teth} is the general tether area, and is calculated differently depending on the configuration. k_{rot} is a simple factor that gives the average fraction of the total tether area that is exposed to the Sun, in the perpendicular direction.

$$A_{eff,teth} = k_{rot} A_{teth} \tag{2.38}$$

Single Line SRP Area Calculation

The SRP area of a simple single-line EDT configuration $A_{teth,single}$ can be found using Equation 2.39, in which L and D_{out} refer to the total tether length, and the outer tether diameter respectively.

$$A_{teth,single} = LD_{out} \tag{2.39}$$

Hoytether SRP Area Calculation

In order to calculate the effective SRP area for a Hoytether configuration $A_{teth,hoy}$, one can use Equation 2.40, in which A_p and A_s are the total areas for the primary and secondary lines of the Hoytether respectively. The occultation coefficient k_{occ} is introduced to account for potential occultation of lines that could occur in a Hoytether configuration.

$$A_{teth,hoy} = k_{occ}(A_p + A_s) \tag{2.40}$$

The total SRP areas of the primary and secondary Hoytether lines can be calculated with Equations 2.41 and 2.42 respectively. The outer diameter of the primary and secondary lines D_p and D_s are known values, and the total length of primary and secondary lines L_p and L_s can be calculated using the equations shown in Section 2.5.

$$A_p = D_p L_p \tag{2.41}$$

$$A_s = D_s L_s \tag{2.42}$$

2.7.2. Radiation Pressure Coefficient Calculation

It is assumed that the two endmasses of the EDT spacecraft have the same radiation pressure coefficient, however the tether itself has a different one, that can vary depending on the material. Therefore the total average radiation pressure can be simply calculated as a weighted sum, accounting for the areas of each component, as shown in Equation 2.43; here k_{rad} refers to the total average radiation coefficient of the spacecraft, $k_{rad,end}$ and $k_{rad,teth}$ refer to the radiation coefficients of the endmasses and tether respectively.

$$k_{rad} = \frac{k_{rad,end}(A_{end,1} + A_{end,2}) + k_{rad,teth}A_{eff,teth}}{A_{end,1} + A_{end,2} + A_{eff,teth}} \tag{2.43}$$

2.8. Spacecraft Guidance

A number of simple guidance rules are followed to control the magnitude and direction of the EDT thrust; this section covers these guidance rules.

2.8.1. Thrust Magnitude

The magnitude of thrust is one of if not the most important parameter in the simulation environment, and so its calculation should be paid particular care. Using the previously implemented models for magnetic field strength and current, the thrust can be calculated quite easily.

The thrust vector $\mathbf{F}$ is calculated using the Lorentz force equation for a current-carrying wire as shown in Equation 2.45 (derived from Equation 2.44), where L, $\mathbf{I}$, and $\mathbf{B}$ refer to the tether length, current vector, and magnetic field vector respectively [27]. In the equation, L is defined a priori, $\mathbf{I}$ and $\mathbf{B}$ are calculated using the methods outlined in Sections 2.4 and 2.3 respectively.

$$\mathbf{F} = \int_0^L \mathbf{I}(l) \times \mathbf{B}(l) dl \tag{2.44}$$

$$\mathbf{F} = L\mathbf{I} \times \mathbf{B} \tag{2.45}$$

However, it is also necessary in order to stabilise an EDT spacecraft, that the cable should be kept taut [53]; in the absence of a significant gravity differential this is done by rotating the EDT spacecraft. This means that the spacecraft is not always oriented in the ideal direction for thrust generation and direction; in the simulation environment this is accounted for by introducing k_{Trot}, a simple coefficient representing the effective fraction of thrust generated accounting for the spacecraft rotation. This forms the final thrust generation equation, as shown in Equation 2.46

$$\mathbf{F} = k_{Trot}L\mathbf{I} \times \mathbf{B} \tag{2.46}$$

According to [53], values of k_{Trot} that can be achieved range from 0.5 - 0.75; for a more thorough description of these phenomena, one can refer to the literature study [46].

2.8.2. Thrust Direction
The thrust direction, as shown by Equation 2.45, is entirely determined by the current and magnetic field directions. In any situation the magnetic field of course cannot be changed, however the EDT orientation, and therefore current direction, can be altered. The direction of current flow in the EDT can also be altered, depending on configuration.

Since the EDT spacecraft is only planned to operate in the ecliptic plane, and the magnetic field itself has a negligible z-component, the spacecraft will always need to be oriented along the z-axis; since the provided thrust is always perpendicular to the magnetic field, this ensures no out-of-plane forces are generated. This leads to the case that there are only two viable values for the current direction direction $\hat{\mathbf{I}}$, either in the positive or negative z-directions, as shown in Equations 2.47 and 2.48 respectively.

$$\hat{\mathbf{I}}_p = \begin{bmatrix} 0 \\ 0 \\ 1 \end{bmatrix} \tag{2.47}$$

$$\hat{\mathbf{I}}_n = \begin{bmatrix} 0 \\ 0 \\ -1 \end{bmatrix} \tag{2.48}$$

Due to the fixed orientation of the magnetic field around an EDT spacecraft, the direction of thrust that can be applied is quite restricted; in-plane thrust can only be provided in either the "positive" or "negative" direction, along the vector at 90° to the local magnetic field. The magnitude of this thrust can be relatively easily altered by an orientation or current change. However for the purposes of this study either maximum or zero thrust is assumed.

Operation in the IMF

Due to the low-thrust nature of the EDT, sometimes several rotations around the Sun are required to make significant changes to the orbit, and cannot rely on being on a simple hyperbolic trajectory. Since the magnetic field direction changes with altitude, and therefore the thrust direction, it is not always possible to set the current direction as only $\hat{\mathbf{I}}_p$ or $\hat{\mathbf{I}}_n$ to achieve the desired orbital changes. In order to solve this, a simple guidance logic is implemented to the current direction vector, which relies on reversing the vector, generally depending what side of the orbit the spacecraft is on. This can either be done by rotating the entire spacecraft, or by reversing the current flow direction through the tether.

Three flight regimes are implemented. The first is the prograde configuration, aiming to increase the spacecraft distance from the Sun, and is the one which is most commonly used. The second one is the retrograde configuration, aiming to reduce the orbit perihelion, and is used in the initial stage of an InO trajectory. The final regime simply disables the EDT thrust completely, which can be used during the cruise of interplanetary transfers for example.

The logic itself simply compares the aphelion and perihelion of the previous timestep to that of the current timestep. In the prograde case, aphelion and perihelion increases are favoured. An aphelion increase with a perihelion decrease is allowed, and if the aphelion decreases then the thrust is disabled. In the retrograde case, perihelion decrease with an aphelion increase is favoured, aphelion and perihelion decreases are allowed, and if the perihelion increases then the thrust is disabled. This logic is summarised by the flow chart shown in Figure 2.12, in which some of the test blocks in each column are identical, this is intended to improve clarity.

All of these flight regimes rely on calculating the change in aphelion and perihelion, ΔAp and ΔPe respectively. This is done directly within the simulation environment, by simply comparing the aphelion and perihelion at a given timestep with its value at the previous timestep and taking the difference.
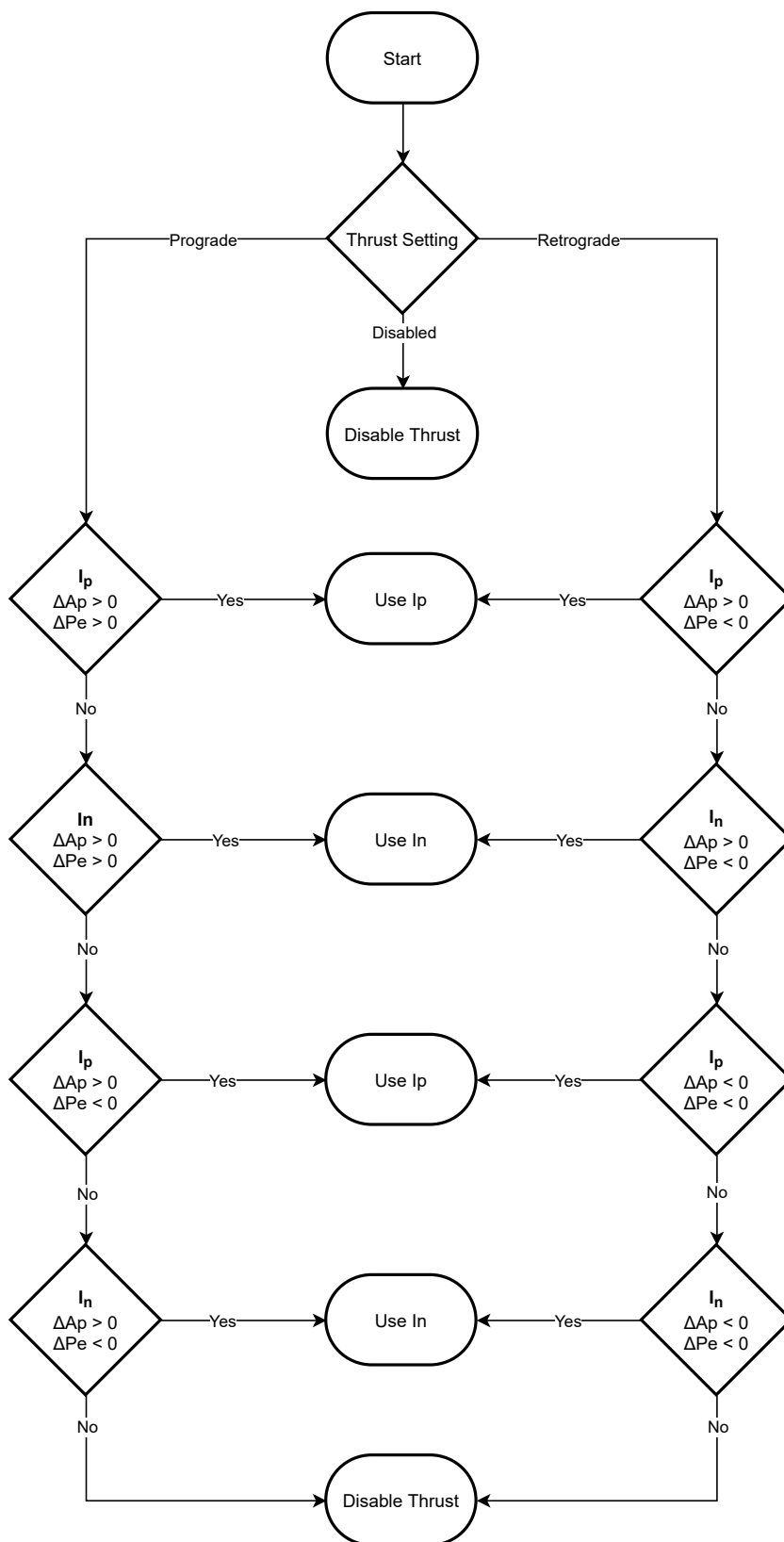
Figure 2.12: Flow chart of guidance logic for EDT current direction vector.

Operation in the ISMF

Once the spacecraft is in the interstellar region, the magnetic field can be considered homogeneous and so thrust can only be applied in the "positive" or "negative" directions. Depending on the location of the spacecraft as it leaves the Solar System, this thrust should be directed in the appropriate direction in order to further increase distance from the Solar System. The ISMF is such that the thrusting directions are approximately oriented in a direction that is rotated at an angle of 45° from the Cartesian x-axis of the Solar System; this can be done since at large distances, the spacecraft trajectory tends towards a straight line.

Therefore in order to provide thrust in an appropriate direction, the Solar System is split up into four quadrants, as shown in Figure 2.13, each denoted by their respective cardinal directions. Also shown in Figure 2.13 as arrows are the possible thrust direction vectors, with the required positive or negative spacecraft direction vector, as previously described in this section, for that particular thrusting direction denoted by a red plus or minus symbol. If the spacecraft finds itself in the South or East quadrants, then it will adopt a positive attitude direction vector, whereas when in the North or West quadrants, it will adopt a negative attitude direction vector.
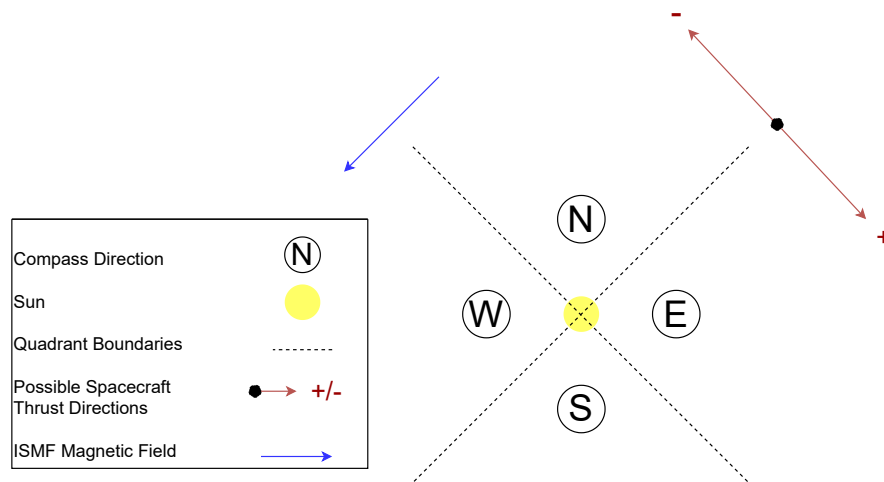

Figure 2.13: Quadrants used to dictate guidance in the interstellar region. Shown are the four compass directions, the overall ISMF direction, as well as the directions available for the spacecraft to thrust and the associated positive or negative orientation vector.

It should be noted that although this model was set up for use in the ISMF, it was found in the final simulations the spacecraft did not enter into the region beyond 100 AU, and so this model was never actually utilised.

3

Simulation Setup

In this chapter, the setup of the optimisation procedures and other simulation parameters is outlined. This is split into 3 main parts: the setup of the preliminary EDT configuration parameter exploration, the setup of the preliminary method of identifying gravity assists to use in the SOKGA trajectories, and finally the setup of the final results simulations, involving how each mission profile will be assessed.

It should be noted that in order not to repeatedly go over the setup of different simulations, Appendix B is introduced here, which provides the default values for every aspect of the simulation environment. Whenever a specific simulation setup is outlined, the values used are the ones listed in Appendix B, unless specifically stated otherwise.

3.1. EDT Configuration Parameter Value Exploration Setup

In order to give the EDT the best chance at feasibility, it is necessary to assess how different EDT configurations affect the final performance of the system, and come to a reasonable reference spacecraft to use when comparing possible trajectory options. To facilitate this an initial parameter value exploration can be conducted, which aims to set well-performing values for each parameter pertaining to the EDT spacecraft configuration, without conducting an exhaustive optimisation procedure for each one.

Some EDT configurations were initially outlined in the literature study to be assessed [46]; however these configurations only pertain to a few of the possible variable parameters. For this parameter exploration, those relatively simple configurations have been expanded upon and are no longer needed. It should be noted that in this setup, only Hoytether configurations are considered, however a single-line configuration is in fact part of the assessment, which is simply a special case of Hoytether in which the number of primary lines is one.

It should also be noted that the parameter exploration is fully conducted for both the bare-tether EDT concept, as well as the transient EDT concept; even though the transient-current case was shown to not be viable, it is included for completeness and a comparison point.

3.1.1. Introduction to EDT Configuration Parameters

A series of parameters are chosen with ranges of values to be adjusted individually, while keeping other base spacecraft parameters the same; this is done in order to reduce both the required simulation time as well as the amount of data that must be analysed. The parameter assessment uses 1000 steps in each range, with some on a logarithmic scale and some linear. The parameters and their chosen ranges are as follows:

Tether length L - the value range chosen is between 1 and 100 km, on a logarithmic scale. Many previous EDT missions have used tethers with lengths in the order 10 km [?], and this range is one order of magnitude above and below this.

Tether diameter D - the value range chosen is 1 - 100 mm, on a logarithmic scale. Previous EDT missions have used varying ranges of tether diameters, and considering the use of several Hoytether lines, a range of both small and large diameters could be useful.

Emitter current I_C - the value range chosen is 1 - 1000 mA, on a logarithmic scale. Space-based current emitters (which would be required for the bare-tether method employed) can operate on the order of 10 mA up to 1000s of mA [17]. In order to give the spacecraft a good chance at feasibility, much larger current values are tested here, although it should be noted that these higher values would adversely affect the spacecraft mass, and focus should predominantly be paid to the sub 100mA range.

Tether area ratio k_A - the value range chosen is 0 - 1, since this encompasses all possible values, on a linear scale. k_A is a newly introduced parameter here, referring to the ratio of material composition in the tether by area; it is introduced here as an easy way to vary the material composition of the tether, and has values between 0 and 1. The cross-sectional area of aluminium or copper in each tether can then be determined using Equations 3.1 and 3.2 respectively, in which A, A_s, and A_c refer to the cross-sectional area of the total tether, the aluminium portion, and the copper portion respectively. A value of 0 corresponds to a pure copper cable, whereas a value of 1 corresponds to a pure aaaaluminium cable.

$$A_s = Ak_A \qquad\qquad\qquad (3.1)$$

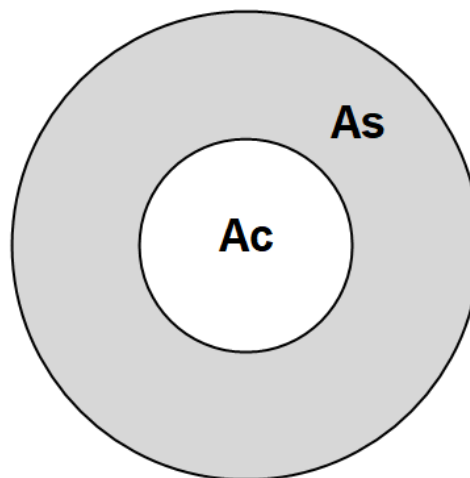$$A_c = A(1 - k_A) \qquad\qquad\qquad (3.2)$$

Figure 3.1: Tether line cross section showing the core area A_c and shell area A_s.

Number of primary lines n - the value range chosen is 1 - 100, on a linear scale. A representative Hoytether has 6 primary lines [16], and therefore an order of magnitude above and below this is chosen.

Primary segment length ratio k_{l_p} - the value range chosen is 0.1 - 1, on a linear scale; very small values are not used since the number of segments in this case would approach infinity. k_{l_p} is a newly introduced parameter here, referring to the ratio between the primary segment length l_p, as defined in Chapter 2, and the overall tether length L; it is introduced as a way to vary the primary segment length in a dimensionless way, so that for a given value of k_{l_p}, each primary line segment takes up the same fraction of the tether, regardless of the overall length. k_{l_p} is defined as shown in Equation 3.3, in which l_p and L refer to the primary segment length and overall tether length respectively.

$$k_{l_p} = \frac{l_p}{L} \tag{3.3}$$

Endmass m_e - the value range chosen is 1 - 100 kg, on a logarithmic scale. Previous EDT missions have been on the order of 10kg endmass [**?**], the smaller values of this range allow microsatellite concepts to be considered, while the larger values allow for larger satellites. The mass refers to the individual mass of each of the two endmasses of the spacecraft.

Rotation coefficient k_{Trot} - the value range chosen is 0.5 - 0.8, on a linear scale. It is known that an EDT can maintain overall thrust in the desired direction approximately 75% of the time; this range allows for slightly better or worse performance than this.

Table 3.1 gives a summary of the above described parameters and ranges, along with the value of the reference spacecraft (against which parameter changes will be made)

Table 3.1: Summary of parameter exploration values, along with their base value and assessment ranges.

Assesment parameter	Symbol	Unit	Base Value	Assessment Range
Tether length	L	km	10	1 - 100
Tether diameter	D	mm	10	1 - 100
Emitter current	I_C	mA	100	1 - 1000
Tether area ratio	k_A	-	0.5	0 - 1
No. primary lines	n	-	10	1 - 100
Primary segment length ratio	k_{l_p}	-	0.5	0.1 - 1
Endmass (individual)	m_e	kg	10	1 - 100
Rotation coefficient	k_{Trot}	-	0.7	0.5 - 0.8

Any EDT configuration parameters not mentioned here were kept constant throughout the assessment, and will be addressed further in the final sensitivity analysis in Chapter 7. It should also be noted that the base values indicated in Table 3.1 are chosen somewhat arbitrarily, unless stated otherwise.

3.1.2. Simulation Setup and Performance Parameters
The simulation settings different from the default ones in Appendix B are shown in Table 3.2, and it should be noted that the performance metrics are the average of the values recorded over the TOF, and the orbit is the default 1 AU Keplerian one.

Table 3.2: Simulation setup parameters for EDT configuration parameter exploration. The ones shown are the differences from default in Appendix B.

Parameter	Symbol	Unit	Value
Include Mercury 3rd Body	-	-	1
Include Venus 3rd Body	-	-	1
Include Earth 3rd Body	-	-	0
Inlcude Mars 3rd Body	-	-	1
Include Jupiter 3rd Body	-	-	1
Include Saturn 3rd Body	-	-	1
Include Uranus 3rd Body	-	-	1
Include Neptune 3rd Body	-	-	1
Guidance Configurations			
Thrust Magnitude Config	-	-	Nominal
Thrust Direction Config	-	-	Nominal Prograde
Initial Ephemeris	t_0	years	2020
TOF Termination	-	years	1
Initial State Coordinate Type	-	-	Keplerian

In addition to the exploration parameters outlined in this section, there are also a number of other parameters which are part of the EDT configuration, but are either kept fixed, or have values directly tied to the exploration parameters. These are outlined in Table 3.3.

Table 3.3: Summary of EDT configuration parameters not addressed by parameter exploration.

Parameter	Symbol	Unit	Behaviour	Value
Hoytether parameters				
Primary line separation ratio	k_a	-	Fixed	100
Secondary tether diameter	D_s	mm	Tied to D	-
Secondary tether area ratio	$k_{A,s}$	-	Tied to k_A	-
Slack coefficient	k_s	-	Fixed	1.005
SRP parameters				
Occultation coefficient	k_{occ}	-	Fixed	0.75
Endmass areas (individual)	A_{end}	m^2	Fixed	1
Endmass radiation coefficient	$k_{rad,end}$	-	Fixed	1.5
Tether radiation coefficient	$k_{rad,teth}$	-	Fixed	1.5
SRP Rotation coefficient	k_{rot}	-	Fixed	0.75

Two parameters were chosen to assess the behaviour and performance of the EDT: average spacecraft thrust and acceleration. Since the simulation settings are very simple, and the thrust of the EDT is small, the average thrust and acceleration values over the simulation period can be used, providing an easy-to-use performance metric.

3.1.3. Handling of Assumption Violations During Simulation

It may be possible that the assumptions of the models used are violated over the course of some simulations, causing the trajectory to break down. An example of this is the assumption that the dimensionless current through the EDT is (much) smaller than 1; when this is violated the generated thrust tends to infinity, causing nonsensical trajectories such as the one shown in Figure 3.2. In this case the thrust grows rapidly reaching a value near infinity at around [x, y] = [0, 2.6], before returning to more sensible values.
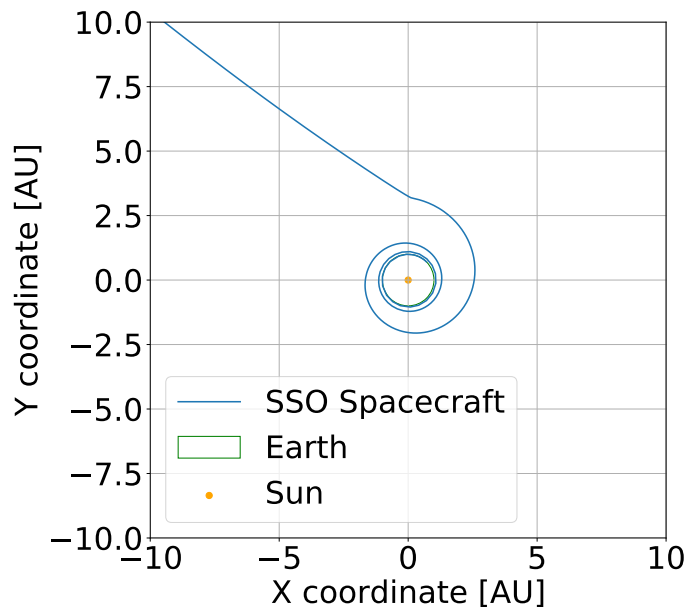

Figure 3.2: Example SSO trajectory with assumtion violations causing nonsensical behaviour.

It was found that the dimensionless current assumption was regularly violated during the parameter exploration simulations, and as such those trajectories are removed from the final analysis. Values that were removed for this reason are summarised in Table 3.4, which shows the tether concept affected, the range of values removed due to assumption violations, as well as the final range of values used for assessment, after the violating ones have been removed. It should be noted that the cutoff value for this assumption violation was any trajectory with an average dimensionless current i_{avg} with a value greater than 0.1.

Table 3.4: Summary of assumption violations during the parameter exploration simulations.

Tether Concept	Assessment Parameter	Violation Range	Final Assesment Range	Units
Bare-tether	Diameter	1 - 2	2 - 100	mm
Bare-tether	Emitter Current	305 - 1000	1 - 305	mA

3.2. Preliminary Gravity-Assist Identification

For some of the proposed simulations, a gravity assist around one of the large planets in the Solar System such as Jupiter or Saturn, in conjunction with a kick-stage from the spacecraft launcher, is used to provide the initial velocity for the spacecraft's journey. This section discusses which trajectories could be used for this purpose, and the methods by which the choices are narrowed down. For the result of this preliminary analysis, refer to Chapter 5.

As a brief overview of how these trajectories are arrived at, a two stage process is used: firstly a Lambert solver is used to find the potential trajectories leading to an intercept with the target planet, the Pareto data points (using injection DV and TOF as target parameters) from this data set of trajectories is then carried onto the second stage. The second stage simply directly runs all the trajectories found from the first stage in the simulation environment itself, selecting the trajectories which perform best (qantified by injection DV and Solar distance after a given TOF) to be taken forward for assessment in the main analysis of the SOKGA mission profile. Figure 3.3 shows the regions governed by the first and second stage of this process. It should also be noted that the Tudat Lambert solver only specifies the minimum allowed flyby distance around the assisting body.
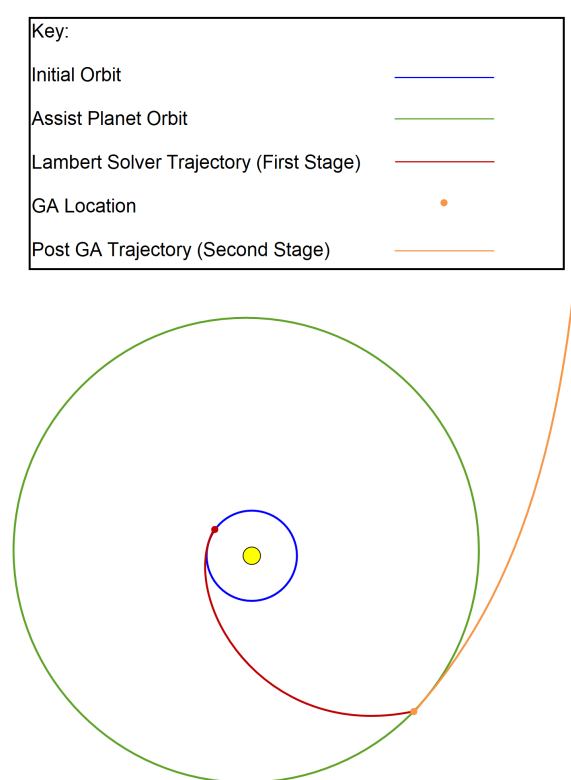

Figure 3.3: Example gravity assist trajectory, in which the initial trajectory to the assisting body is found by the Lambert solver trajectory (red), and the second stage simulation process after the gravity-assist (orange). Also shown are the initial spacecraft orbit and assisting body orbit depicted as blue and green lines, as well as the gravity-assist location depicted as an orange point.

3.2.1. Initial Lambert Solver Optimiser

For the intial stage of determining gravity-assist cases to utilise, it is first necessary to determine which cases are viable from Earth orbit. To do this, the framework set out in Tudat for the calculation of patched-conic Lambert trajectories is used, along with the PaGMO optimisation routines to find a number of viable solutions. The solutions are bounded by three variables: the launch date, time of flight (TOF), and DV requirement, which can be seen in Table 3.5. It was decided to only consider Jupiter and Saturn gravity assists, since these are the most massive bodies and therefore are most likely to provide useful contributions to optimise trajectories.

Table 3.5: Constraints for the Lambert solution optimisation, and Hohmann trajectory information for both Jupiter and Saturn.

Constraint Type	Jupiter	Saturn	Units
Launch date range	2021 - 2050	2021 - 2050	-
Hohmann time of flight	2.73	6.05	years
Hohmann DV	8.8	10.3	km/s
Time of flight constraints	1 - 5	2 - 15	years
DV constraints	8.5 - 9.68	10 - 11.33	km/s

The reasoning for choosing these bounds is as follows: the launch date should be some time from the current year (2021) to the relatively near future, which was chosen to be 2050, 30 years in the future, which was chosen fairly arbitrarily but provides a good length of time for a potential mission to be developed and built; in addition to this it also represents a fair amount of time to encompass varying parameters such as the Solar cycle. Secondly, the TOF for a Jupiter trip is given a lower bound of 1 years to help restrict the search space, since a TOF lower than this is really infeasible as it is much lower than the Hohmann TOF; the upper bound is set to 5 years, again fairly arbitrarily to restrict the search space, but to also allow some freedom in the possible trajectories. Finally the DV of the injection manoeuvre should be bounded at the upper level to account for what could reasonably be provided by a launcher / kick-stage; in this case the upper bound is set to the Hohmann transfer DV from an Earth-radius orbit around the Sun, rounded up by about 10% to allow for some additional launch dates or faster transfers. The DV lower bound is given for the same reason as the TOF lower bound: to restrict the search space. And again is chosen to be around the same as the Hohmann DV, since without other assists it is not possible to get much lower than this value. Although some better DVs may be possible depending on the geometry of the Earth-Jupiter situation (for example launching at Earth aphelion, and arriving at Jupiter perihelion).
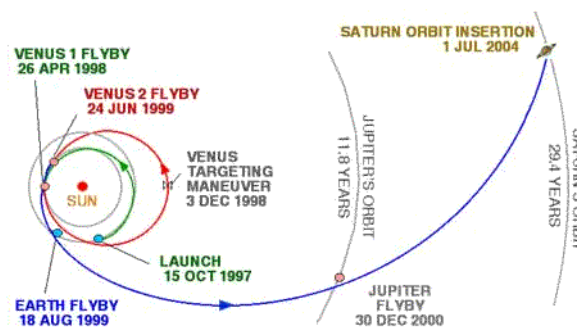

Figure 3.4: Example of a Jupiter gravity assist used by Cassini [43].

The optimiser used to generate the gravity-assist trajectories is readily built into the Tudat environment, using a combination of the Tudat Lambert solver, in conjunction with the PaGMO optimisation algorithms. The implementation is very similar to that of the Earth-Mars example problem shown in the Tudat documentation [44]. The MOEAD algorithm was chosen with default settings defined by the Tudat environment, an island size of 1000, and 100 generations. This algorithm was chosen since it is known to be effective for use-cases such as this one [20]; the island size and number of generations were chosen to be far larger than needed, in order to ensure convergence (which could be done due to the short simulation runtimes), and the remaining settings specific to MOEAD were left to the Tudat defaults, since these generally produce acceptable results.

Another step taken to ensure population diversity was to run the optimiser in two modes: global and synodic. In the global mode, the optimiser is simply given the range of dates and directly optimises within that range. This can introduce issues where a narrow range of dates are found, which is not ideal for the purposes of this study, since many trajectories across a wide range of dates is required to fully explore the range of possible solutions. Therefore the second mode of synodic optimisation is also introduced, which runs an individual optimisation across every synodic period for the transfer between Earth and the gravity-assist target planet; this period is approximately one year for both Earth-Jupiter and Earth-Saturn cases.

Additionally the minimum pericenter radius from the assisting body is specified for each planet, using the values provided by default in Tudat [14], and are shown in Table 3.6; a maximum precienter radius is not specified however, and may be anywhere within the body's sphere of influence.

Table 3.6: Minimum precienter radius used for each planet during a gravity-assist [14].

Planet	Minimum Radial Distance During Assist [km]
Mercury	2640
Venus	6252
Earth	6578
Mars	3596
Jupiter	72000
Saturn	61000
Uranus	26000
Neptune	25000

3.2.2. Second-Stage Gravity-Assist Analysis

The initial Lambert optimiser stage provides a range of possible gravity-assist trajectories; however the number of possible trajectories is far too large to individually simulate each one during the later SOKGA mission profile optimisation. Therefore a second stage of analysis must be conducted in order to put forward only the most optimal trajectories.

The method for achieving this is to take each of the trajectories found by the first-stage Lambert solver and fully simulate them (numerically within the simulation environment) for a set period of time; there are two parameters which define the performance of these gravity assist-trajectories, in the concept of an EDT mission. Firstly the required launch DV, which should be minimised, and secondly the distance from the Sun achieved after a given simulation time, which should be maximised. The justification for minimising DV is quite clear, in that it enables a smaller and less massive kick stage to be used in an eventual mission, but the final distance achieved is also an important parameter: in the case of the EDT missions assessed in this

study, the goal is to reach further out into the Solar System in a reasonable time, and so those trajectories that can achieve longer Solar distances in a shorter time period are of course more optimal.

The simulation method in this case uses the general simulation environment developed for the main EDT simulations, but with many of the features disabled; the simulation setup is as shown in Table 3.7.

Table 3.7: Simulation setup parameters for second-stage gravity-assist optimisation. The ones shown are the differences from default in Appendix B. It should also be noted that only one of the Jupiter or Saturn bodies are enabled, depending on the assisting body; also the initial coordinates are of course different for each assist trajectory, and are obtained from the first-stage analysis.

Parameter	Symbol	Unit	Value
Include Mercury 3rd Body	-	-	0
Include Venus 3rd Body	-	-	0
Include Earth 3rd Body	-	-	0
Inlcude Mars 3rd Body	-	-	0
Include Jupiter 3rd Body	-	-	1
Include Saturn 3rd Body	-	-	1
Include Uranus 3rd Body	-	-	0
Include Neptune 3rd Body	-	-	0
Guidance Configurations			
Thrust Magnitude Config	-	-	disabled
TOF Termination	-	years	10
Initial State Coordinate Type	-	-	Cartesian

The reason for running the simulation in a second stage like this instead of doing this kind of analysis directly with the Lambert optimiser stage is primarily practical: the Tudat Lambert solver requires a start and end destination [14], and no information is (directly) given about the spacecraft trajectory after an encounter. Since the simulation environment has already been developed, it is a fairly trivial task to further numerically propagate the Lambert trajectories, instead of finding another (possibly more elegant) solution.

It should be noted that this second stage is not an optimisation, but simply an assessment of the promising trajectories found by the Lambert solver, in order to remove any sub-optimal trajectories.

3.3. Mission Profile Analysis Setup
A number of mission profile types have been chosen for analysis whose utility can be individually assessed, using the EDT configuration that will be chosen in Section 5.1. These different mission profiles are specified and briefly outlined below and in Table 3.8. It should also be noted that two further trajectories, EDGE and α-c, were originally considered, but were subsequently removed from analysis due to time constraints. EDGE is short for Edge of the Solar System, and would aim to have a prolonged mission at the Solar System edge, near the heliospheric interface, while α-c would be an interstellar mission profile, with the intention of gauging the time it would take for an EDT to reach alpha centauri.

Table 3.8: Summary of mission profiles for investigation, HI and IM stand for Heliospheric Interface and Interstellar Medium respectively. Entries in brackets refer to those profiles that were initially intended to be included, but were removed due to time constraints.

Mission Designation	Mission Target
SSO+	Far outer Solar System, HI
InO	Far outer Solar System, HI
SOKGA	Far outer Solar System, HI, IM
(EDGE)	(Far outer Solar System, HI)
(α-c)	(IM)

Each of the above-mentioned trajectories is further outlined below; for a more thorough description of these trajectories and the justification for their choice, one should refer to the literature study [46].

- SSO+ - Simple-Straight-Out+ - This profile has evolved from the original SSO profile, and acts as a baseline profile. During development it was found that the EDT had significantly lower performance than expected, therefore the SSO profile which was planned to start in a circular 1AU orbit was modified into the SSO+ profile, which allowed a kick-stage impulse to be utilised. After this, the spacecraft is set on the "prograde" guidance mode, and the simulation is run for a particular length of time to see how much the orbit is altered by the EDT. It is the simplest of the mission profiles, aiming simply to get as far as possible from the Sun, and provides something to compare the other proposed profiles to.

- InO - Inner Solar system, Out - this profile first sends the spacecraft to the inner Solar System, with a combination of kick-stage and EDT propulsion, taking advantage of the increased thrust in that region, before eventually venturing out into the wider Solar System. Like the SSO+ profile, InO simply aims too get as far into the outer Solar System as possible in the given time frame.

- SOKGA - Straight-Out with Kickstage and Gravity Assist - This profile is similar in goal to SSO+, but the spacecraft first receives a more directed initial kick, allowing it to take advantage of a gravity assist to propel itself more quickly into the outer Solar System, where an EDT is expected to have better performance relative to its contemporaries.

3.3.1. Optimisation Parameter Selection

In order to give the EDT propulsion concept a good chance at feasibility, optimising different simulation parameters to improve overall performance is essential. First it is necessary to define, for each mission profile, what constitutes good performance, and therefore which parameters are optimised.

In all cases, the perspective being analysed in this study is the use of an EDT as a main propulsion system; therefore there are three simulation parameters governing the EDT performance: achievable Solar distance, TOF to reach that distance, as well as the velocity at that distance. These performance parameters are the same across all mission profiles.

Between each mission profile however, there are several different parameters able to alter the effectiveness of the trajectory; not all of these parameters are applicable to each profile type, and the assessable ranges between parameters may also vary. The parameters and bound ranges chosen for each optimisation parameter can be seen in Table 3.9; each row shows the parameter, and each column the type of trajectory, a "-" symbol signifies that the specified

parameter is not valid for use on that particular trajectory. Initial Ap and Pe refer to the initial aphelion and perihelion respectively of the EDT spacecraft orbit; target perihelion refers to the perihelion that the EDT spacecraft should target in the first stage of its trajectory, and is only applicable to the InO mission profile.

Table 3.9: Bound ranges for chosen optimisation parameters.

Parameter	SSO +	InO	SOKGA
Launch Year	2025 - 2050	2025 - 2050	-
Initial Ap [AU]	1 - 10	1	-
Initial Pe [AU]	1	0.3 - 1	-
Target Pe [AU]	-	0.1 - 0.9	-

Table 3.9 is mostly self-explanatory, however the details of the specific ranges chosen for each parameter on each trajectory are outlined in the following subsections. It should be noted that the launch date range where applicable is always between 2025 and 2050, this is to ensure a range of possible start dates in the near future, covering several Solar cycles.

3.3.2. Optimiser Selection and Setup
Throughout the optimisations that are being run, generally two methods are used; for single-objective optimisations the Differential Evolution (DE) optimisation algorithm included in PaGMO and PyGMO is used, whereas for multi-objective optimisations its related multi-objective algorithm MOEAD is used. These are chosen as they generally provide a good option for orbit-based simulations [20]; for a more in-depth description of these choices, one should refer to the literature study [46].

The settings used for these algorithms is generally kept to the default parameters, as described in the pygmo.de class description of the PyGMO documentation for the DE algorithm, and the pygmo.moead class description of the PyGMO documentation for the MOEAD algorithm [7]; default parameters can be chosen since the optimisation is quite straightforward, and these settings work well. The population and number of generations can be changed between simulations, and will be described in further subsections on a case-by-case basis. It should also be noted that in order to show the robustness of the optimisation, two runs were made, with different seed numbers (which triggers a different series of quasi-random numbers).
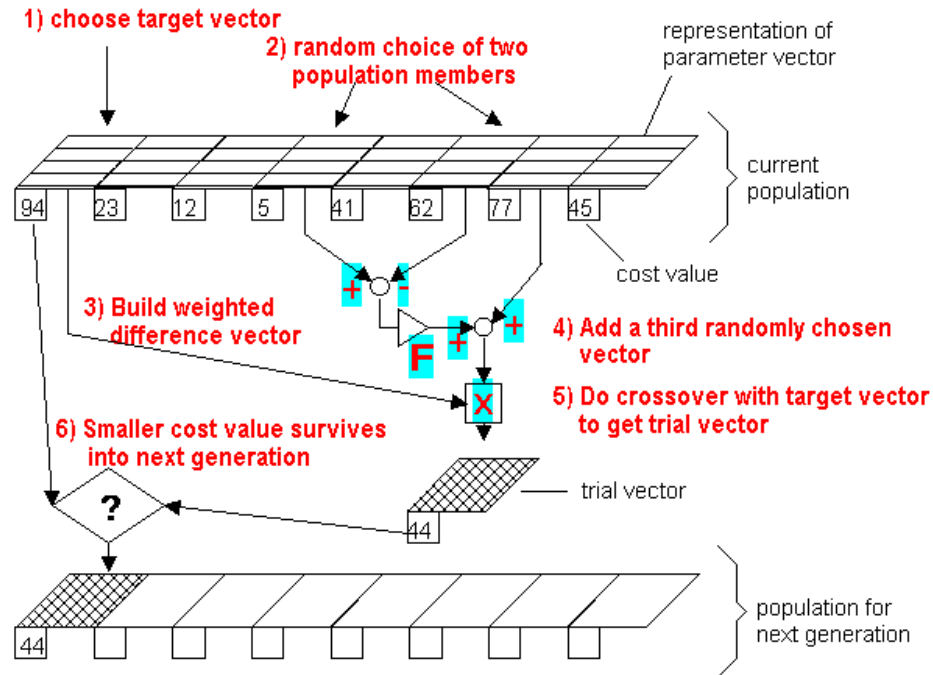
Figure 3.5: Differential Evolution optimisation implementation in PaGMO [8].

3.3.3. SSO+ Profile Optimisation Setup

For the SSO+ optimisation case, the launch year, initial aphelion and initial perihelion are able to be modified as optimisation parameters. The launch year range is chosen as described in Table 3.9, the initial aphelion range has a lower bound of 1 AU, the distance of the Earth from the Sun, and an upper bound of 10 AU, which corresponds to an initial kick stage DV of approximately 10 km/s, which is representative of modern kick stages. The initial perihelion is fixed at 1 AU, since in this profile, the spacecraft would not use its kick stage to reduce the perihelion.

The simulation settings used for SSO+ optimisations can be seen in Table 3.10, in which the orbit parameters used are indeed the default ones.

Table 3.10: Simulation setup parameters for SSO+ profile optimisation. The ones shown are the differences from default in Appendix B.

Parameter	Symbol	Unit	Value
Guidance Configurations			
Thrust Magnitude Config	-	-	Nominal
Thrust Direction Config	-	-	Nominal Prograde
TOF Termination	-	years	100
Initial State Coordinate Type	-	-	Keplerian

The optimisation goal in this case was chosen to simply be the maximum achievable aphelion, over a fixed simulation period, which should be maximised. This can be done since the thrust is very small, and so the orbit is unable to achieve a hyperbolic trajectory. It should be noted that this is then a single-parameter optimisation, and as such the DE optimiser can be used,

with the following population properties:

- Population size = 1000

- Number of generations = 100

3.3.4. InO Profile Optimisation Setup

For the InO optimisation case, the launch year, initial aphelion, initial perihelion and target perihelion are able to be modified as optimisation parameters. The launch year range is chosen as described in Table 3.9, the initial aphelion range is fixed at 1 AU, since in this profile the spacecraft would not use its kick stage to raise the orbit initially. The initial perihelion range has an upper bound of 1 AU, simply the Earth's orbit altitude, and a lower bound of 0.3 AU, which corresponds to an initial kick-stage DV of approximately 10 km/s, which is representative of modern kick stages. Finally, the target perihelion is chosen relatively arbitrarily between 0.1 and 0.9 AU, much of which can be provided by the initial kick stage. It should be noted that while in some cases the target perihelion is already achieved at the simulation start, it is still a parameter to optimise for, since it determines at what point the EDT should switch operation mode when the perihelion does not follow directly from the initial conditions.

Naturally the simulation is split into two stages, the first using a retrograde guidance logic in order to achieve the required perihelion, and the second stage utilising prograde guidance logic to raise the aphelion; the simulation switches from stage one to stage two when the target perihelion is reached. The simulation settings used for InO optimisations can be seen in Tables 3.11 and 3.12, which represent the first and second stage setups respectively, in which the orbit parameters used are indeed the default ones for the first stage, and for the second stage the initial conditions are obtained from the final second stage state. The total TOF is 100 years, and the first stage is terminated when the target perihelion is reached.

Table 3.11: Simulation setup parameters for stage 1 InO profile optimisation. The ones shown are the differences from default in Appendix B.

Parameter	Symbol	Unit	Value
Guidance Configurations			
Thrust Magnitude Config	-	-	Nominal
Thrust Direction Config	-	-	Nominal Retrograde
Termination Type	-	-	Proximity Termination
Proximity Termination Body	-	-	Sun
Proximity Termination Value	-	AU	Target Perihelion
Initial State Coordinate Type	-	-	Keplerian

Table 3.12: Simulation setup parameters for stage 2 InO profile optimisation. The ones shown are the differences from default in Appendix B. It should be noted that the TOF termination is set so that the total TOF is 100 years.

Parameter	Symbol	Unit	Value
Guidance Configurations			
Thrust Magnitude Config	-	-	Nominal
Thrust Direction Config	-	-	Nominal Prograde
Termination Type	-	-	Nominal TOF Termination
TOF Termination	-	years	100 - Stage 1 TOF
Initial State Coordinate Type	-	-	Cartesian

The optimisation goal in this case, as with the SSO+ case, was chosen as the maximum achieved aphelion, for the same reasons as the SSO+ case, which should be maximised. Similarly a single-objective DE optimisation algorithm is used with population properties:

- Population size = 1000

- Number of generations = 100

3.3.5. SOKGA Profile Optimisation Setup

For the SOKGA optimisation case, all initial parameters are dictated by the specific gravity assist, and therefore no (further) optimisation on them needs to take place. The gravity assist trajectories to be specified in Section 5.2 are small enough in number that it is possible to simply simulate all of them with an operational EDT, and analyse them together.

Regarding simulation settings, the simulation is split into two stages, in which the first is the initial coast phase to the gravity assist body, followed by the second stage is the EDT thrusting stage, as the spacecraft leaves the Solar System on a hyperbolic orbit. The specific point at which stage 1 transitions into stage 2 (i.e. when the EDT is activated) is the moment at which the spacecraft leaves the SOI of the assisting body. The simulation settings for each stage are slightly different, shown in Tables 3.13 and 3.14; it should be noted that the initial coordinates are determined depending on the gravity-assist trajectory, and the final simulation termination is done at 100 AU, where the IMF ends.

Table 3.13: Simulation setup parameters for stage 1 SOKGA profile optimisation. The ones shown are the differences from default in Appendix B. The proximity termination body and value are shown for both Jupiter and Saturn respectively.

Parameter	Symbol	Unit	Value
Include Mercury 3rd Body	-	-	0
Include Venus 3rd Body	-	-	0
Include Earth 3rd Body	-	-	0
Inlcude Mars 3rd Body	-	-	0
Include Jupiter 3rd Body	-	-	1
Include Saturn 3rd Body	-	-	1
Include Uranus 3rd Body	-	-	0
Include Neptune 3rd Body	-	-	0
Guidance Configurations			
Thrust Magnitude Config	-	-	disabled
Termination Type	-	-	Proximity Termination
Proximity Termination Body	-	-	Jupiter / Saturn
Proximity Termination Value	-	AU	0.32 / 0.36
Initial State Coordinate Type	-	-	Cartesian

Table 3.14: Simulation setup parameters for stage 2 SOKGA profile optimisation. The ones shown are the differences from default in Appendix B. The initial coordinates are obtained from the final coordinates of the first stage.

Parameter	Symbol	Unit	Value
Include Mercury 3rd Body	-	-	0
Include Venus 3rd Body	-	-	0
Include Earth 3rd Body	-	-	0
Inlcude Mars 3rd Body	-	-	0
Include Jupiter 3rd Body	-	-	1
Include Saturn 3rd Body	-	-	1
Include Uranus 3rd Body	-	-	0
Include Neptune 3rd Body	-	-	0
Guidance Configurations			
Thrust Magnitude Config	-	-	nominal
Termination Type	-	-	Distance Termination
Proximity Termination Body	-	-	Sun
Proximity Termination Value	-	AU	100
Initial State Coordinate Type	-	-	Cartesian

Since the spacecraft on a SOKGA trajectory are generally in a hyperbolic orbit, the maximum achieved aphelion optimisation goal cannot be used like it was for the SSO+ and InO cases. Therefore two optimisation parameters are introduced to assess the trajectories: spacecraft velocity and TOF upon reaching a particular Solar distance. These goals were chosen since they provide a good allegory for the overall performance of the EDT; the shorter the TOF to a particular distance, the shorter a potential mission can be, and the higher the velocity at that location the further out that mission can reach.

The distance at which the simulations terminate was chosen to be 100 AU, since this is the nominal edge of the Solar System, where the magnetic field modelling switched from interplanetary to ISMF in the spherical Solar magnetic field model. The justification for this distance is that it fully assesses the spacecraft performance within the Solar System, which is where the SOKGA trajectory is most pertinent; in the case that a trajectory does not reach 100 AU at all it is simply removed from consideration.

4

Verification and Validation

In this section verification and validation efforts are performed in order to confirm that the simulation environment can be safely used in further simulations. This includes the assessment of various environment models as well as the main simulation components such as current and thrust generation models.

4.1. Magnetic Field Model Verification

After the decision to split the magnetic field modelling into two regions, namely interplanetary and interstellar, the verification and validation efforts can naturally be separately considered for these regions. The efforts are also distinctly divided between verification, which evaluates that the modelling is working as intended, and validation, which evaluates that the models represent reality to a sufficient degree.

4.1.1. Parker Model Verification

Firstly the Parker model used in the interplanetary region can be verified using the reference data found in Ferreira 2007 [15], which is shown in Figure 4.1.

The magnetic field strength data for the Parker model used in Ferreira 2007 [15] was extracted and plotted in Figure 4.2, alongside the strength outputted by the Tudat simulation, with nominal input values as determined in Chapter 2; it should be noted that the Solar cycle variations were removed in the simulation, as these are also not accounted for in Ferreira 2007 [15].
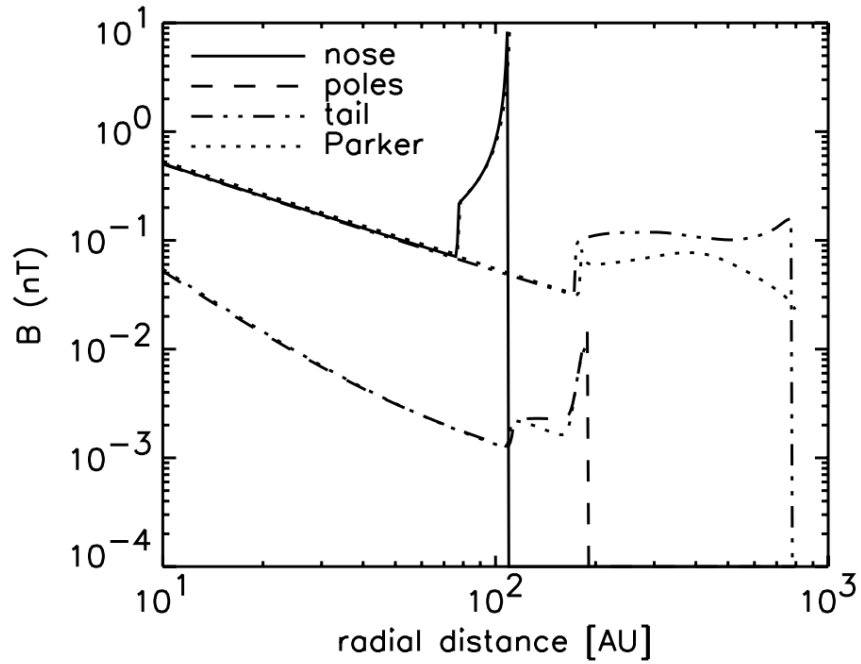
Figure 4.1: Reference Parker model magnetic field strength data [15].
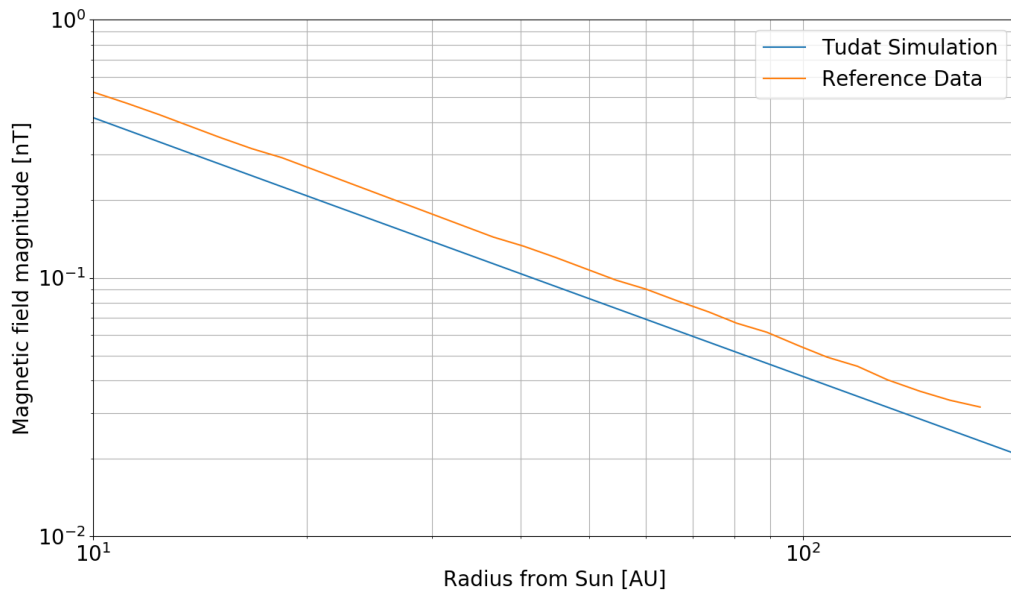
Figure 4.2: Reference Parker model from literature (orange), compared against the Tudat simulation data (blue).

From Figure 4.2, it can be seen that the two models exhibit very similar behaviour over the plotted radius regime, but with a slight, consistent relative offset between the two datasets. This offset is both small, being within the uncertainty range of other factors (see further in this section), and the simulated strength is conservative compared to the reference data. Therefore the magnetic field strength of the implemented Parker model can be considered verified.

4.1.2. Interstellar Model Verification

Due to the inherently simple nature of the interplanetary magnetic field model used, namely a homogeneous one, verification is quite straightforward; the output of the simulated magnetic field in the interstellar region (i.e. beyond 100 AU) is compared directly against the values decided upon in Chapter 2. When doing this, one finds that the values are identical to those in Table 2.3, as expected.

4.1.3. Parker Model Validation

As well as verifying the implementation of the Parker model, it is also prudent to validate it using real world data. In this case Voyager data was chosen, since the data is freely available, and provides direct data from 1 AU to extreme distances from the Sun, which can be seen in Figure 4.3.
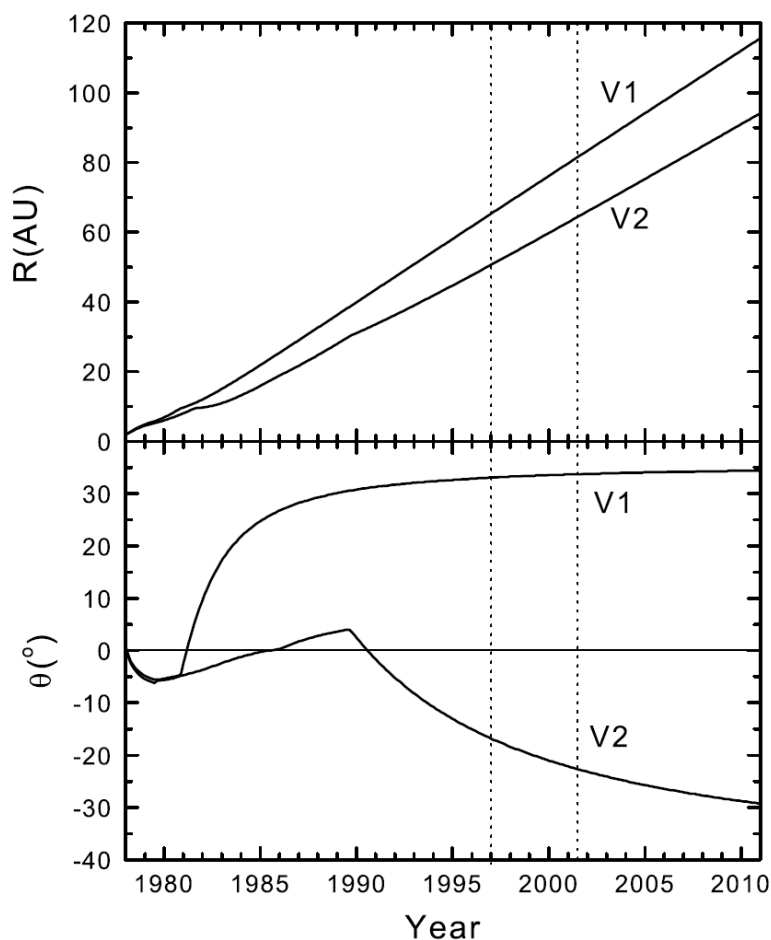
Figure 4.3: Voyager 1 (V1) and Voyager 2 (V2) data on radius from Sun and magnetic field direction over time [10].

Magnetic field measurements from both Voyager 1 and 2, as well as the Tudat simulated magnetic field strength, can be seen in Figure 4.4; it should be noted that the nominal implementation described in Chapter 2 is used, with the simulated spacecraft travelling in a similar time period as that of the Voyager spacecraft, on a fairly arbitrarily chosen hyperbolic orbit with parameters as shown in Table 4.1.

Table 4.1: Orbit parameters chosen for the verification and validation spacecraft used for the Parker magnetic field.

Parameter	Value	Unit
a	-3.34	AU
e	1.3	-
i	0	deg
AOP	180	deg
RAAN	0	deg
TA	0	deg

Also useful to note is the level of uncertainty in the Voyager data, which varies per dataset as shown in Table 4.2; something to bear in mind with these uncertainties however is that no information on the confidence level of these ranges is provided in the literature, and Behannon [5] also states a contradictory uncertainty value of 0.09 nT for all measurements. However, the discrepancy is small and so the presented values can still be used for this study.

Table 4.2: Uncertainty levels for Voyager datasets. Later measurements are able to achieve smaller uncertainties using post-processing techniques [5].

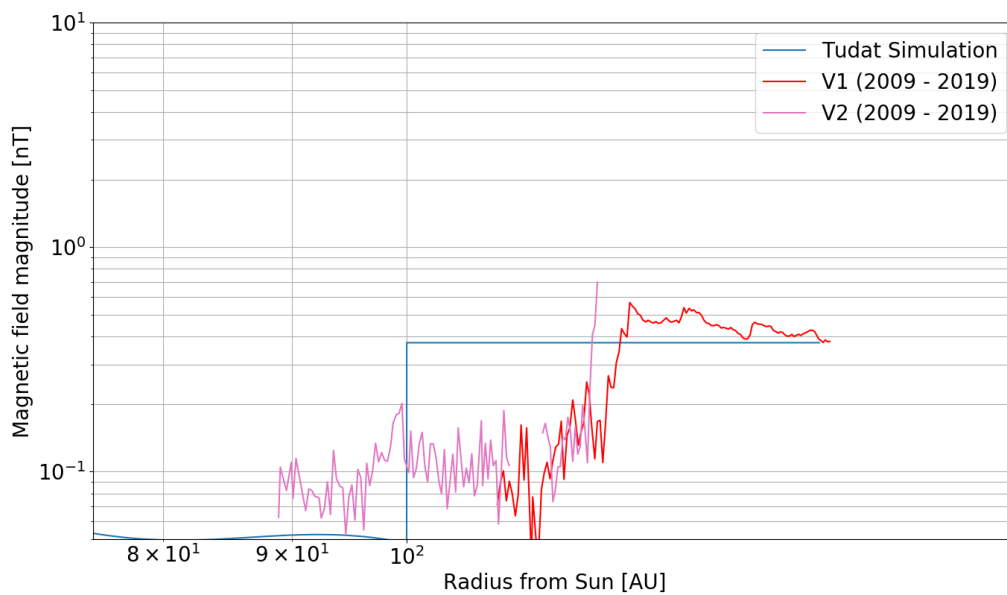| Time period	Uncertainty [nT]
1977 - 1989	$\pm$ 0.05
1990 - 2004	$\pm$ 0.02
2009 - 2019	$\pm$ 0.02
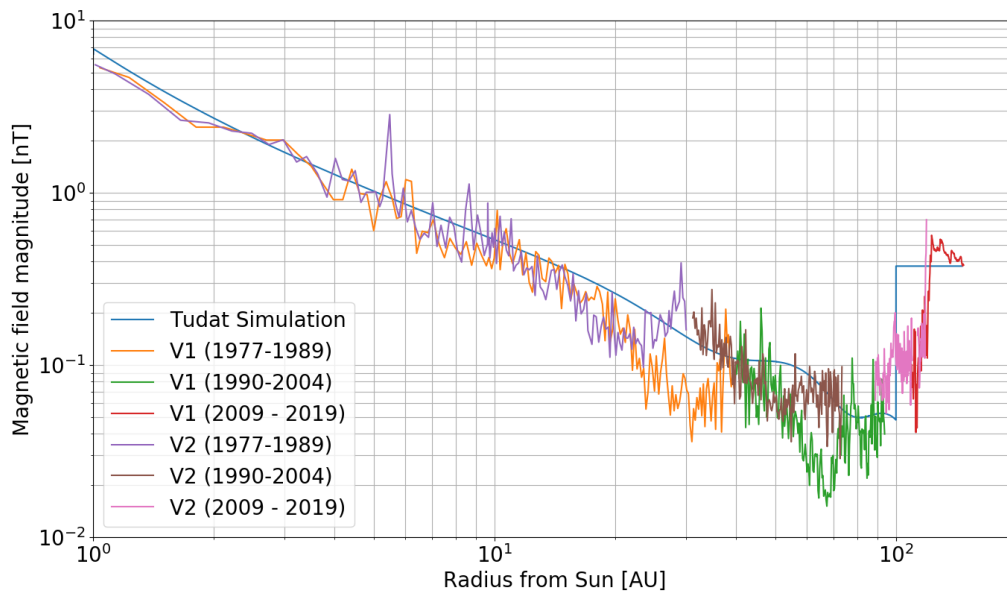
Figure 4.4: Magnetic field strength with distance from the Sun, for the simulation environment (blue), and reference Voyager 1 (V1) data (orange and green), and Voyager 2 (V2) data (red and purple) [23].

It can be seen in Figure 4.4 that the simulated magnetic field strength has qualitatively similar behaviour to the Voyager spacecraft, especially for smaller distances from the Sun. Beyond around 10 AU the simulated data, as well as the two sets of Voyager data, begin to diverge from one-another somewhat, however the overall differences are quite manageable. Therefore the Parker model up to approximately 100 AU can be considered validated. The differences between the simulated model and the Voyager data can also be used as a basis for later sensitivity studies.

It should be noted that the difference in behaviour between the two Voyager vehicles can be explained using Figure 4.3, which shows two things. Firstly the upper portion of Figure 4.3 shows that the two spacecraft are not at the same distance from the Sun at a given time, and so must be experiencing different levels of Solar activity as they pass a particular radial distance. Secondly, the two spacecraft travel along much different trajectories, one making its way in the direction of Solar North and the other in Solar South, which can be seen in Figure 4.5 [11].
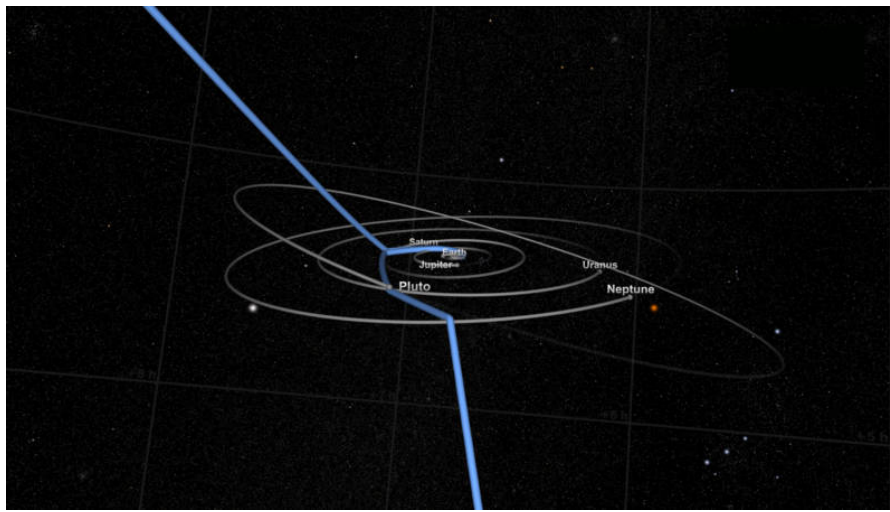
Figure 4.5: Voyager 1 and 2 trajectories, heading to Solar North and South respectively [11]

4.1.4. Interstellar Model Validation

Also shown in Figure 4.4 is the behaviour of the magnetic field in the interstellar region, beyond approximately 100 AU. In the nominal simulation environment, 100 AU is chosen as the transition between the interplanetary and interstellar regimes, in accordance with Ferreira 2007 [15]. For a more detailed view of the interstellar data, refer to Figure 4.6.

Figure 4.6: Magnetic field strength with distance from the Sun, for the simulation environment (blue), and reference Voyager 1 (red) and Voyager 2 (pink) data [23]. The plot is a zoomed in at the interstellar region shown in Figure 4.4.

From Figure 4.6, it can be seen that in the region surrounding 100 AU, where the interplanetary regime transitions into the interstellar regime, the simulation environment does a relatively poor job predicting the magnetic field strength. However, beyond the transitioning region, once the magnetic field strength settles into the interstellar regime, Figure 4.6 shows that the simulation environment does a much better job of predicting the magnetic field strength, as shown by the Voyager 1 data in red. With these considerations, the magnetic field modelling in the simulation environment can be considered validated in the interstellar regime, with uncertainties quantified for use in the sensitivity study. It should be noted that although it appears the switch from an IMF to ISMF model should maybe occur at a slightly further solar distance than 100 AU, this is a logarithmic scale plot, meaning a crossover point of 100 AU is sufficient here.

4.2. Current and Thrust Modelling Verification and Validation

In this section the current models described in Chapter 2 will be verified and validated, along with the thrust produced, as this is just one step further in the calculation process. Verification is fairly straightforward, as the simulated values can be directly compared against expected outputs given some initial conditions, using hand calculations of the equations described in Chapter 2. Validation however is somewhat more difficult, due to the novel nature of the field and corresponding lack of previously completed missions or simulations, with access to the relevant data; therefore validation for these aspects can be done somewhat indirectly using a higher-level validation process further described in Subsection 4.2.1.

As previously mentioned, the thrust and current can be verified at each stage of the calculation process against a series of hand calculations using the relevant equations, with each intermediary value being compared against the simulated values. In order to fully verify the model implementation, a number of verification cases were chosen, to test the simulation with

a range of possible input parameters; these verification cases are designated and described in Table 4.3.

Table 4.3: Description of various cases used in current verification.

Verification Case	Description
1	Representative case, with positive current orientation
2	Representative case, with negative current orientation
3	Values arbitrarily randomly generated, with values of the same order of magnitude as cases 1 and 2.

Firstly, the input parameters for each case must be chosen and specified. This is done in Table 4.4, in which **V**, **B**, **I** are vectors referring to spacecraft velocity, magnetic field strength, and spacecraft pointing vector (i.e. the unit vector indicating the direction of the tether and therefore direction of current flow) respectively; σ, A, I_c, and L refer to the tether conductivity, cross-sectional area, current at point C on the tether (refer to Figure 2.8), and length respectively.

Table 4.4: Base parameters used in the current model verification, for each verification case.

Verification Case	V	B	I	σ	A	I_c	L
Units	m/s	nT	-	S/m	m^2	A	m
1	$\begin{pmatrix} 0 \\ 30000 \\ 0 \end{pmatrix}$	$\begin{pmatrix} 4.782 \\ 4.420 \\ 0 \end{pmatrix}$	$\begin{pmatrix} 0 \\ 0 \\ 1 \end{pmatrix}$	4.86×10^7	4.704×10^{-4}	0.002	10
2	$\begin{pmatrix} 0 \\ 30000 \\ 0 \end{pmatrix}$	$\begin{pmatrix} 4.782 \\ 4.420 \\ 0 \end{pmatrix}$	$\begin{pmatrix} 0 \\ 0 \\ -1 \end{pmatrix}$	4.86×10^7	4.704×10^{-4}	0.002	10
3	$\begin{pmatrix} -3180 \\ 16020 \\ 18690 \end{pmatrix}$	$\begin{pmatrix} 1.413 \\ -1.126 \\ -5.215 \end{pmatrix}$	$\begin{pmatrix} 0.176 \\ 0.875 \\ -0.450 \end{pmatrix}$	5.952×10^7	5.00×10^{-3}	0.0372	531

For verification case 1, the values chosen correspond to a nominal simulation, occurring in a circular Solar orbit, with semi-major axis of (approximately) 1 AU, on January 1st 2000; the velocity was rounded to 30 km/s for ease of calculation, and the magnetic field strength corresponds to a nominal case for this region, according to the model laid out in Chapter 2. The spacecraft pointing vector **I** is chosen to provide a force in the positive direction (i.e. to raise the orbit), while σ, A, I_c, and L are all chosen according to nominal values for a representative spacecraft.

Verification case 2 uses identical base parameters as verification case 1, with the exception that the spacecraft pointing vector was reversed, to produce a negative thrust.

Finally, verification case 3 utilises randomly generated values for all parameters, in order to fully test the robustness of the simulated environment. These randomly generated values are bounded in such a way to keep them "reasonable"; this was done by taking the values for the nominal case and scaling them accordingly. The main advantage of using arbitrary values for this test is that the model can be verified without the many null values present in the vectors of the nominal cases (avoiding the inherent risks).

The results of the verification can be seen in Table 4.5, in which E_m, I_0, i_c, λ_A, i_{avg}, I_{avg}, and F refer to the motional electromotive potential difference across the EDT, unit current, dimensionless current at C, dimensionless voltage at A, average dimensionless current, average true current, and thrust generated respectively.

Table 4.5: Verification of current modelling implementation using hand calculations, compared against a single instance of simulation data, for each verification case. Each case also has an "S" and "R" beside it, denoting if the given data is Simulation (obtained from the simulation environment), or Reference (obtained via hand calculation).

Verification Case	E_m	I_0	i_c	λ_A	i_{avg}	I_{avg}	F
Units	10^{-5}V	A	10^{-4}	-	10^{-4}	A	10^{-11}N
1S	-143.4600	-32.7970	-0.6098	0.0025	0.6098	-0.0020	13.0228
1R	-143.4600	-32.7970	-0.6098	0.0025	0.6098	-0.0020	13.0228
2S	143.4600	32.7970	0.6098	0.0025	0.6097	0.0020	13.0220
2R	143.4600	32.7970	0.6098	0.0025	0.6097	0.0020	13.0220
3S	327.7457	975.3711	0.3814	0.0018	0.3814	0.0372	10422.3999
3R	327.7457	975.3711	0.3814	0.0018	0.3814	0.0372	10422.3999

Table 4.5 shows that for all final and intermediary values, the hand calculated results and simulation results are identical to 5 significant figures, concluding the verification process.

It should be noted that already at this stage the found values for thrust shown in Table 4.5 are not promising, being on the order of 1 nN. While not necessarily being completely accurate this produces performance several orders of magnitude short of feasibility: with a 1000kg spacecraft this would produce a velocity change over 10 years of only 0.0003 m/s. This could be improved somewhat with configuration alterations, but even several orders of magnitude of improvement would still be inadequate. This inadequacy was not able to be directly identified in the literature study, and the justification for continuing the project beyond this point is as follows: during the development of the simulation environment there were several programming mistakes which compounded to inflate the apparent performance of the EDT from the nN range into the μN and mN range. These programming mistakes were not identified until late in the simulation development process, and so it was decided to continue the project to completion, which provides a definitive and thorough assessment of EDT feasibility.

4.2.1. High Level Simulation Validation
As previously mentioned, complete validation in a novel field such as EDT propulsion is quite difficult, but a high-level validation effort can be performed. This involves choosing one or more studies which assess missions or simulations using EDTs, and attempting to replicate the results. Generally the data used for these simulations is not readily available, so many assumptions are made, and so the validation can be considered successful if the difference between reference and simulation values are within an order of magnitude.

Like in the verification, the input parameters to the simulation are specified in Table 4.6 [54]; it should be noted that unlike in the verification cases, the dimensionless current is specified, instead of the true current, but the calculation method is almost identical. It should be noted that the values for **V** and **B** used here differ significantly from Table 4.4, although the fundamentals of the problem remain the same, so this is not a problem; additionally both verification / validation methods are stand-alone.

Table 4.6: Base parameters used in the current model validation [54].

	V	**B**	**l**	σ	A	i_c	L
Units	m/s	nT	-	S/m	m^2	A	m
Values	$\begin{pmatrix} 0 \\ 7350 \\ 0 \end{pmatrix}$	$\begin{pmatrix} 0 \\ 0 \\ -17500 \end{pmatrix}$	$\begin{pmatrix} -1 \\ 0 \\ 0 \end{pmatrix}$	3.4014×10^7	1.9635×10^{-7}	0.015	500

The output of the simulation and reference data can be seen in Table 4.7, in which the simulated induced voltage E_m is within the range of values produced by the reference data [54], and so can be considered validated.

Table 4.7: Validation of current and thrust modelling, using reference data [54], compared against simulation data.

	E_m
Units	V
Simulation	-89
Reference	-60 to -90

Regarding the remaining parameters used to calculate tether current, these values are not readily provided in any literature, and so cannot be properly validated, although for the purposes of this study, the previously conducted verification is considered sufficient.

4.3. SRP Verification

The verification process for SRP perturbations is quite a simple one. Since the cannonball model of SRP is already modelled and validated within Tudat, only the implementation of it for this project needs to be verified.

In order to do this, the SRP acceleration magnitude that is outputted from the simulation environment is compared against a number of reference calculations completed by hand, using the equations outlined in Section 2.7. For these calculations the same tether properties are used and are outlined in Table 4.8, with the citations referring to where the value was obtained; it should be noted that k_{rad}, A_{SRP} and m_{tot} are chosen arbitrarily.

Table 4.8: Summary of parameters used in SRP verification.

Parameter	Symbol	Unit	Value
Radiation Coefficient	k_{rad}	-	0.5
Vehicle SRP Area	A_{SRP}	m^2	2.4
Vehicle Mass	m_{tot}	kg	100
Reference radiation intensity [13]	W_0	W/m^2	1367
Reference radiation distance [24]	r_0	AU	1
Speed of light	c [13]	m/s	2.998 ×10^8

The comparison between outputted Tudat simulation data and the reference calculations can be seen in Figure 4.7. In the figure, the two models are close enough that only the reference calculations can be recognised; the largest variation between the two was on the order of magnitude 10^{-17} m/s^2, thus verifying the simulated SRP model.
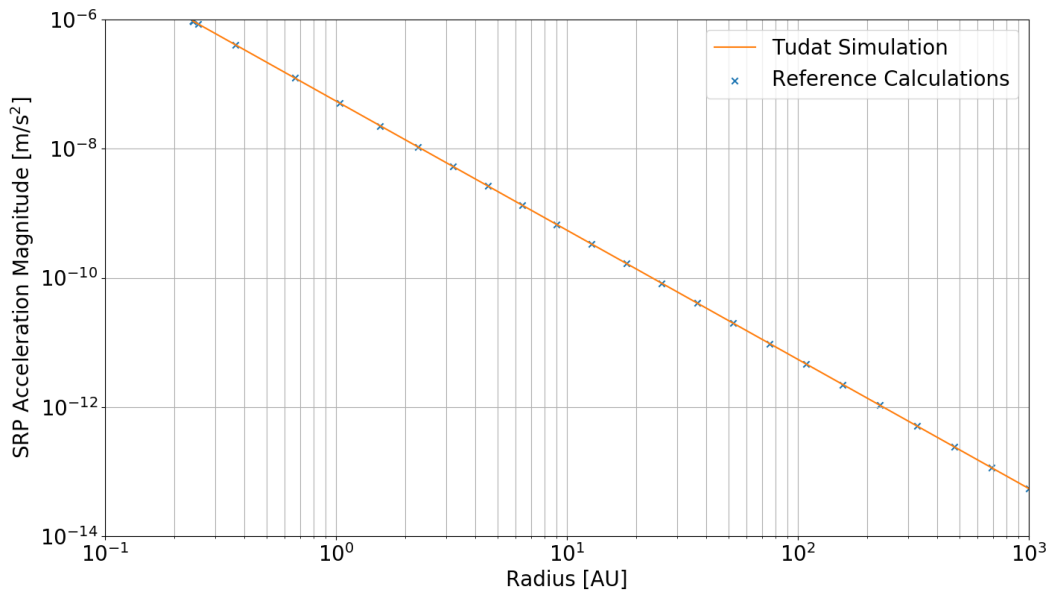
Figure 4.7: Comparison of SRP acceleration magnitude from Tudat simulation, and reference calculations (i.e. those done by hand).

An additional simple stage of verification involved individually setting the SRP area and solar radiation coefficient values to zero, which showed the outputted acceleration to then become zero m/s^2, as expected.

4.4. Gravity Assist Verification and Validation

In order to verify the simulations run in the first stage optimisation of Section 3.2, the simulation is used on a simpler case, for which there are known results with the same optimiser.

The case used for verification is the Earth-Mars trajectory calculated by Tudat developers, with constraints as shown in Table 4.9 [44]. It should be noted that in this case a DV constraint is not imposed, unlike the simulations run in Section 3.2; this is to comply with the setup of the verification case. In addition to this, the arrival DV at Mars is also included, into a circular 200 km orbit. However all other aspects are equal: the MOEAD optimisation algorithm is used with the same settings, and the results obtained are for the 10th generation of optimisation.

Table 4.9: Constraints used for the Earth-Mars trajectory optimisation.

Bound Type	Value	Units
Launch date range	2020 - 2025	-
Time of flight constraints	200 - 1000	days

The results of the optimisation arrived at by the verification case are shown in Figure 4.8, which comprises a porkchop plot, with the optimised data points overlated as a scatter plot, along with a separate scatter plot of DV against TOF. To compare against this is a porkchop plot with relevant optimised points overlayed as a scatter plot, shown in Figure 4.9, which is arrived at using the same methods as in Section 3.2.
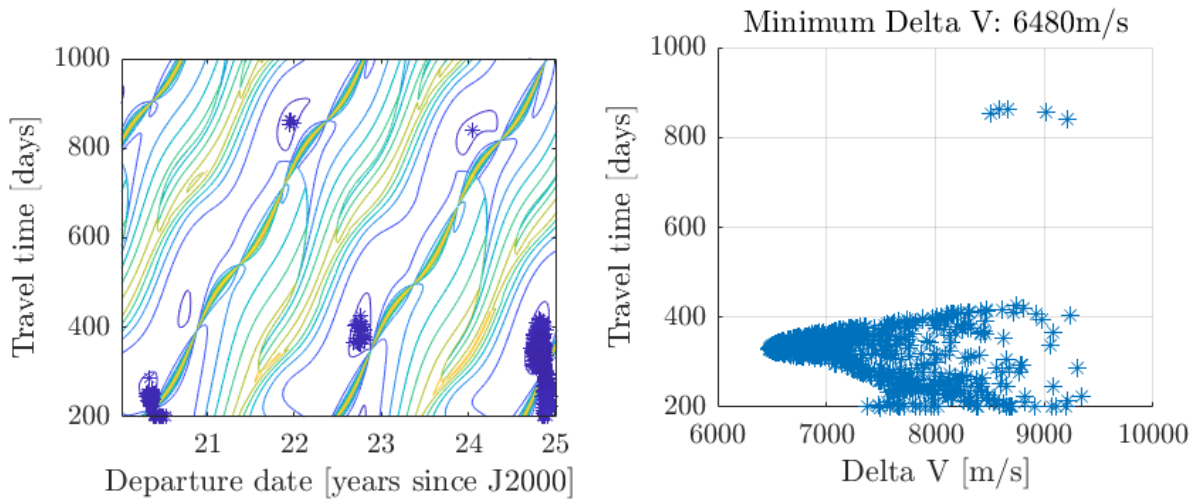
Figure 4.8: Optimisation plots achieved by Tudat developers, for the Earth-Mars trajectory optimisation over the period 2020-2025. These represent the 10th generation of optimisations. The plots are the porkchop plot with optimised solutions shown by blue crosses (left), and a scatter plot of DV against travel time for all optimised solutions (right) [44].
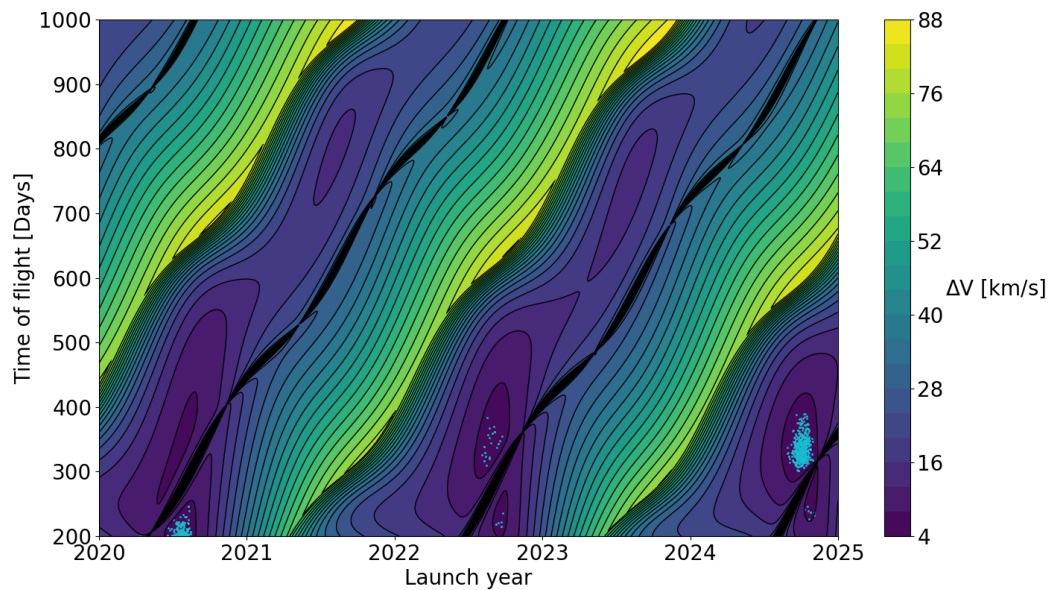
Figure 4.9: Recreation of the porkchop plot in Figure 4.8, for an Earth-Mars transfer trajectory, with 10th generation optima overlayed as a scatter plot.

By comparing Figures 4.8 and 4.9, it can be clearly seen that the results are almost identical, with similar regions of optima found; those being mid 2020 with a TOF of around 200 days, mid 2022 with a TOF around 400 days, and the end of 2024 with a TOF ranging from around 300 to 450 days.

It should be noted that there a few other minima points represented in Figure 4.8 that are not

shown in Figure 4.9, however there are only one or two points for each of these regions in the verification case, and so due to some slight variation in the simulation implementation and the inherent slight randomness of the optimisation scheme, it can be expected that these regions could be missed.

The DV - TOF plot from Figure 4.8 (right) can also be recreated as shown in Figure 4.10. The figure shows a clear similarity in the character of the obtained optima, although the minimum DV of the simulated data (around 5.8 km/s) is considerably lower than that of the reference case (around 6.5 km/s). Since optima are only generated to the 10th generation, and there are slight differences in implementation between the reference case and the simulated case, this difference can be attributed to the relative difference in convergence between the two cases.
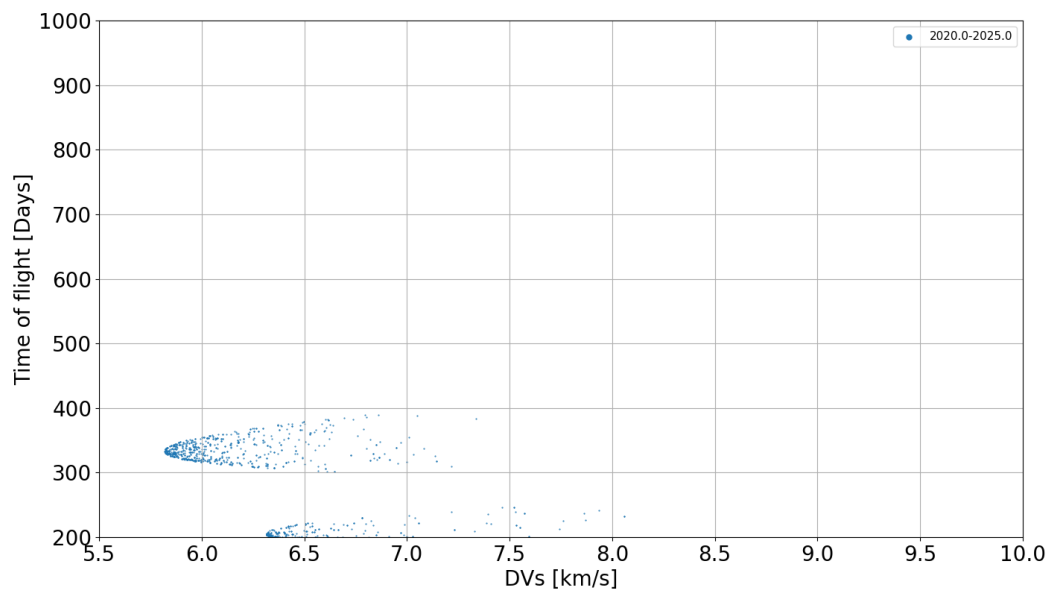
Figure 4.10: Recreation of the DV - TOF plot in Figure 4.8, for an Earth-Mars transfer trajectory.

With the above considerations in mind, it can confidently be concluded that the first stage optimisation is verified.

4.5. Integrator Verification

In order to verify the quality of the simulation, the integrator used and its settings must be assessed. In order to do this two trajectory types were chosen: a gravity assist-based trajectory and an inner Solar System trajectory; these trajectories were then run using the same nominal integrator (RK-87 Dormand-Prince), with a nominal trajectory using the usual tolerance values, along with a highly precise reference trajectory, with much tighter tolerances to compare against.

Firstly for the gravity assist case, the initial conditions are taken arbitrarily from the selection of solutions found by the gravity-assist generator discussed in Section 3.2. The reference simulation uses a tolerance value of 10^{-12} for both absolute and relative tolerance, while the nominal case uses values of 10^{-5}. Figure 4.11 shows the difference between the nominal

and reference trajectories over time, while Figures 4.13 and 4.12 represent the trajectories themselves. It should be noted that Figure 4.11 shows something of a pattern, with some points having higher discrepancies than others, which is most likely to be caused by interpolation to common epochs between the nominal and reference trajectories.
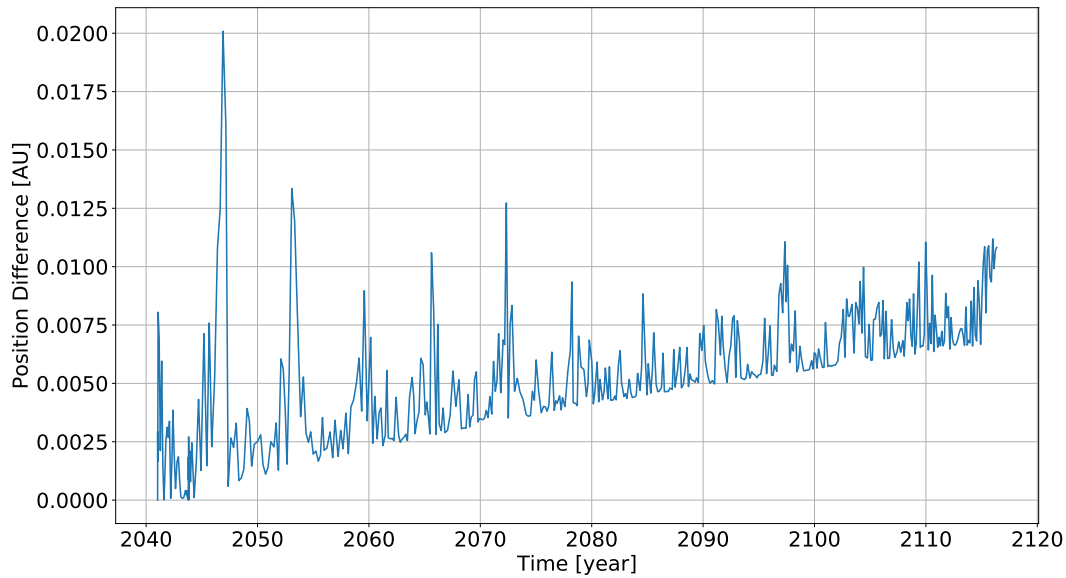
Figure 4.11: Gravity-assist based integration verification, showing differences between nominal and reference trajectories.
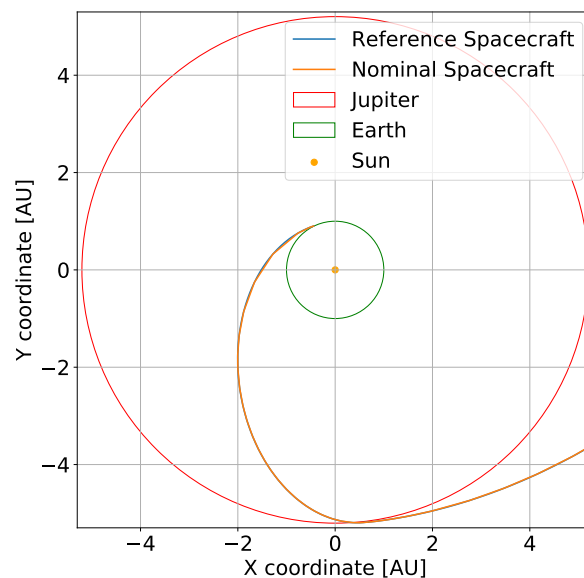
Figure 4.12: Gravity-assist based integration verification, showing enlarged section of early trajectory.
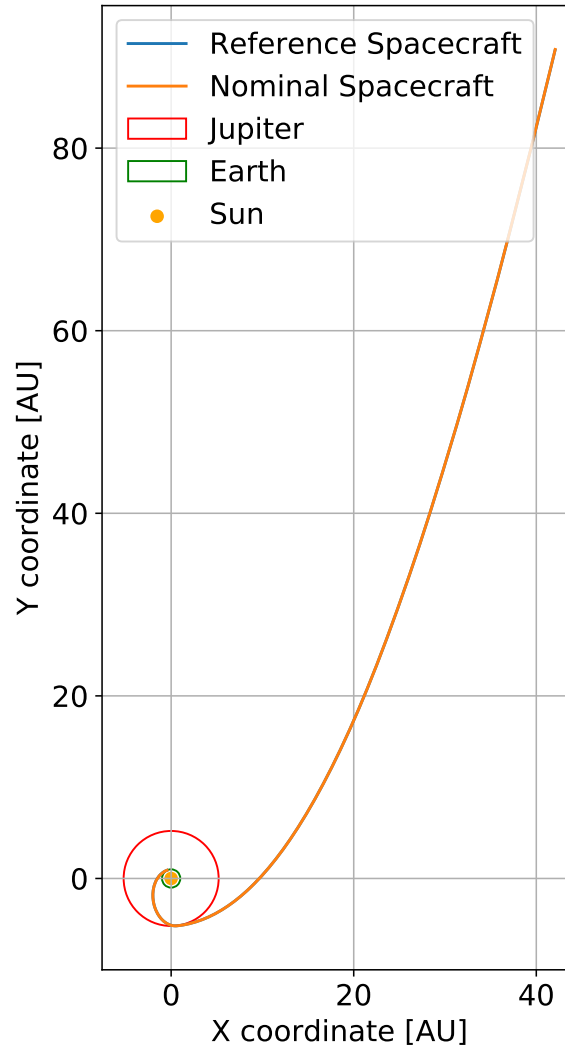
Figure 4.13: Gravity-assist based integration verification, showing full trajectory.

For the inner Solar System case, similarly to the gravity-assist case, the reference simulation uses a tolerance value of 10^{-12} for both absolute and relative tolerance, while the nominal case uses a value of 10^{-5}. The orbit chosen is an elliptical one with aphelion 100 AU, perihelion 0.1 AU, 0° inclination, and an initial true anomaly of -90°. Figure 4.14 shows the difference between the nominal and reference trajectories over time, while Figures 4.15 and 4.16 represent the trajectories themselves.
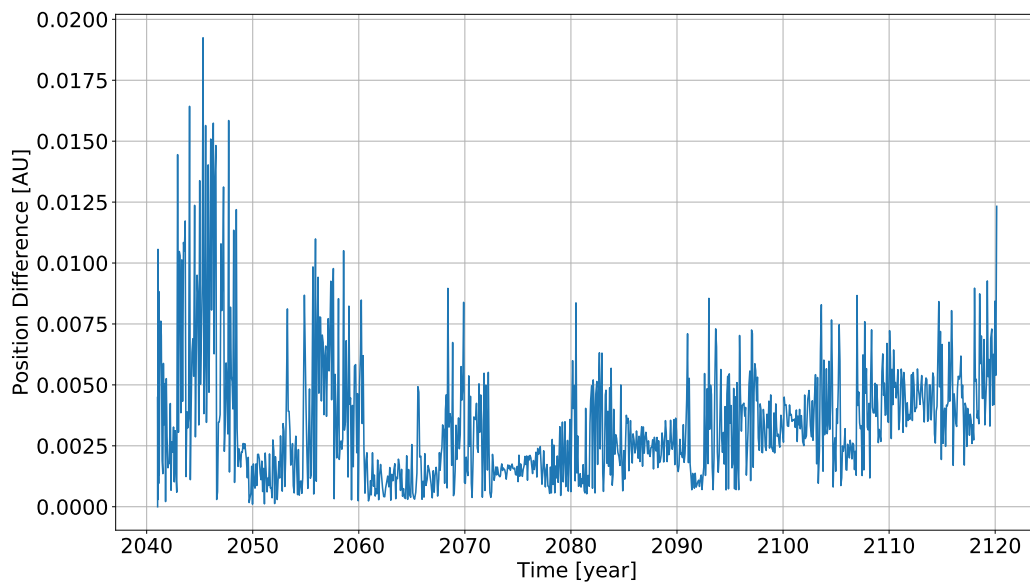
Figure 4.14: Simple inner Solar System based integration verification, showing differences between nominal and reference trajectories.
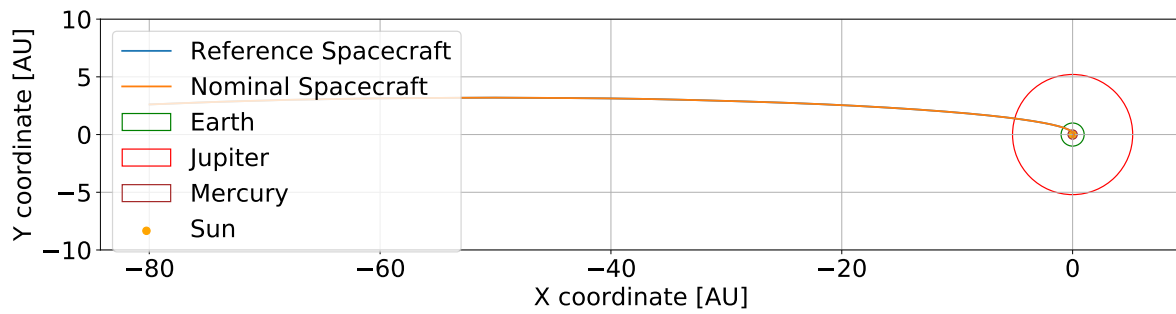
Figure 4.15: Simple inner Solar System based integration verification, showing full trajectory.
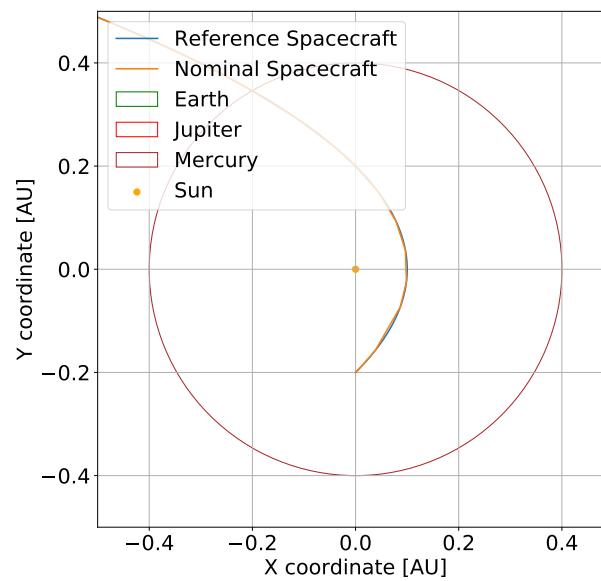
Figure 4.16: Simple inner Solar System based integration verification, showing enlarged section of early trajectory.

From the above plots and information, it can be seen that the maximum deviation between the integrators is no more than 0.02 AU, with no clear pattern to the magnitude of those differences over time, indicating that they likely arise from small calculation errors and do not significantly compound over time. For the purposes of this study, such displacements are acceptable due to the interplanetary scales involved, and therefore the integrator settings can be considered verified.

It should also be noted that the integrator itself does not require further verification or validation, since it is already built into the Tudat package, and so has been extensively validated.

5

EDT Configuration and Gravity-Assist Exploration

In this chapter some preliminary results are assessed, which support but do not directly answer the research questions. Namely the results of the EDT configuration parameter exploration, as well as the results of the gravity-assist trajectory identification procedure.

5.1. EDT Configuration Parameter Exploration Results

This section shows the results of the simulations outlined in Section 3.1; the following subsections show a series of plots and discussions for each parameter, with a subsequent summary of the information gained and a description of the spacecraft taken forward for the trajectory analyses.

In each plot the bare-tether and transient-tether EDT configurations are shown; also shown (where the plot scales allow) is the nominal EDT configuration that is decided upon at the end of this section.

5.1.1. Tether Length

Figure 5.1a shows that, as expected, longer tethers tend to produce larger thrust values; the relationship is linear and is the same regardless of using either the transient or bare-thether current generation solutions.

Figure 5.1b shows that with increasing tether length, the spacecraft acceleration also tends to increase; the relationship however is not linear, with diminishing returns as the tether length increases to higher values. It should also be noted that unlike the thrust, which varies by orders of magnitude, the acceleration improvement is small relative to the overall acceleration; this is to be expected since as the tether length increases so too does the spacecraft mass, which is dominated by the tether mass.

(a) Thrust with varying tether length.
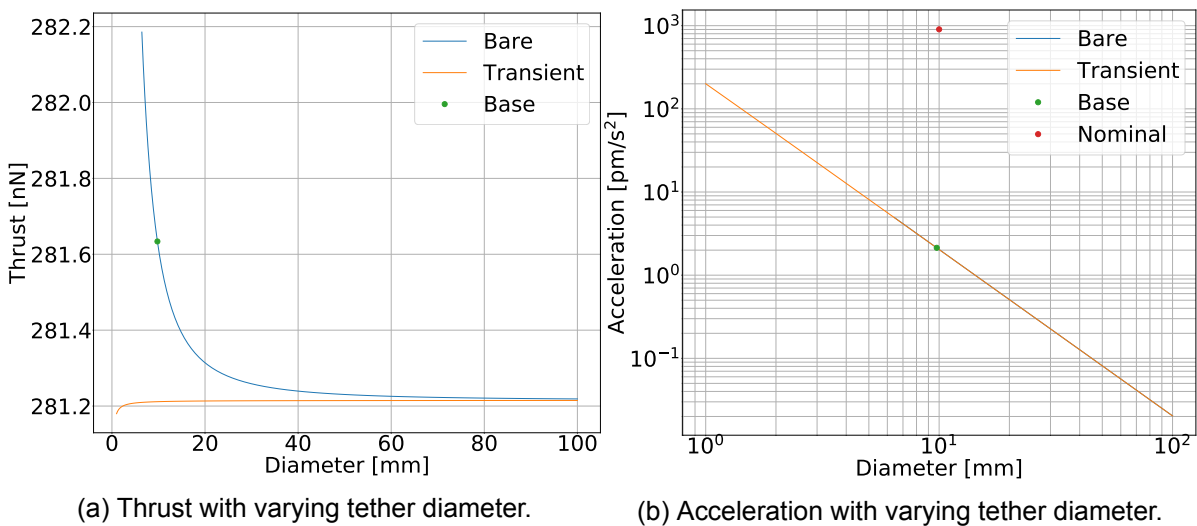
(b) Acceleration with varying tether length.
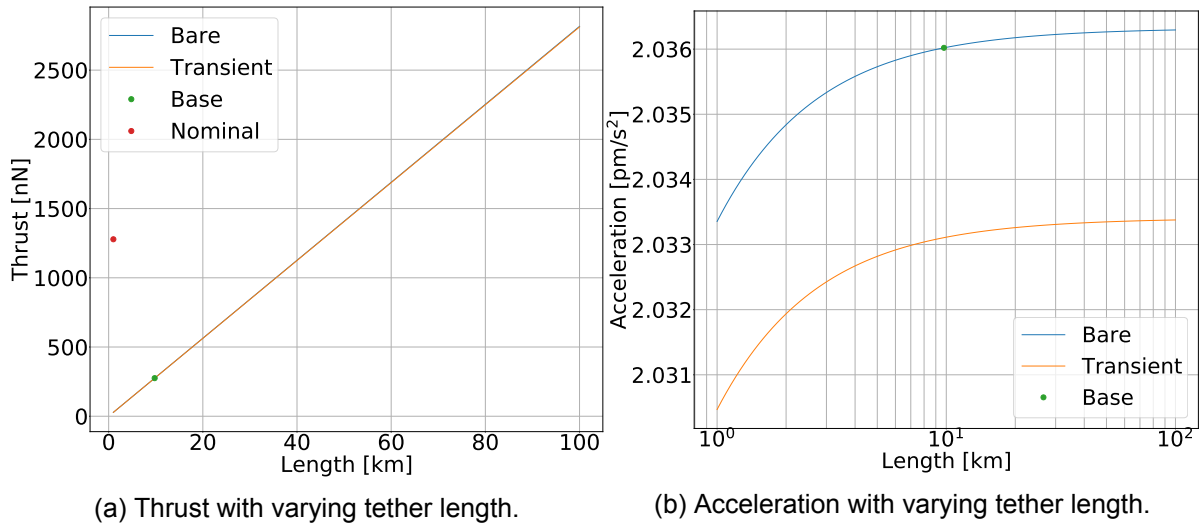
Figure 5.1: EDT spacecraft performance with varying tether length. Bare-tether and transient thrust generation concepts are shown in blue and orange respectively, with the base nominal case represented by a green point.

5.1.2. Tether Diameter

Figure 5.2a shows that in the transient case, at very small values of tether diameter (around 1-3 mm) there is a very small increase in thrust generation capacity, before the generated thrust plateaus out at the values obtained for larger tether diameters. This behaviour is not expected, since for the transient case only changes in tether length, magnetic field strength, or generated current should correspond to a change in generated thrust.

The bare-tether case shows that the generated thrust increases exponentially for small diameter values, before plateauing out to around the same thrust as the transient case. This behaviour is unexpected as a larger tether diameter equates to a larger conducting area and therefore one might expect an increased thrust; the behaviour may be explained by the fact the small-diameter tethers begin to approach violation of the small dimensionless current assumption, since it is already known that diameters of 2 mm or smaller do indeed violate this, as described in Subsection 3.1.3.

Despite these unexpected results for the thrust behaviour with tether diameter, it can be seen that the magnitude of the effect is very small, only being on the order of 1 nN. Therefore the effect of this behaviour can simply be neglected.

(a) Thrust with varying tether diameter.
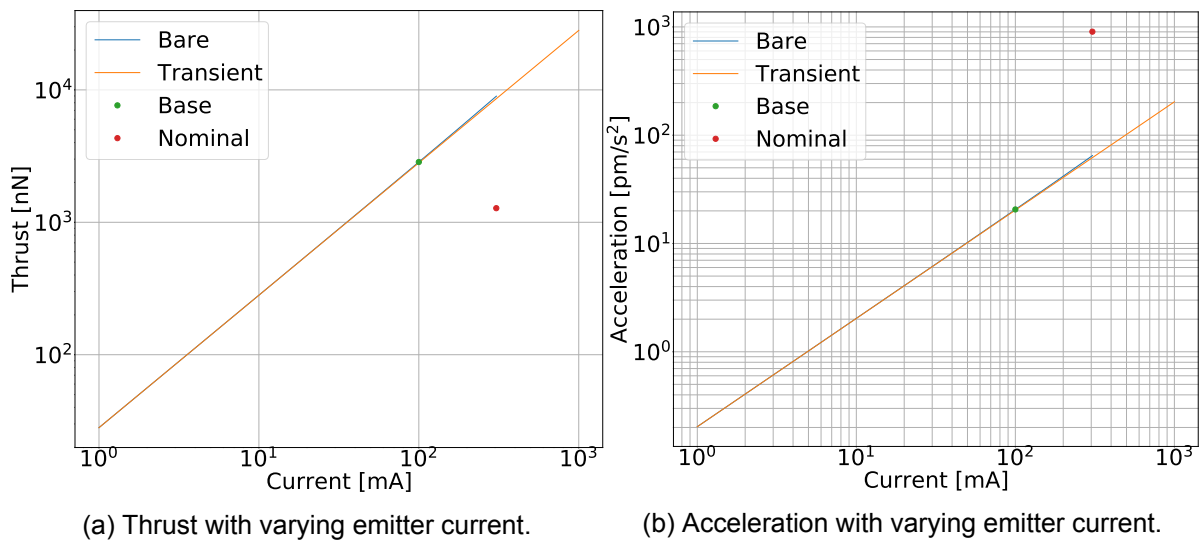
(b) Acceleration with varying tether diameter.

Figure 5.2: EDT spacecraft performance with varying tether diameter. Bare-tether and transient thrust generation concepts are shown in blue and orange respectively, with the base nominal case represented by a green point.

Unlike for the thrust generation, it can be seen in Figure 5.2b that as the tether diameter increases, the spacecraft acceleration exponentially decreases. This is to be expected, since increasing tether diameter inevitably increases the total tether volume, and therefore the overall mass of the spacecraft, without significantly affecting the thrust generation.

5.1.3. Generated Tether Current

Figure 5.3a shows that as expected, the larger the emitter current the larger the provided thrust; the relationship is exponential (since the scale of the plot is logarithmic), and is the same for both bare-tether and transient current generation methods. One thing to note however is that the bare-tether line stops slightly before the transient-current line (at around 120 mA), this is because the cases with currents higher than this were invalid due to breaking assumptions of the simulation environment.

Also as expected, Figure 5.3b shows that the spacecraft acceleration also increases with increasing emitter current, with the same exponential relationship as for the thrust. Again the bare-tether line ends above around 120 mA, as these configurations are not valid. It should be noted that the effect of increased emitter current on the spacecraft (end) mass is not modelled as one might expect; this is to reduce complexity, and because the overall spacecraft mass is generally dominated by the tether itself.

(a) Thrust with varying emitter current.   (b) Acceleration with varying emitter current.

Figure 5.3: EDT spacecraft performance with varying tether emitter current. Bare-tether and transient thrust generation concepts are shown in blue and orange respectively, with the base nominal case represented by a green point.

5.1.4. Tether Area Ratio

Figure 5.4a shows a departure in behaviour between bare and transient current generation solutions. The transient current case shows no relationship between area ratio and generated thrust: this is to be expected since for this case the current is modelled as a single value irrespective of the tether composition. The bare-tether solution on the other hand shows increasing thrust with increasing area ratio, or in other words the more aluminium content compared to copper, the larger the thrust; the relationship is non-linear and somewhat unexpected, as one would expect the increased conductivity of copper to positively impact the thrust generation capability of the EDT. It should be noted however that the increase in thrust with varying area ratio is very small, overall changing by less than 1 nN.

Unlike the thrust, Figure 5.4b shows that there is a significant increase in acceleration with increasing area ratio, with the behaviour the same for both the bare-tether and transient current solutions. The relationship is exponential, and the relationship is to be expected since aluminium has a significantly lower density than copper, causing and overall reduction in spacecraft mass and therefore an increase in acceleration.

(a) Thrust with varying tether area ratio.
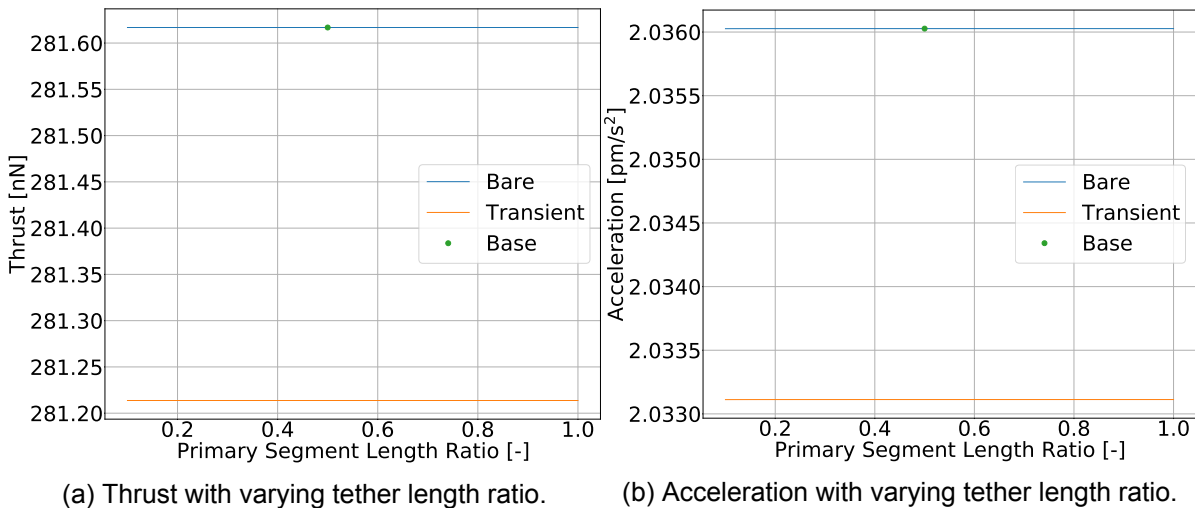
(b) Acceleration with varying tether area ratio.
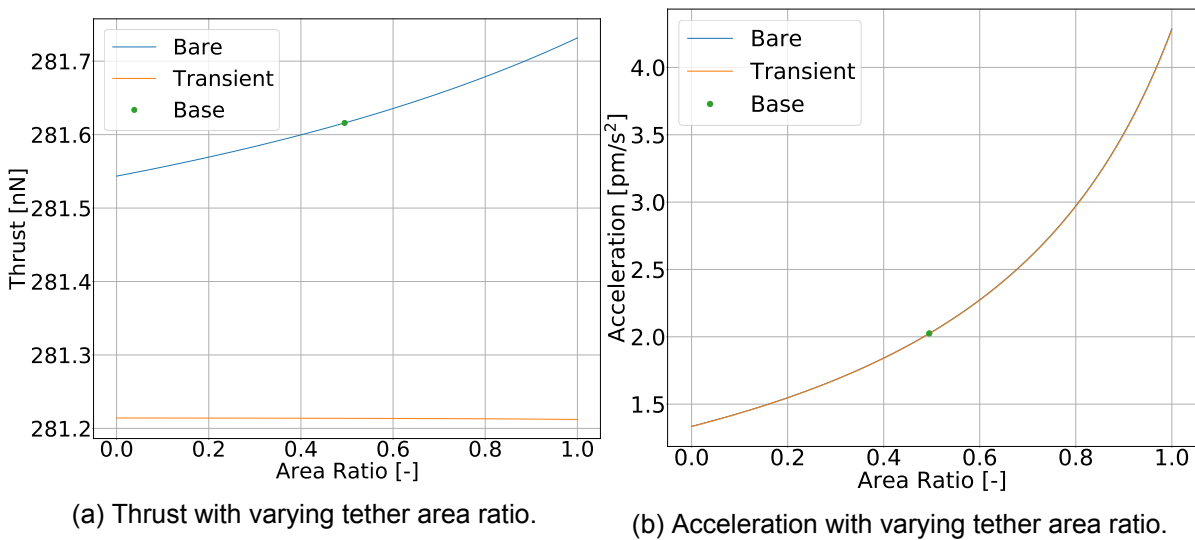
Figure 5.4: EDT spacecraft performance with varying tether area ratio. Bare-tether and transient thrust generation concepts are shown in blue and orange respectively, with the base nominal case represented by a green point.

5.1.5. Number of Primary Lines

Figure 5.5a shows that for the transient case, the number of primary lines has no relationship with the thrust generation, as would be expected. However, for the bare tether case, thrust generation decreases exponentially with an increasing number of primary lines. This is somewhat unexpected, for the same reasons outlined in Subsection 5.1.2, however since the difference in thrust generation is very small, it can simply be neglected in the same way.

Unlike for the thrust generation, Figure 5.5b, it can be seen that as the number of lines increases, the spacecraft acceleration exponentially decreases. This is to be expected, since increasing number of lines inevitably increases the total tether volume, and therefore the overall mass of the spacecraft, without significantly affecting the thrust generation.

(a) Thrust with varying number of primary lines.

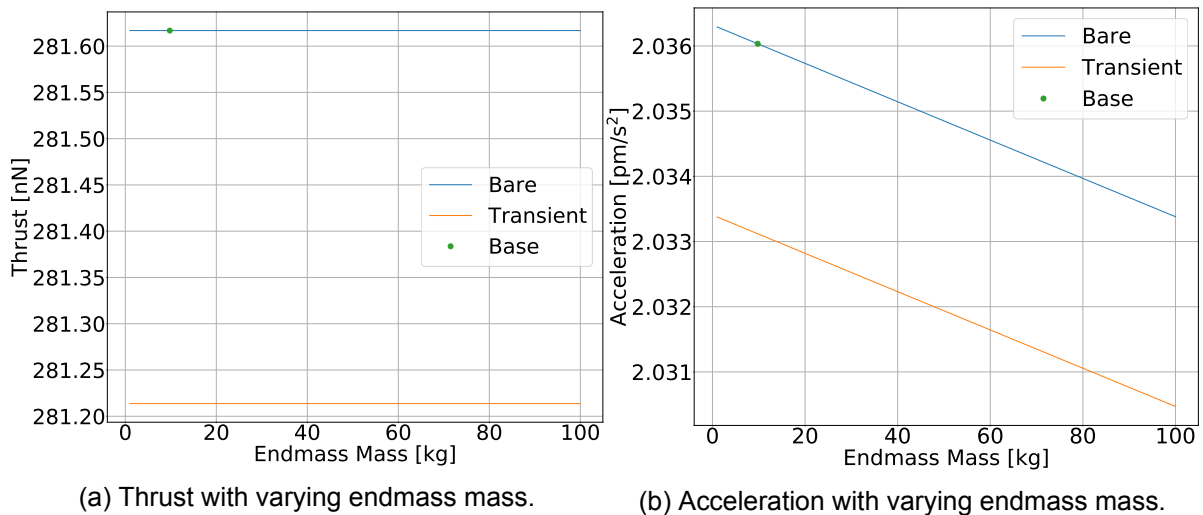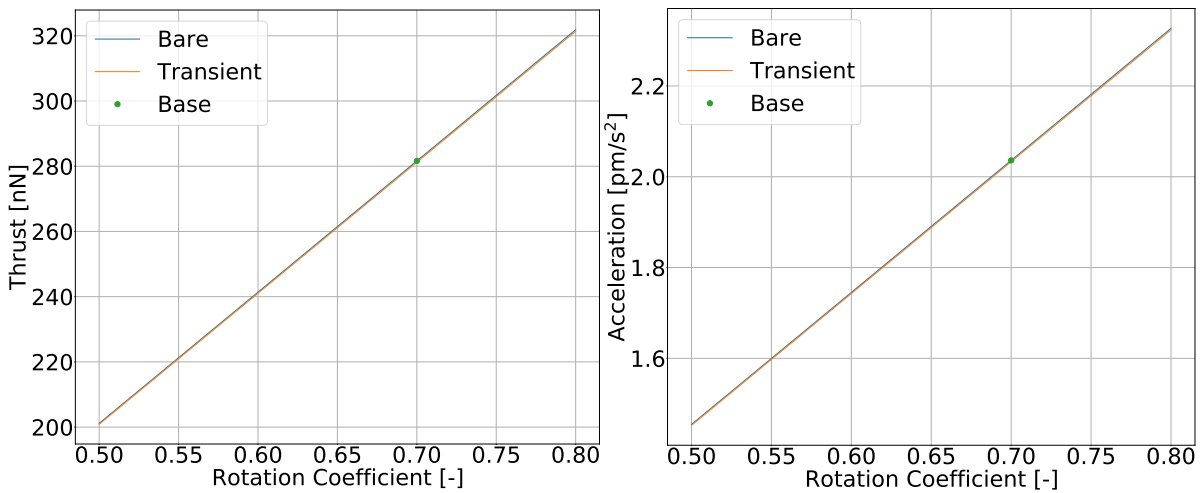(b) Acceleration with varying number of primary lines.
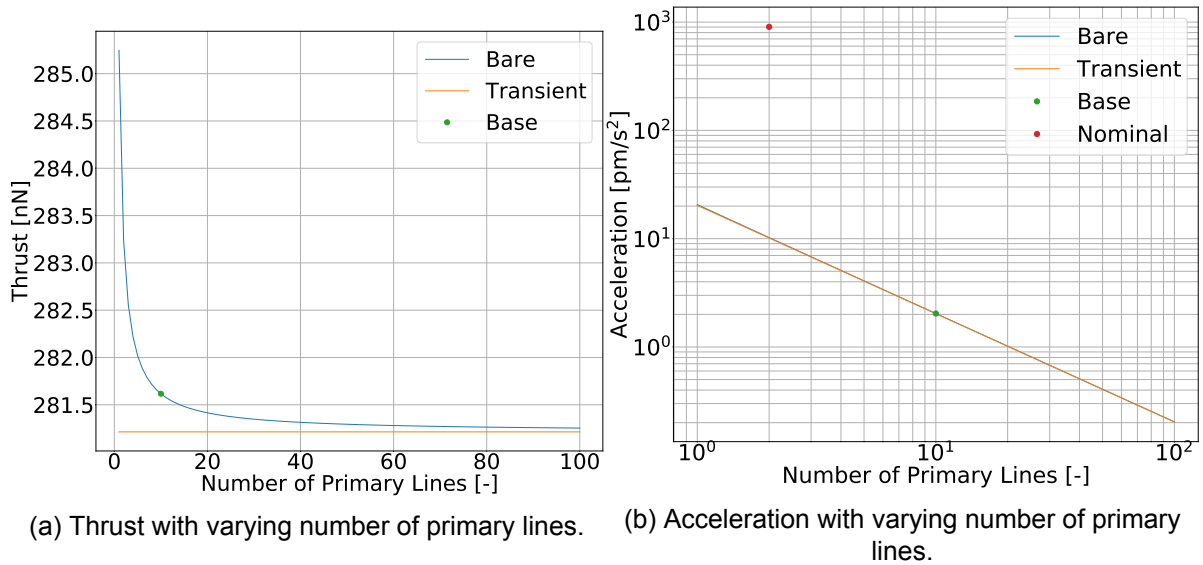
Figure 5.5: EDT spacecraft performance with varying number of primary lines. Bare-tether and transient thrust generation concepts are shown in blue and orange respectively, with the base nominal case represented by a green point.

5.1.6. Length Ratio

Figure 5.4a shows that for both bare-tether and transient current generation solutions, there is no relationship between thrust and primary segment length ratio. This is to be expected, since the ratio does not actually affect the primary lines themselves, but rather the secondary lines, and so any performance difference would manifest as a mass reduction only.

Like for the thrust, Figure 5.6b also shows no relationship between primary segment length ratio and spacecraft acceleration. Again this is expected, since changing the ratio will only affect the number of links secondary links between primary tether lines, without significantly changing the total length of secondary lines, and therefore the mass is also unaffected.

(a) Thrust with varying tether length ratio.　　(b) Acceleration with varying tether length ratio.

Figure 5.6: EDT spacecraft performance with varying tether length ratio. Bare-tether and transient thrust generation concepts are shown in blue and orange respectively, with the base nominal case represented by a green point.

5.1.7. Endmass

Figure 5.7a shows that for both the bare-tether and transient cases there is no relationship between endmass and thrust. This is to be expected since the endmass has no effect on the tether itself, which is what is used to generate thrust.

Figure 5.7b shows that, with increasing endmass, the spacecraft acceleration decreases, with a linear relationship. This is to be expected, although it should be noted that the impact to acceleration is miniscule, since the spacecraft mass is generally dominated by the tether mass, rather than the endmass.

(a) Thrust with varying endmass mass.

(b) Acceleration with varying endmass mass.

Figure 5.7: EDT spacecraft performance with varying endmass mass. Bare-tether and transient thrust generation concepts are shown in blue and orange respectively, with the base nominal case represented by a green point.

5.1.8. Rotation Coefficient

Figure 5.8a shows that for both bare-tether and transient cases with increasing rotation coefficient, the generated thrust also increases, and the relationship is linear. This is to be expected since the rotation coefficient is a simple factor applied directly to the generated thrust in the simulation environment.

Similarly to the thrust, Figure 5.8b also shows that for both bare-tether and transient cases, the spacecraft acceleration has a positive linear relationship with the rotation coefficient, as expected.

(a) Thrust with varying rotation coefficient.   (b) Acceleration with varying rotation coefficient.

Figure 5.8: EDT spacecraft performance with varying rotation coefficient. Bare-tether and transient thrust generation concepts are shown in blue and orange respectively, with the base nominal case represented by a green point.

5.1.9. Configurations Parameter Exploration Summary

To summarise the results of this section, Table 5.1 provides a qualitative summary of each parameter and its effect on EDT thrust and acceleration (i.e. performance). It should be noted that this only refers to the bare-tether current generation concept; this is because this is the more realistic approach, and also since the only parameters in which their behaviour is different are those parameters with a negligible affect on performance. In the table, the performance is described as "Strong", "Weak", or "Negligible", which are highlighted using green and red graduated row colouring; it should be noted that the colouring applies to the acceleration column, and not thrust, since acceleration is the main performance metric.

Table 5.1: Parameter effects on EDT performance, for bare-tether current generation case.

Parameter	Thrust		Acceleration	
	Behaviour	*Strength*	*Behaviour*	*Strength*
L	Linear increase	Strong	Logarithmic increase	Negligible
D	Exponential decrease	Negligible	Exponential decrease	Strong
I_C	Exponential increase	Strong	Exponential increase	Strong
k_A	Non-linear increase	Negligible	Exponential increase	Weak
n	Exponential decrease	Negligible	Exponential decrease	Strong
k_{l_p}	None	-	None	-
m_e	None	-	Linear decrease	Negligible
$k_{T,rot}$	Linear increase	Weak	Linear increase	Weak

The observations of Table 5.1 and previous sections allow for a nominal spacecraft to be sized according to the optimal outcome for each parameter. This new nominal spacecraft can then be taken forward for use in further analysis of the trajectories outlined in Section 3.3.

Table 5.2: Nominal spacecraft configuration to take forward in future simulations.

Parameter	Symbol	Unit	Nominal Value
Tether length	L	km	1
Tether diameter	D	mm	10
Emitter current	I_C	mA	305
Tether area ratio	k_A	-	1.0
No. primary lines	n	-	2
Primary segment length ratio	k_{l_p}	-	0.5
Endmass mass (individual)	m_e	kg	50
Rotation coefficient	$K_{T,rot}$	-	0.8

It should be noted that for several parameters in Table 5.2, the spacecraft performance is not sensitive to that parameter, and so it can be chosen essentially arbitrarily, therefore the base value is simply taken.

The found nominal spacecraft has the performance properties as shown below:

- Nominal thrust: 1.278 μN

- Nominal accel: 0.903 nm/s^2

- Nominal mass: 1414 kg

5.2. Gravity-Assist Identification Results

In this section, the results of the two-stage optimisation using a Lambert solver in the first stage, and a MOEAD optimiser in the second stage, is presented. The first-stage results are first present for each gravity-assist body, followed by the second-stage results.

5.2.1. Jupiter Assist Results - First stage

Shown in Figures 5.9 and 5.10 are the 90th generation DV - TOF Pareto fronts for the global and synodic optimisations respectively for the Earth-Jupiter transfer. The 90th generation was chosen, since at higher generations the system tended to "over optimise", significantly reducing population diversity.

It can be seen in the synodic case that there is significant variation in the the Pareto fronts for each synodic period, which is to be expected. Comparing the two plots, it can also be seen that the global front is essentially a combination of the most optimal points from all synodic periods, which is also to be expected: clearly the global optimiser is doing a good job in the global optimisation.
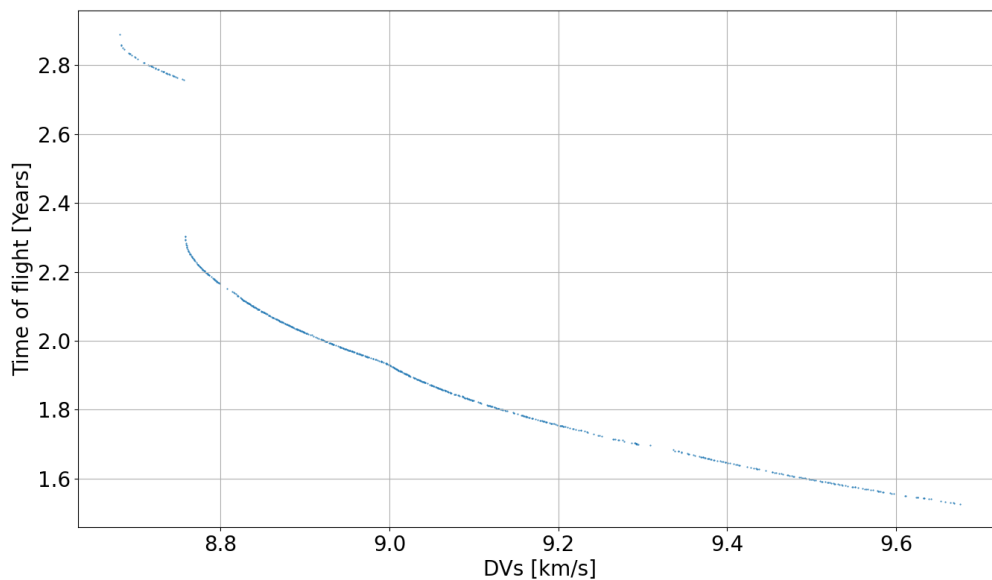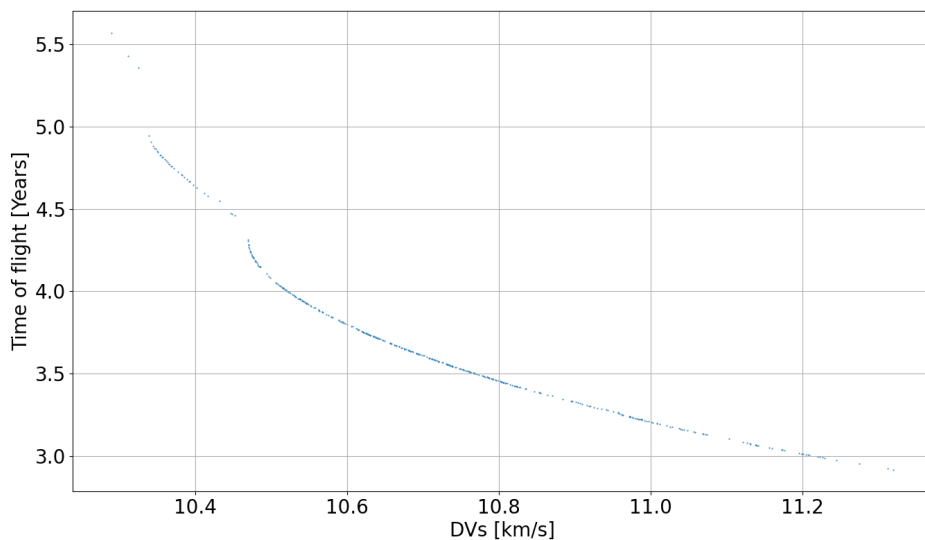

Figure 5.9: Pareto front of the global optimisation of an Earth-Jupiter gravity assist, over the period 2020-2050. This represents the 90th generation of optimisation using the MOEAD algorithm.
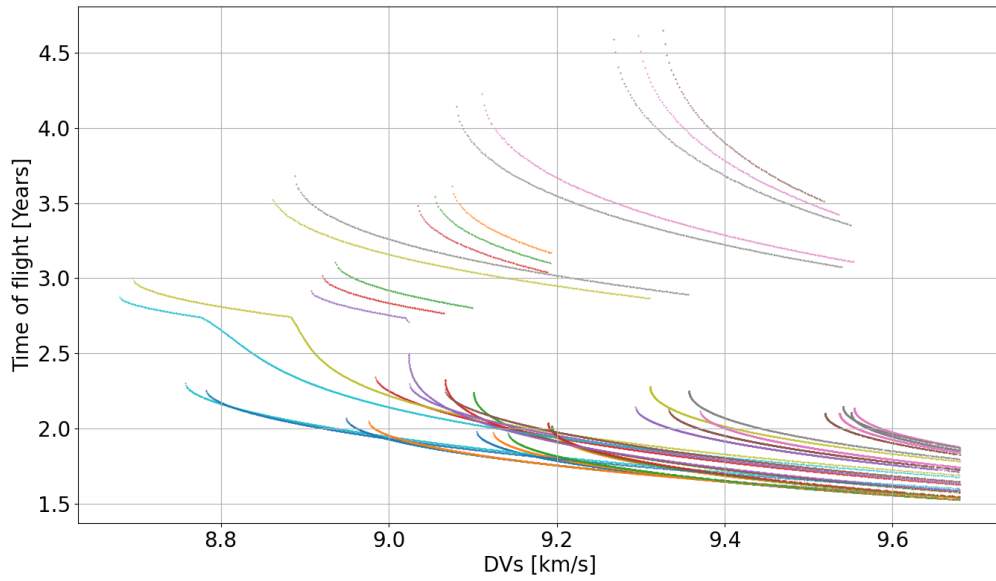
Figure 5.10: Pareto fronts for each synodic period of an Earth-Jupiter gravity assist, over the period 2020-2050. This represents the 90th generation of optimisation using the MOEAD algorithm.
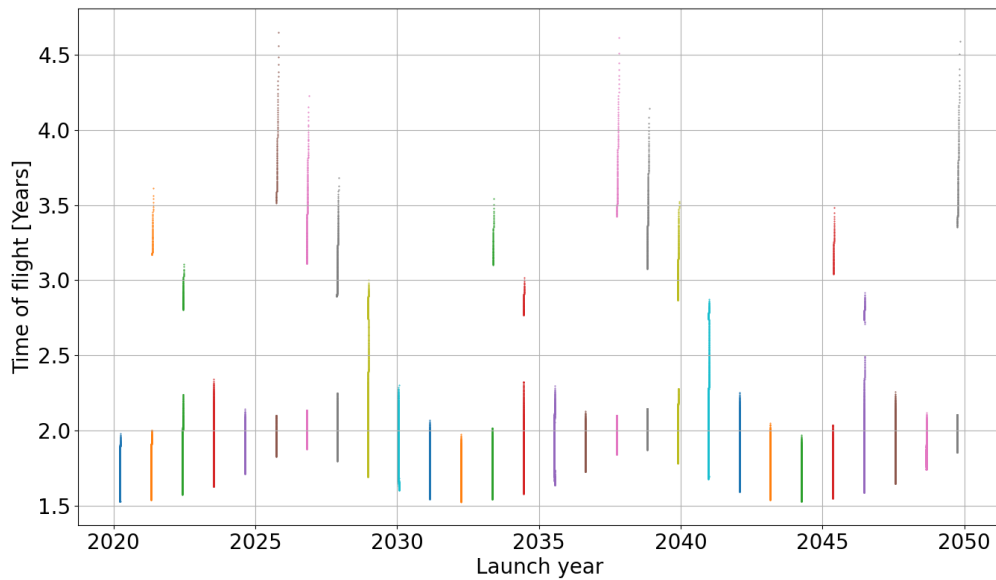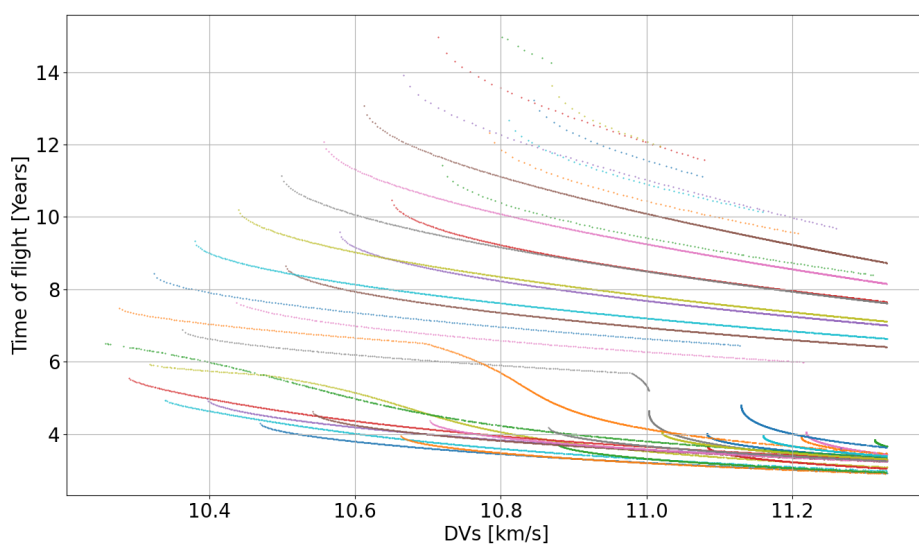

Figure 5.11: Launch year vs TOF plot for an Earth-Jupiter gravity assist, for each synodic period, over the period 2020-2050. This represents the 90th generation of optimisation using the MOEAD algorithm.

Shown in Figure 5.11 are the launch windows and times of flights for each synodic period of the Earth-Jupiter transfer, showing a clear oscillatory pattern in the minimum TOF, with period around 10 years, which is to be expected as Jupiter moves closer and further from the Sun along its orbit.

To get a better idea of how the solutions shown in Figure 5.11 relate to the associated DV, a porkchop plot can be used. Figure 5.12 overlays the trajectories from Figure 5.11, onto a porkchop plot for the same period, created using a grid-search technique. It clearly shows as expected that the solutions lie in the dark regions, where the DV is relatively low (around 8 km/s).
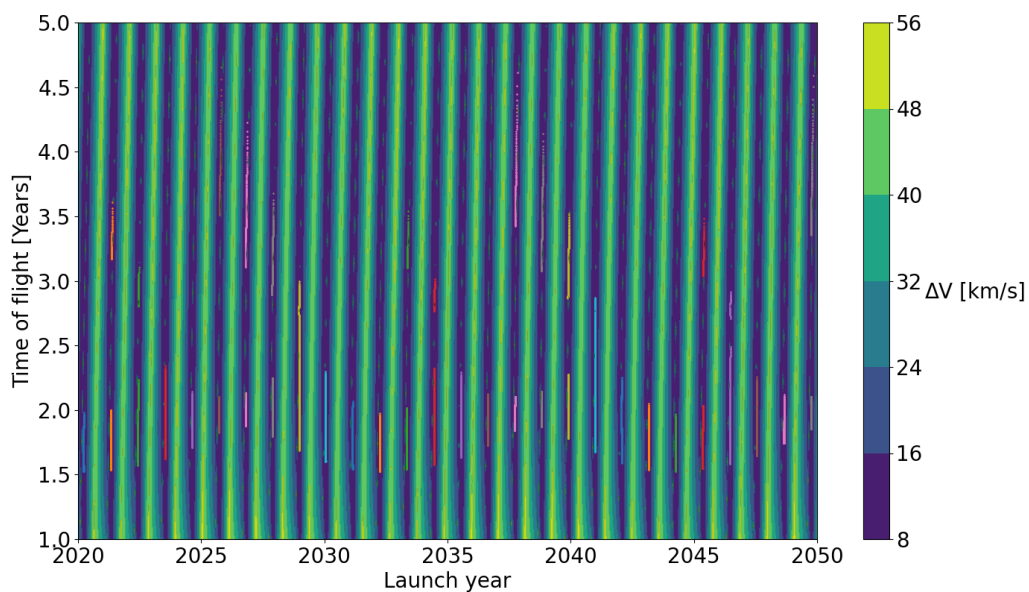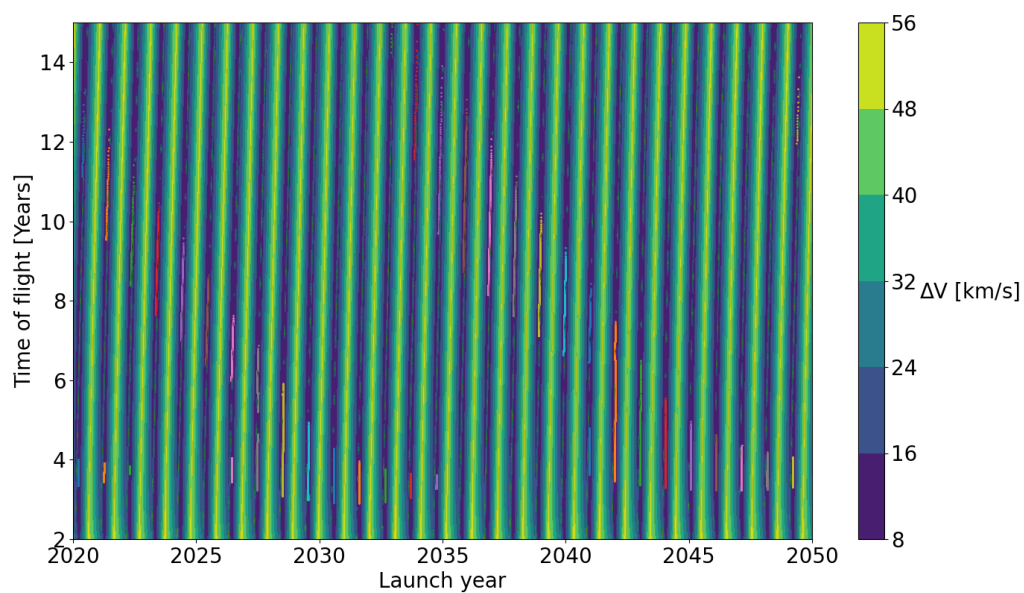

Figure 5.12: Porkchop plot of the trajectories of an Earth-Jupiter gravity assist, over the period 2020-2050, with the synodic optimisation results of Figure 5.11 superimposed, using a different colour for each synodic period.

A closer inspection of some of the global optima can be seen in Figure 5.13, shown as points in light blue, sitting around the middle of the low DV region of the porkchop plot.
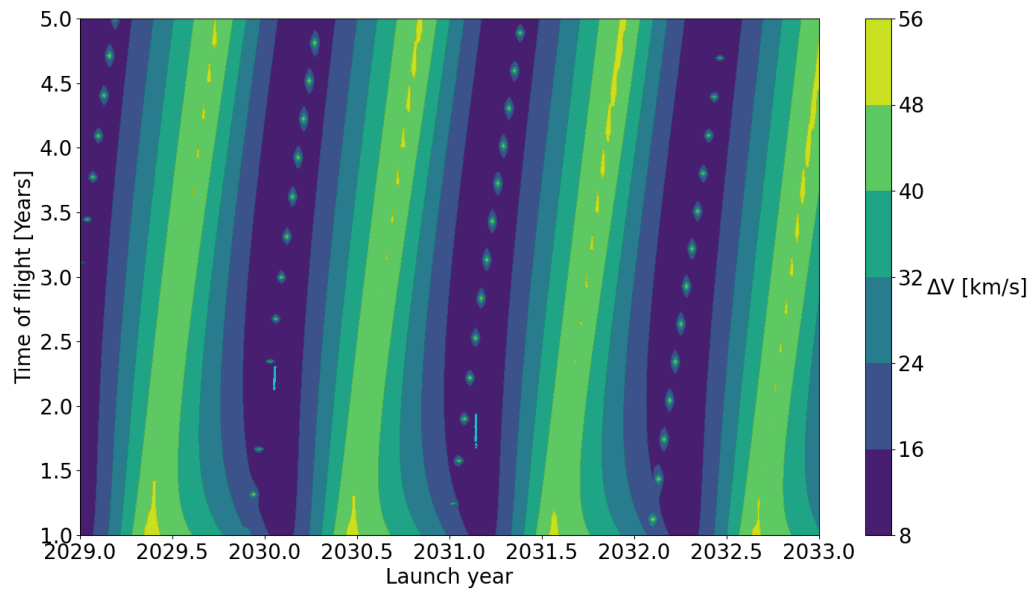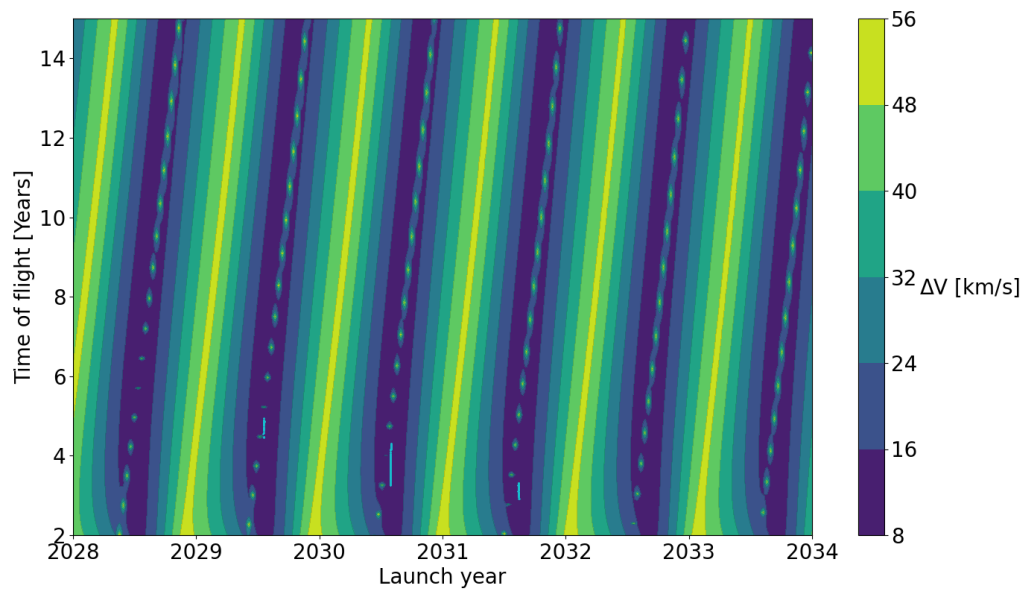

Figure 5.13: Porkchop plot of the trajectories of an Earth-Jupiter gravity assist, over the period 2029-203, with the global optimisation results for the date range superimposed as blue points.

5.2.2. Saturn Assist Results - First Stage

Similarly to the Earth-Jupiter case, the global and synodic Pareto fronts for the Earth-Saturn case can be seen in Figures 5.14 and 5.15, also shown are the launch years and times of flight in Figure 5.16. The conclusions drawn from these plots are the same as the Earth-Jupiter case, but with generally larger values for DV and TOF.

Figure 5.14: Pareto front of the global optimisation of an Earth-Saturn gravity assist, over the period 2020-2050. This represents the 90th generation of optimisation using the MOEAD algorithm.

Figure 5.15: Launch year vs TOF plot for an Earth-Saturn gravity assist, for each synodic period, over the period 2020-2050. This represents the 90th generation of optimisation using the MOEAD algorithm.
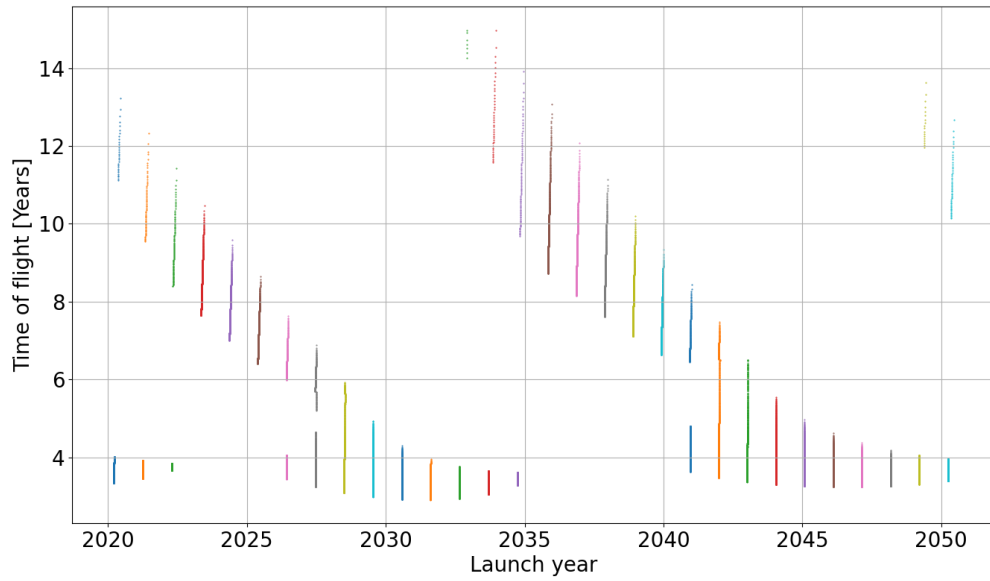
Figure 5.16: Launch year vs TOF plot for an Earth-Saturn gravity assist, for each synodic period, over the period 2020-2050. This represents the 90th generation of optimisation using the MOEAD algorithm.

Similarly to the Earth-Jupiter case porkchop plots were also produced for the Earth-Saturn case, with synodic solutions shown in Figure 5.17, and a closer inspection of the global solutions in Figure 5.18. The conclusions remain the same as previously described.

Figure 5.17: Porkchop plot of the trajectories of an Earth-Jupiter gravity assist, over the period 2020-2050, with the synodic optimisation results of Figure 5.16 superimposed, using a different colour for each synodic period.

Figure 5.18: Porkchop plot of the trajectories of an Earth-Jupiter gravity assist, over the period 2029-203, with the global optimisation results over the date range superimposed as blue points.

5.2.3. Second-Stage Gravity Assist Results

Figure 5.19 shows all Jupiter gravity-assist trajectories found by the Lambert solver, as a scatter plot against the two previously described objectives. It can be seen that there is a large amount of variation in the different possible trajectories; this is to be expected due to the variety of combinations of input variables that can result in a valid trajectory.
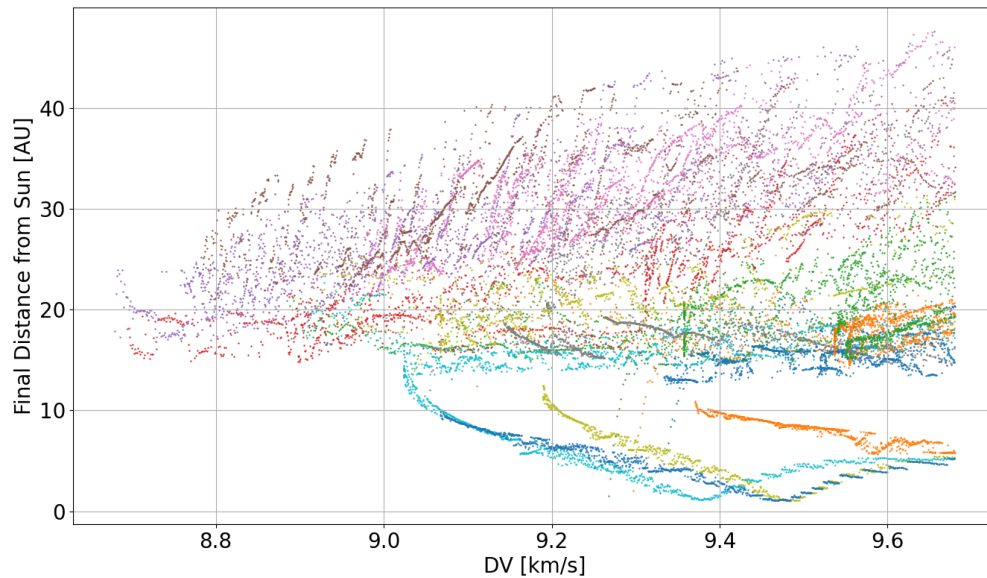
Figure 5.19: Required DV against final Solar distance for all found Jupiter gravity-assist trajectories. Each colour represents a different synodic period.

However, for the purposes of this analysis it is only necessary to single out the most efficient trajectories, for each synodic period; those being the ones with maximised Solar distance and minimised DV. This is done by making a Pareto from for each synodic period, as shown in Figure 5.20. In the figure, each possible trajectory is plotted as an individual scatter point, with a front joining these points to more clearly highlight which points belong to each synodic period; it should be noted however that the trajectory options are indeed discrete, and so a trajectory that lies along this front, but is not one of the plotted points, is not possible.

As expected, Figure 5.20 shows that certain synodic periods (and therefore launch dates) are favoured over others, which is to be expected, and is useful information which can be taken forward into the mission profiles analysis.
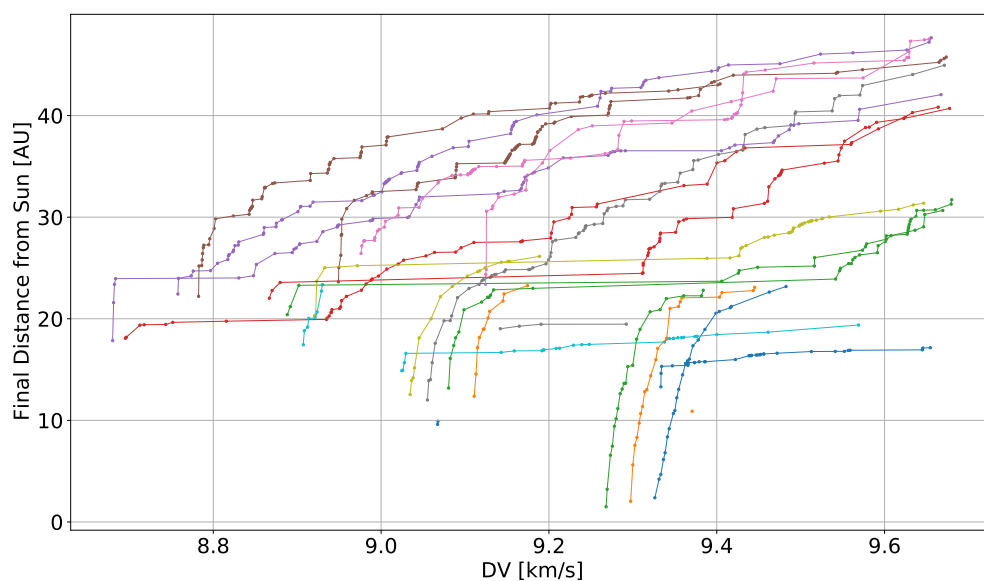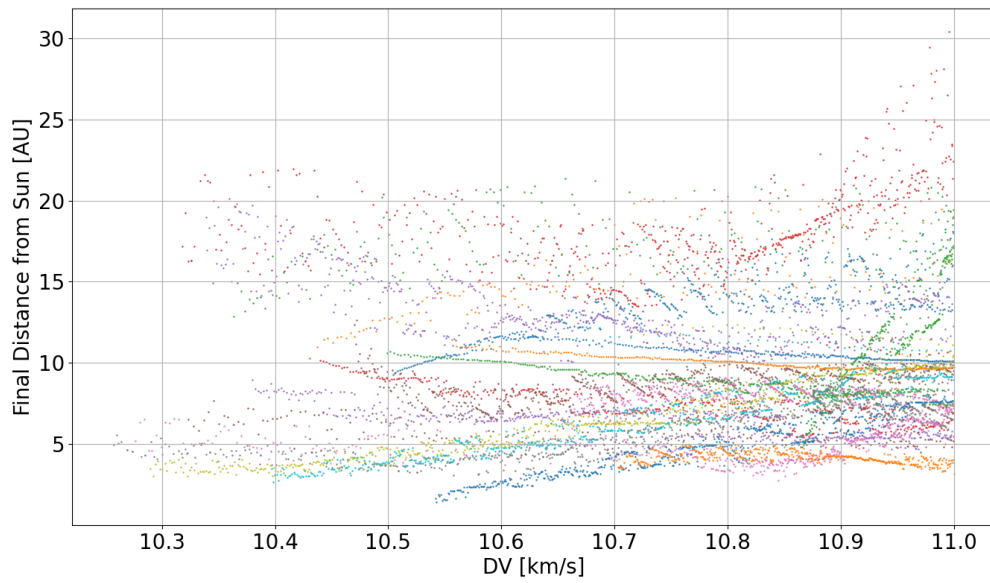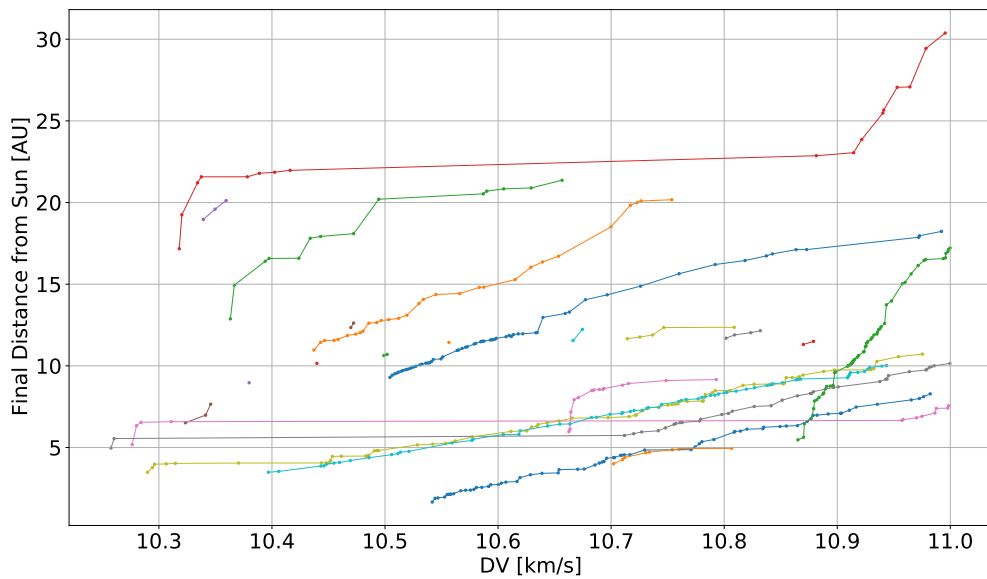
Figure 5.20: Pareto front of required DV against final Solar distance for the most efficient Jupiter gravity assist trajectories. Each colour represents a different synodic period.

Figures 5.21 and 5.22 are analogous to the Jupiter results, and the derived conclusions are broadly the same. However it should be noted that in general, gravity assists using Saturn produce results less efficient in both DV and Solar distance than Jupiter assists. This is to be expected since Saturn is further from the Sun, requiring a larger DV impulse to reach it, and is also a less massive body, and so provides a smaller velocity change during the gravity assist itself.

Figure 5.21: Required DV against final Solar distance for all found Saturn gravity assist trajectories. Each colour represents a different synodic period.

Figure 5.22: Pareto front of required DV against final Solar distance for the most efficient Saturn gravity assist trajectories. Each colour represents a different synodic period.

5.2.4. Gravity-Assist Preliminary Results Summary

To summarise, a series of potential gravity-assist trajectories have been identified, using both Jupiter and Saturn as target bodies. Due to the small diversity of the global optimisation solutions, generally only providing trajectories over a relatively small launch window, it has been decided to move forward using all trajectories on the Pareto front identified by the optimisation over each synodic period; this ensures many possible launch dates and varied trajectory geometry, allowing for a more full analysis of the use of an EDT over some of these trajectories.

6

Mission Profile Results

This chapter covers the results of the main analysis of this thesis project, namely the comparison between mission profiles where an EDT could be used. Each mission profile has its results presented individually, followed by a general summary of the results.

6.1. SSO+ Performance Results

This section covers the results obtained from the optimisation analysis of the SSO+ profile as described in Section 3.3. Figure 6.1 shows the relationship between the initial aphelion, and the aphelion change from the start to the end of the simulation, for both the initial generation, shown in blue, and the final generation, shown in orange.

Inspecting the first generation results it can be seen that in general, the larger the initial aphelion, the larger the aphelion change, which is to be expected as these eccentric orbits tend to require less energy for a comparable aphelion increase than the less eccentric ones. It can also be seen from the final generation results that the high initial aphelion cases are most optimal, which is to be expected, but also that there is some spread in the aphelion change. The most important thing to note from this figure however is that the aphelion change is very small, on the order of 0.01 AU, indicating the very poor performance of the EDT spacecraft even over a long TOF; this is of course expected after finding the very weak acceleration provided by the EDT in Section 5.1.
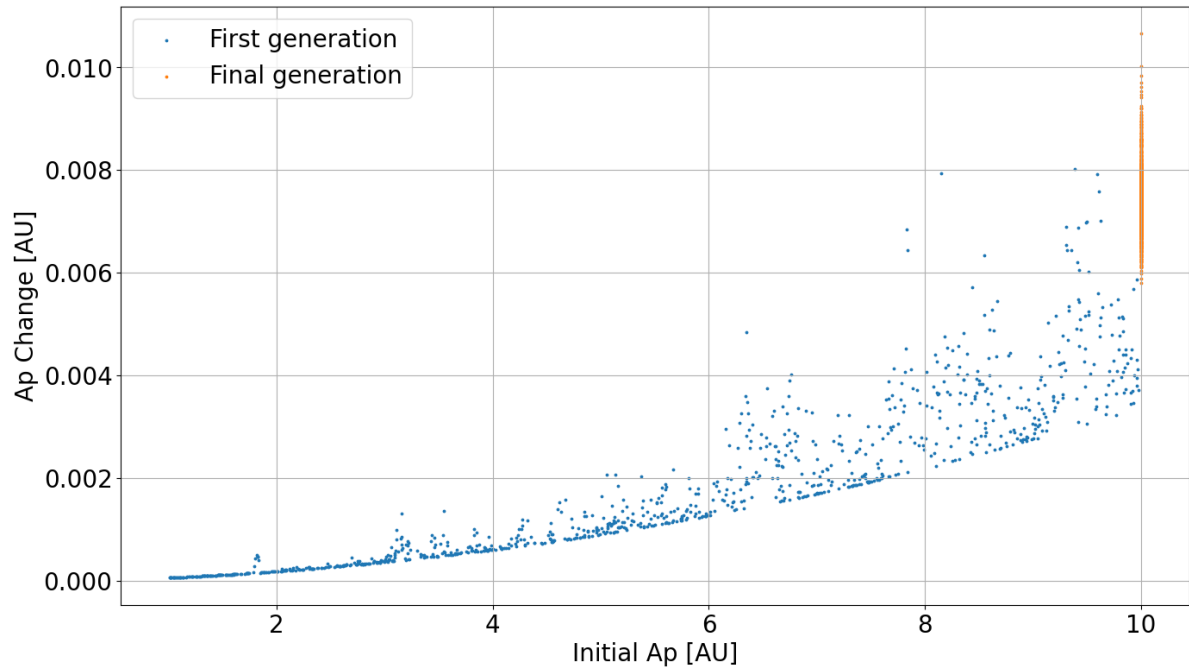
Figure 6.1: SSO+ trajectory initial aphelion vs maximum aphelion.

Figure 6.2 shows the launch date plotted against the maximum aphelion, with the first generation shown in blue, while the final generation is in orange. It can be seen that in the initial generation there is no discernible relationship between launch year and maximum achieved Aphelion, whereas after optimisation in the final generation, solutions appear to cluster around the years 2030 and 2040.
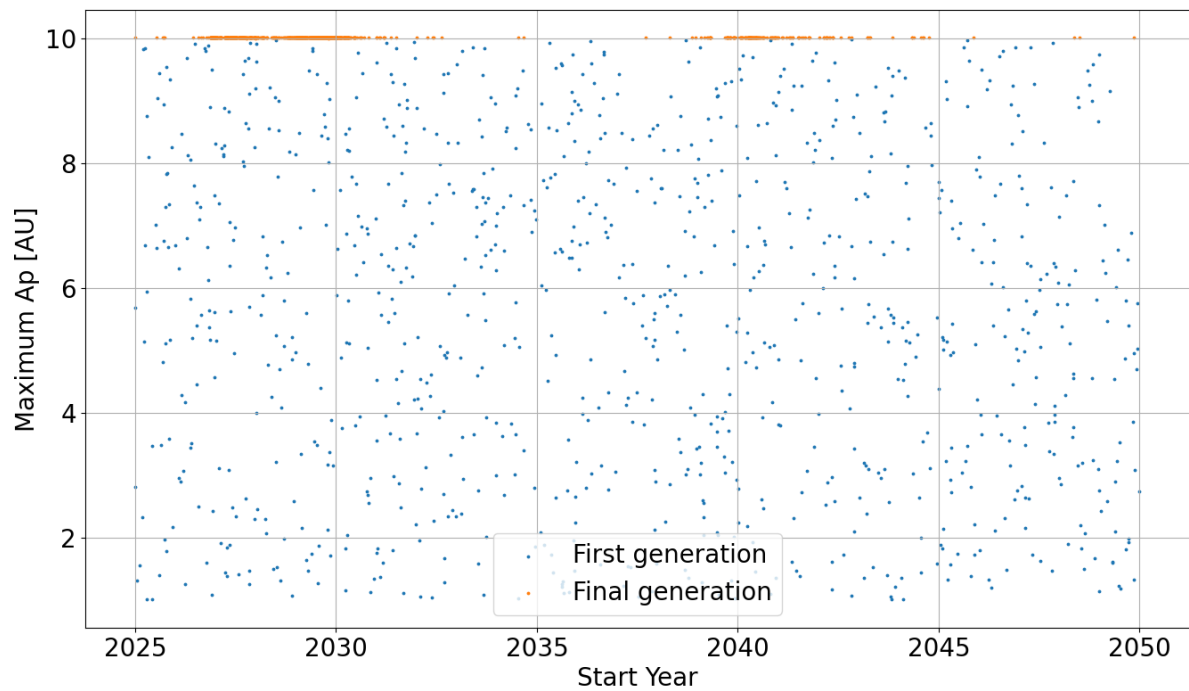

Figure 6.2: SSO+ trajectory initial launch year vs maximum aphelion.

The trajectory found to be most optimal, that is the one with the largest maximum aphelion, can be seen in Figure 6.3, which has a launch year of 2029.5, an initial aphelion of 10.0 AU, and a maximum aphelion of 10.01 AU.
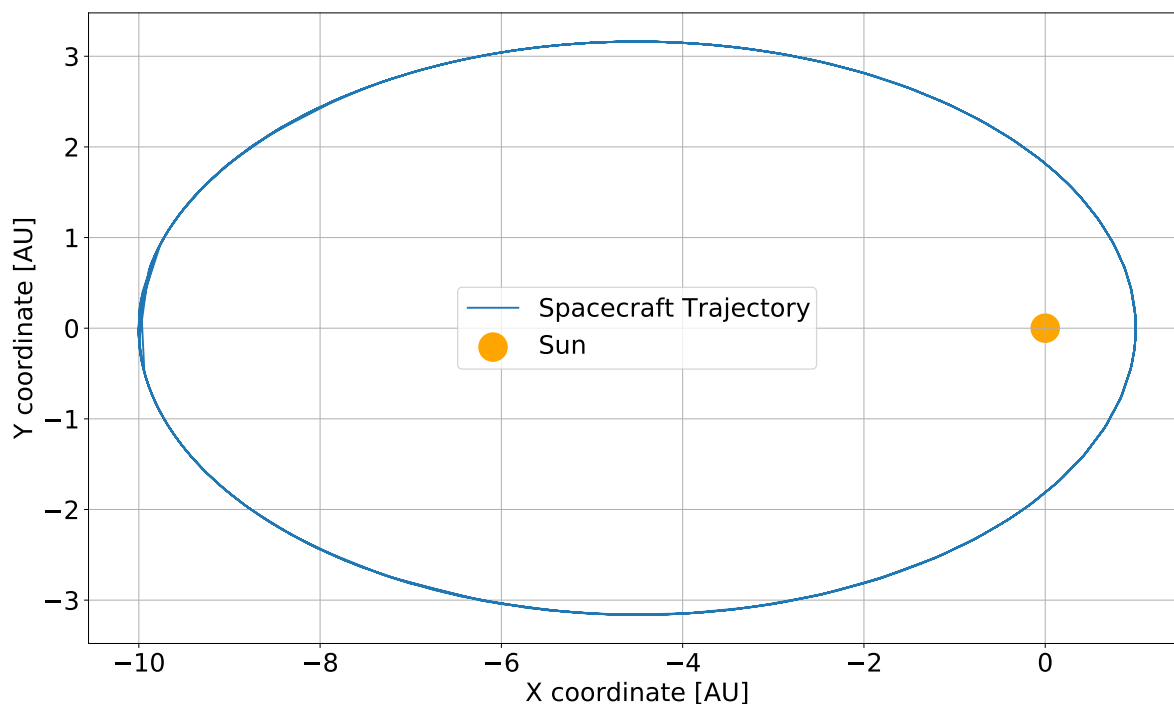

Figure 6.3: The most optimal trajectory of the SSO+ mission profile optimisation.

The difference between initial and final aphelions was only 0.01 AU, clearly showing that the EDT in the SSO+ profile configuration using an EDT has severe performance limitations, as can be seen by Figure 6.3, which has no discernible changes to the initial orbit. Table 6.2 gives a clear summary of the performance of the SSO+ profile, in addition to the performance of the alternate seed value; it can be seen that the performance characteristics are comparable, and so the optimisation routine can be considered robust.

Table 6.1: Comparison of SSO+ results using different seeds.

Seed Value	Launch Year	Initial Aphelion [AU]	Maximum Aphelion [AU]
97	2029.499	10.0	10.0097
1264899	2029.496	10.0	10.0110

6.2. InO Performance Results

This section covers the results obtained from the optimisation analysis of the InO profile as described in Section 3.3. Figure 6.4 shows the relationship between the initial perihelion, and the aphelion change over the course of the simulation, for both the initial generation shown in blue, and the final generation shown in orange; the plot shows that most trajectories when chosen randomly (i.e. in the first generation) provide very little aphelion change over the course of the simulation, regardless of initial Pe. It also shows that after optimisation, there is a small cluster of optimal trajectories, which have initial Pe values on the lower end of the range, which is to be expected as generally more EDT acceleration can be achieved when moving faster through a stronger magnetic field, which is the case at smaller Solar distances. It can already be seen that the aphelion change in the InO case is smaller than in the SSO+ case shown in Figure 6.1
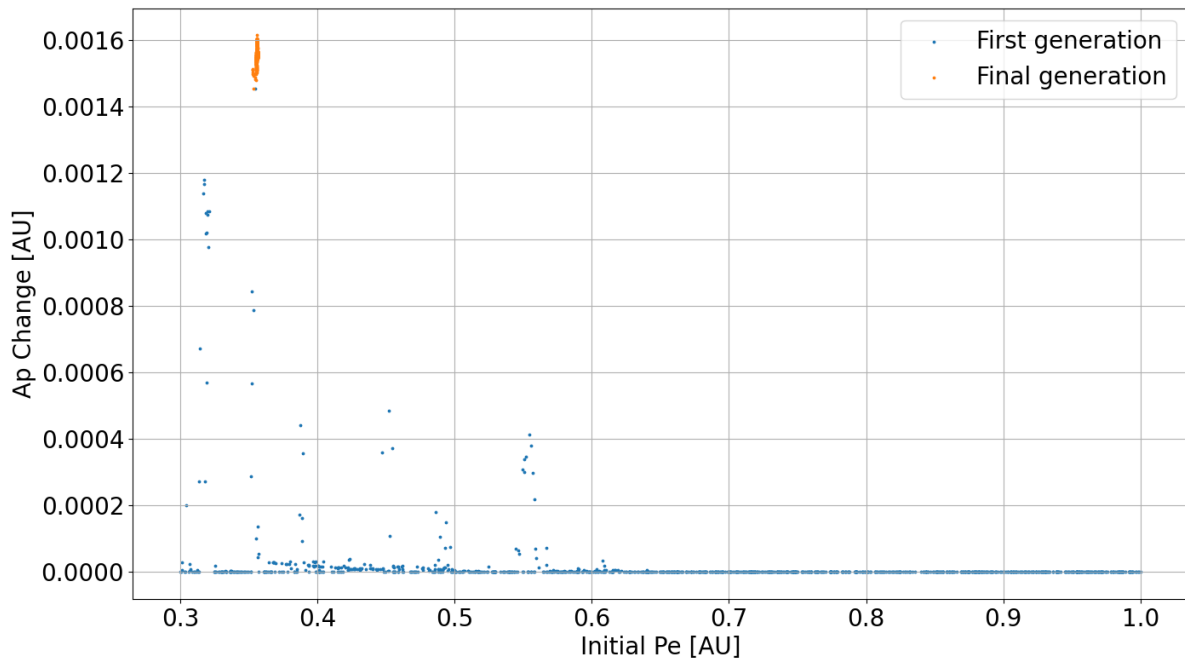

Figure 6.4: Initial EDT perihelion vs aphelion change during simulation, for the InO case.

Figure 6.5 shows the target perihelion plotted against the overall aphelion change; it can be seen that in the initial generation, most trajectories do not provide an aphelion change at all, whereas after optimisation, there are solutions clustered around target perihelion values of 0.4 AU and 0.85 AU, with approximately equal performance. The reasoning for this clustering is somewhat unclear, and although it does not affect the overall results, it should be noted when embarking on any future research.
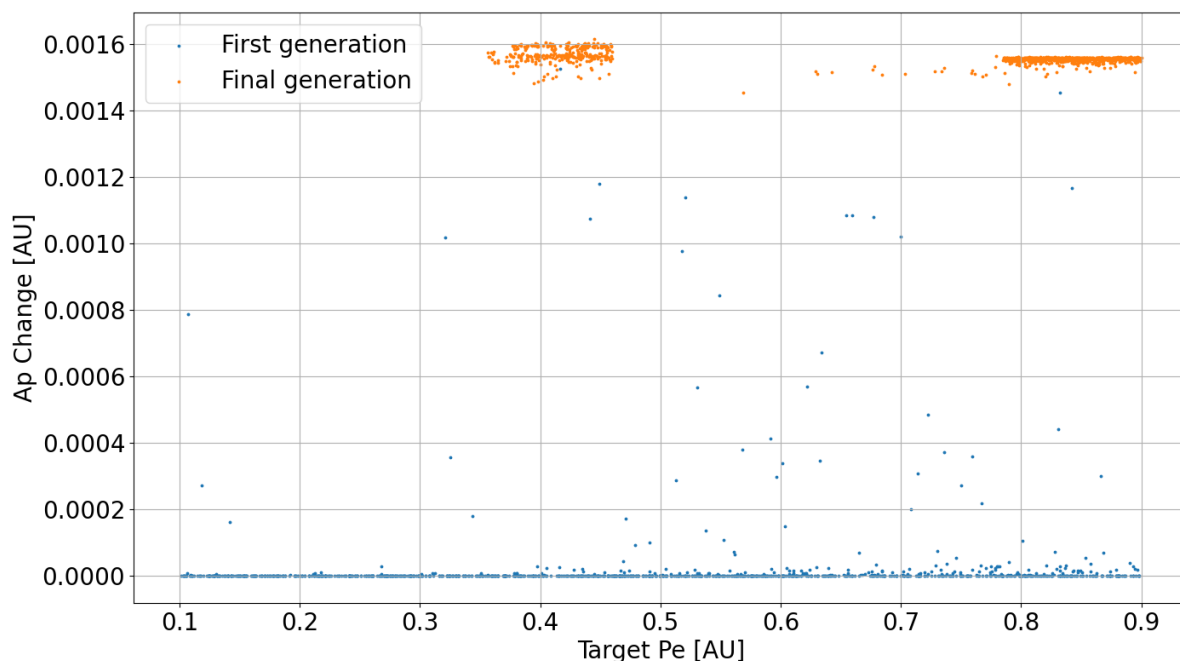
Figure 6.5: EDT target perihelion vs aphelion change during simulation, for the InO case.

Figure 6.6 shows the launch year plotted against the maximum aphelion achieved; it can be seen that in the first generation there is no clear relationship between the two values, which is to be expected. After optimisation however, solutions are found across the launch date range, with a slight favour to earlier dates; it should also be noted that all solutions achieve approximately equal performance. This behaviour is essentially expected, since the simulation time is long enough that relatively short-term changes such as magnetic field strength fluctuations are evened out.
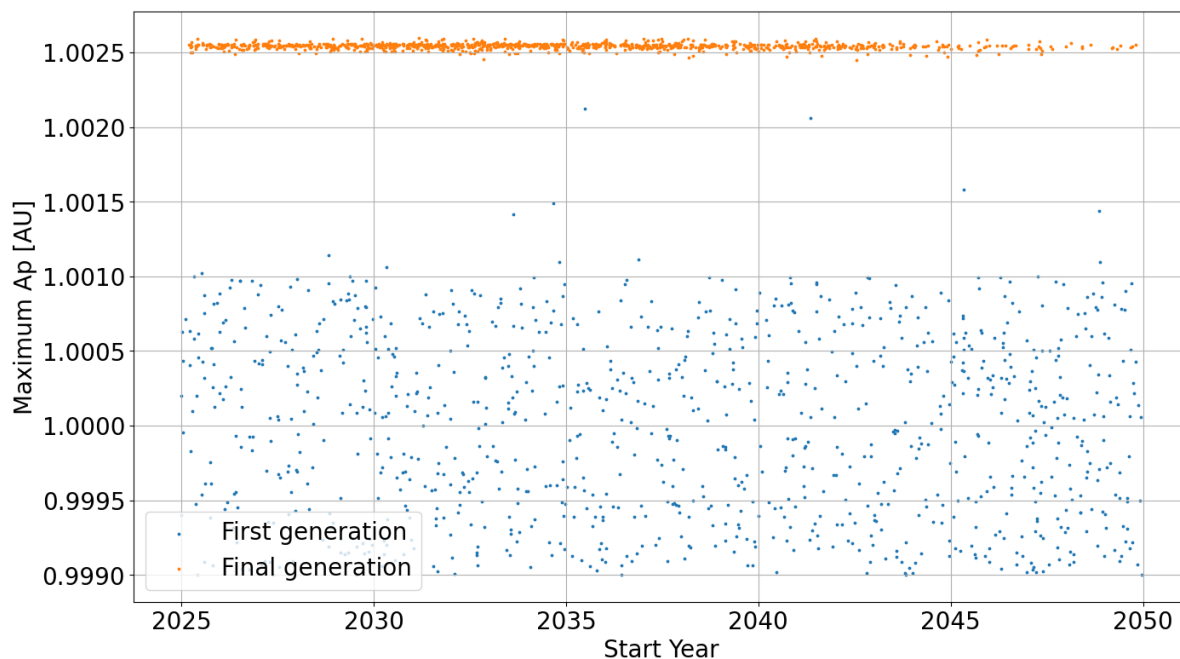

Figure 6.6: EDT launch year vs maximum achieved aphelion, for the InO case.

The InO trajectory found to be most optimal can be seen in Figure 6.7, which shows the first stage of the trajectory in orange (the retrograde portion) and the second stage of the trajectory (the prograde portion) in blue. The trajectory has a launch year of 2031.2, initial perihelion of 0.36 AU, target perihelion of 0.45 AU, and a maximum achieved aphelion of 1.003 AU.
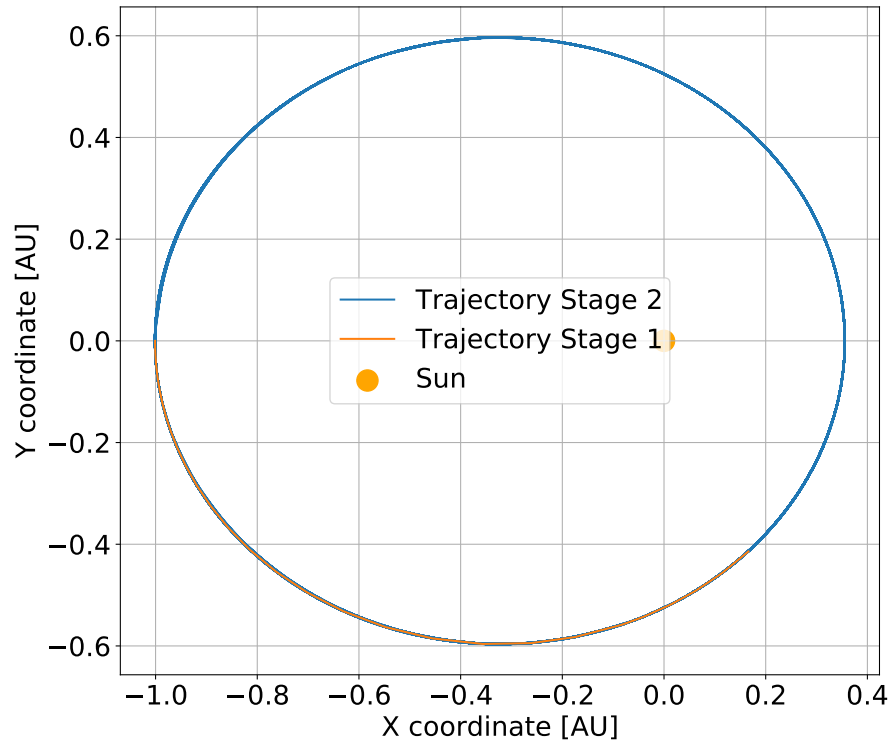

Figure 6.7: The most optimal trajectory of the InO mission profile optimisation; the first stage of the flight is shown in orange, while the second stage is in blue.

The difference between the initial and final aphelions for this case was only around 0.003 AU, clearly showing that like the SSO+ case, the InO profile configuration has severe performance limitations, which can be observed in Figure 6.7, which has no discernible change in the orbit. Table 6.2 provides a clear presentation of the performance of the InO mission profile, along with the performance of the alternative seed case, which has comparable performance, and therefore the optimiser can be considered robust.

Table 6.2: Comparison of InO results using different seeds.

Seed Value	Launch Year	Initial Perihelion [AU]	Initial Target Perihelion [AU]	Maximum Aphelion [AU]
97	2031.170	0.356	0.453	1.0026
1264899	2030.516	0.356	0.449	1.0026

6.3. SOKGA Performance Results

This section covers the results obtained from the optimisation analysis of the SOKGA profile as described in Section 3.3. Figure 6.9 shows all the simulated SOKGA trajectories, with blue and orange points showing those trajectories using Jupiter and Saturn gravity assists respectively. For each individual trajectory type there is a clear relationship between TOF and velocity at 100 AU, with longer TOFs generally having lower velocities, which is of course to be expected. Also shown in red are the most optimal points for this trajectory type which should maximise velocity while minimising TOF, in this case there is only a single optimal trajectory, which is shown in Figure 6.9.
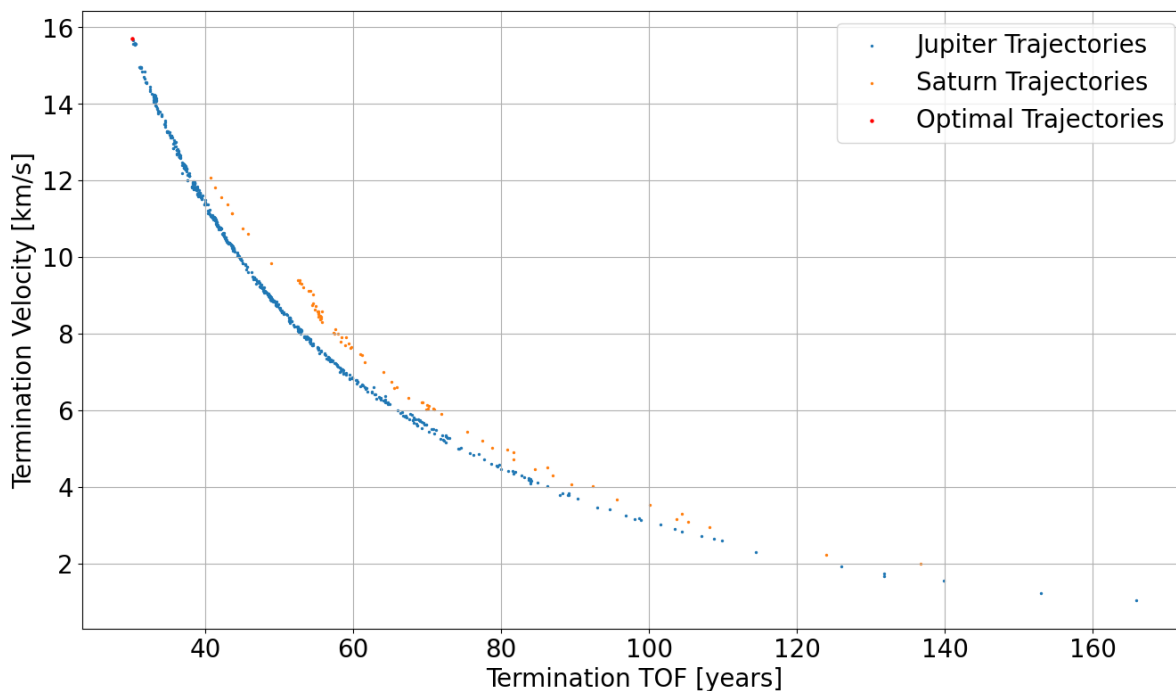

Figure 6.8: Scatter plot of simulated SOKGA trajectories. Blue and orange points show Jupiter and Saturn assist trajectories respectively; red points show the most optimal trajectories.
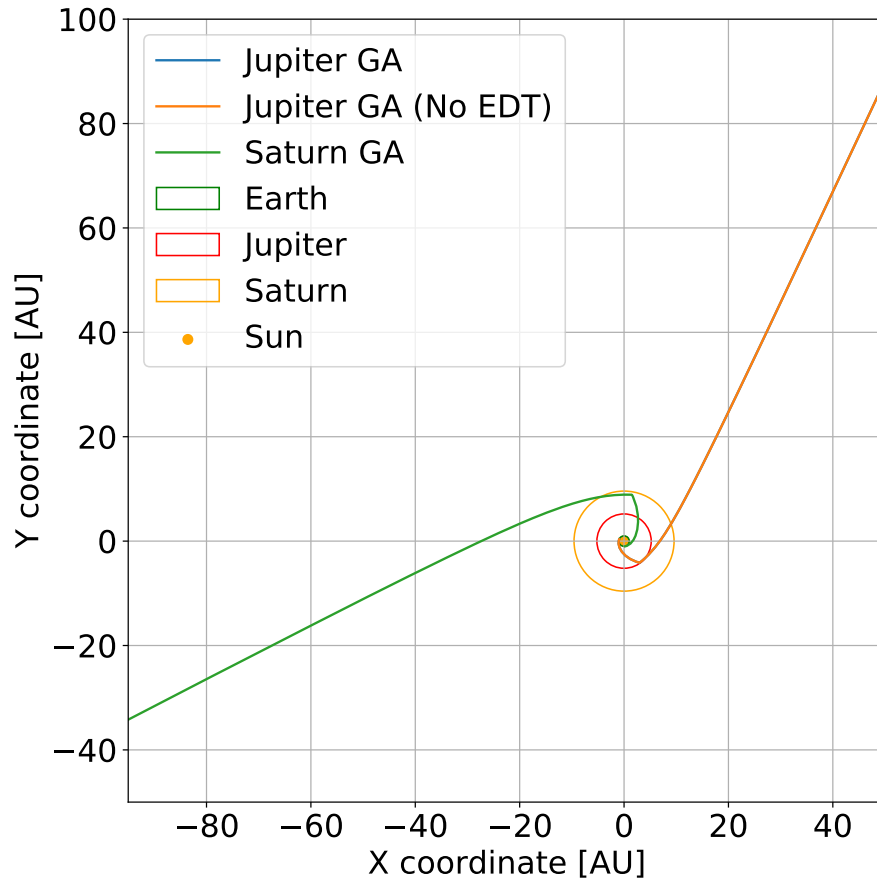
Figure 6.9: Most efficient SOKGA trajectories, in the case of both a Jupiter and Saturn gravity assist, along with a reference trajectory that shows the Jupiter trajectory with no EDT enabled.

The most optimal trajectory shown in Figure 6.9 has a launch date of 2043.2, utilising a Jupiter gravity assist. A clear summary of the plotted trajectories can be seen in Table 6.3; the table clearly shows that like both the SSO+ and InO profiles, the effect of the EDT on the trajectory is practically negligible, only providing a TOF improvement of around 45 days over a total TOF of over 30 years. The terminal velocity is similarly underwhelming, with only a 3 m/s increase compared to a fully ballistic trajectory.

Table 6.3: Comparison of SOKGA trajectories using different assist bodies, as well as comparing against a simple ballistic trajectory.

Trajectory	Launch Year	Termination TOF [years]	Termination Velocity [km/s]
Jupiter assist (with EDT)	2043.158	30.14	15.700
Jupiter assist (without EDT)	2043.158	30.26	15.697
Saturn assist (with EDT)	2028.505	40.78	12.076

6.4. Overall Results Summary

After running simulations for different trajectory types, Table 6.4 gives a summary of the performance of each of the mission profiles; since SSO+ and InO use the same performance metric, these can be directly compared quantitatively, whereas SOKGA cannot. Therefore a fourth column giving a qualitative description of the performance is also given.

Table 6.4: Summary of EDT performance using the SSO+ and InO trajectories, over a given simulation TOF.

Profile Type	Simulation Time [Years]	Max Aphelion Increase [AU]	Performance Description
SSO+	100	0.01	Severely limited
InO	100	0.002	Severely limited
SOKGA	30 - 40	-	Severely limited

As can be seen in Table 6.4, for all of the assessed profiles, the performance can be described as severely limited, meaning that in the present configuration, the EDT system does not provide an appealing means of propulsion.

<div style="text-align: right; font-size: 3em;">7</div>

Sensitivity Analysis

In this section, a sensitivity analysis is conducted, to assess how sensitive the results found in Chapters 5 and 6 are to different parameters. This is done for EDT configuration parameters, followed by mission profile parameters.

7.1. Sensitivity Analysis Setup

Firstly, the setup of the sensitivity analysis can be outlined in this section. In general, the nominal setup is used as a baseline, and each chosen sensitivity parameter is varied individually with respect to that baseline, and compared against the nominal case; therefore a full optimisation is not run again, since the time required for this would simply be too large. The specific parameters chosen and accompanying setup information is specified further for each case in the following subsections.

It should also be noted that whenever a range is defined for a sensitivity parameter, the analysis of it involves a discretised linearly spaced range, of size 1000, in order to provide sufficient fidelity.

7.1.1. EDT Configuration Parameter Sensitivity Setup

An initial analysis on many parameters was conducted in Chapter 5, however there were a number of parameters not directly considered there which can be analysed here; it is from that section that the nominal values are also taken where appropriate. The overall simulation setup is the same as the nominal case outlined in Chapter 5, and so essentially uses an SSO+-style mission profile.

It should be noted that the sensitivity is gauged against the main performance metric also used in Chapter 5, namely the achieved acceleration.

The assessed parameters can be split into 2 general categories: Hoytether properties and material properties, referring to sizing parameters of the Hoytether, and tether material properties respectively. The specific parameters, nominal values, and assessed ranges can be seen in Table 7.1; the Hoytether properties are those not directly assessed in Chapter 5, while the material properties were chosen to gauge the benefits of improved materials. It should be noted that initially, an assessment of the effect of SRP perturbation parameters on the sensitivity of the system had been envisioned, however SRP perturbations had to be disabled from the simulation environment, when it became clear that those perturbations became dominant over the EDT forces, and so made reading results more difficult.

<div style="text-align: center;">93</div>

Table 7.1: Sensitivity analysis values and ranges, for EDT configuration parameters.

Parameter	Symbol	Unit	Nominal Value	Range
Hoytether Properties				
Primary line separation ratio	k_a	-	100	10 - 1000
Secondary tether diameter	D_s	mm	1	0.1 - 100
Secondary tether area ratio	$k_{A,s}$	mm	0.5	0 - 1
Slack coefficient	k_s	-	1.005	1 - 1.1
Material Properties				
Shell resistivity	$\rho_{r,s}$	Ωnm	26.5	10 - 40
Core resistivity	$\rho_{r,c}$	Ωnm	16.8	10 - 40
Shell density	ρ_s	g/cm^3	2.78	1.5 - 10.0
Core density	ρ_c	g/cm^3	8.92	1.5 - 10.0

A further explanation of the parameters in Table 7.1, as well as their nominal and chosen ranges, can be seen below:

Primary line separation ratio k_a - the nominal value is 100, with a chosen value range of 10 - 100, on a linear scale. This is a newly introduced parameter to quantify the primary line separation, a, relative to the primary tether diameter, D, and is calculated using Equation 7.1. The nominal value was arrived at by simply using the example EDT given in [16] as an example, which has primary line separation and tether diameter of 5cm and 0.54m respectively, giving a separation ratio of 92.6, which is rounded up to 100. The range was then simply chosen as 1 order of magnitude above and below the nominal.

$$k_a = \frac{a}{D} \tag{7.1}$$

Secondary tether diameter D_s - the nominal value and range are identical to that of the primary tether diameter described in Chapter 5, but is now varied independently of the primary diameter.

Secondary tether area ratio $k_{A,s}$ - similarly to the secondary tether diameter, $k_{A,s}$ has a nominal value and range identical to its primary ratio counterpart in Chapter 5, but can now also be varied independently.

Slack coefficient k_s - the slack coefficient defined in Section 2.5, has a nominal chosen value the same as the one described in [16]. The lower limit of its range, a value of 1.0, is the most exreme possible value, in which there is no slack; the upper bound of 1.1 however is chosen fairly arbitrarily.

Shell resistivity $\rho_{r,s}$ - the shell is nominally made from aluminium, and therefore the nominal value is simply that of aluminium. However, the sensitivity range is chosen relatively arbitrarily, with the lower limit in the region of that of copper, and the upper limit around twice that of aluminium.

Core resistivity $\rho_{r,c}$ - the core is nominally made from copper, and therefore the nominal value is simply that of copper. The sensitivity range is the same as that chosen for the shell resistivity.

Shell density ρ_s - the shell is nominally made from aluminium, and therefore the nominal value is simply that of aluminium. The lower limit of the sensitivity range is chosen to be a value approximating materials such as carbon nanotubes with a density of around 1300 kg/m^3 [51], since this is the lowest material density that is reasonably conceivable. The upper bound is approximately that of copper, which is one of the most dense materials that may be considered.

Core density ρ_c - the core is nominally made from copper, and therefore the nominal value is simply that of copper. The sensitivity range is the same as that chosen for the shell density.

7.1.2. Mission Profile Parameter Sensitivity Setup

A sensitivity analysis is also run on a number of parameters relating to the mission profile setup; which parameters are relevant to each specific mission profile may vary, and are shown in Table 7.2. In the table each parameter is named, and for each mission profile a "Y" or "N" is present standing for "Yes" and "No", indicating the use of that parameter in the analysis; it can be clearly seen that most parameters are run for most mission profiles, with the exception of initial AOP, which is not analysed for the SOKGA cases, since the value is predefined by the gravity assist used.

Table 7.2: Sensitivity analysis parameters which are run, for each mission profile type. Y and N stand for Yes and No respectively, indicating whether or not that parameter is to be assessed for that profile type.

Parameter	Symbol	SSO +	InO	SOKGA
Magnetic Field Parameters				
IMF Azimuthal Angle	ϕ_0	Y	Y	Y
IMF Strength	B_0	Y	Y	Y
Initial Orbit Parameters				
Argument of Perihelion	AOP	Y	Y	N

The parameters were chosen as those parameters able to directly affect the EDT performance; the interplanetary magnetic field (IMF) azimuthal angle affects performance as it dictates the orientation of the produced force, with smaller values producing a more along-track force. The IMF strength also clearly affects the EDT performance, as the stronger the field, the stronger the achievable thrusting force. The initial AOP should have little or no effect on the shown EDT profiles, since the magnetic field is symmetric around the Sun, however was implemented as preparation for the (now removed) EDGE and α-c profile analyses, and it was decided to leave the information in.

Table 7.3 shows the nominal and sensitivity ranges for each of the parameters mentioned in Table 7.2. The nominal IMF azimuth angle is the one decided on in Section 2.3, and its range encompasses all mathematically possible angles for the IMF azimuth. In reality the range would be much smaller, but all values are included for completeness. It should be noted that in the case of IMF strength, B_0 is split into its component estimation parameters, as described in Section 2.3, which are individually varied; the ranges for each of the values are chosen fairly arbitrarily, being simply $\pm$ 100% of the nominal value, which is sufficient to give an idea of the parameters' effect on EDT performance. Finally the AOP nominal value is chosen arbitrarily at 0°, while the range encompasses all possible values.

Table 7.3: Sensitivity analysis values and ranges, for mission profile parameters.

Parameter	Symbol	Unit	Nominal Value	Range
Magnetic Field Parameters				
IMF Azimuthal Angle	ϕ_0	deg	42.748	0 - 90
IMF Strength (Estimation Parameter 1)	a_1	nT	1.00	0 - 2
IMF Strength (Estimation Parameter 2)	a_2	nT	1.50	0 - 3
IMF Strength (Estimation Parameter 3)	b_1	-	0.10	0 - 0.2
IMF Strength (Estimation Parameter 4)	b_2	-	0.57	0 - 1.14
IMF Strength (Estimation Parameter 5)	c_1	-	4.00	0 - 8
IMF Strength (Estimation Parameter 6)	c_2	-	-2.90	-5.8 - 0
IMF Strength (Estimation Parameter 7)	d	nT	6.20	0 - 12.4
Initial Orbit Parameters				
Argument of Perihelion	AOP	deg	0	0 - 360

7.2. Configuration Parameter Sensitivity Results

This section covers the results of the sensitivity analysis for EDT configuration parameters, as set up in Subsection 7.1.1. Each parameter is first individually addressed, followed by a short summary.

7.2.1. Primary Line Separation Ratio

Figure 7.2 shows that the larger the primary line separation ratio k_a, the lower the EDT performance, and the performance decreases more drastically as k_a is further increased. This is to be expected, since a larger k_a also produces a slightly longer secondary link length, and therefore adds to the mass of the spacecraft. However it can also be clearly seen that the performance is generally insensitive to k_a, with the total change in acceleration in the order of 0.1 pm/s^2.
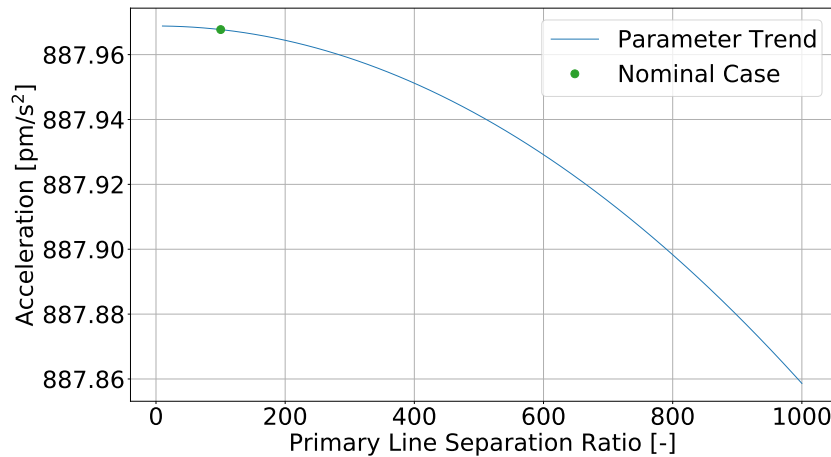

Figure 7.1: Achieved acceleration performance of EDT while varying primary line separation ratio k_a. The blue line shows the trend, while the green point shows the nominal case.

7.2.2. Secondary Tether Diameter

Figure 7.2 shows that in general, the larger the secondary tether diameter D_s, the lower the EDT performance. The rate of performance decay begins relatively unpronounced in the region of approximately 1 mm in diameter, before having a drastic impact on performance in the 1-20 mm range, before again having a much smaller rate of performance impact beyond 20 mm. It can also be seen that the sensitivity is very strong, with the accelerations ranging from over 2000 pm/s^2 at very small D_s values, down to almost 0 pm/s^2 at large D_s values, with the nominal case being somewhere in the middle. It is clear to see that significant performance gains could be achieved, by reducing the secondary tether diameter where possible.
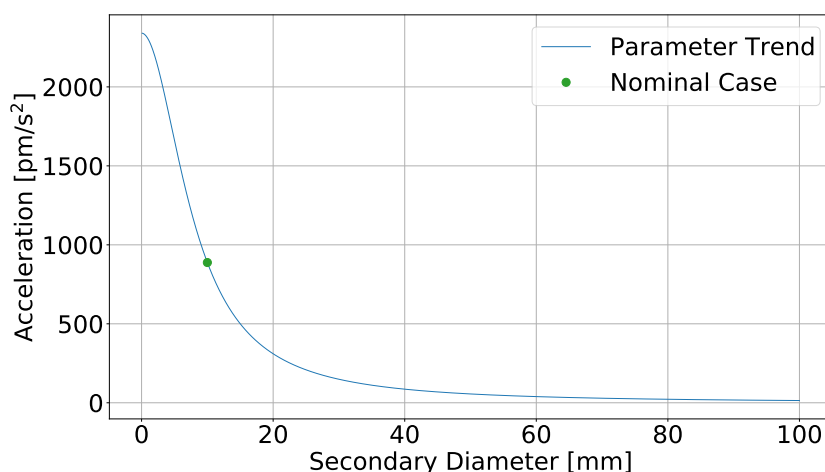
Figure 7.2: Achieved acceleration performance of EDT while varying secondary tether diameter D_s. The blue line shows the trend, while the green point shows the nominal case.

7.2.3. Secondary Tether Area Ratio

Figure 7.3 shows that in general, the larger the secondary area ratio $k_{A,s}$, the better the EDT performance; the relationship is non-linear, with the rate of performance increase increasing more rapidly at higher values of $k_{A,s}$. The magnitude of the sensitivity is quite significant, with the EDT acceleration more than doubling over the range of area ratios; although there is of course no room for improved performance, as the nominal case is already at the optimal point. This behaviour is expected, as it was also the case for the primary area ratio.
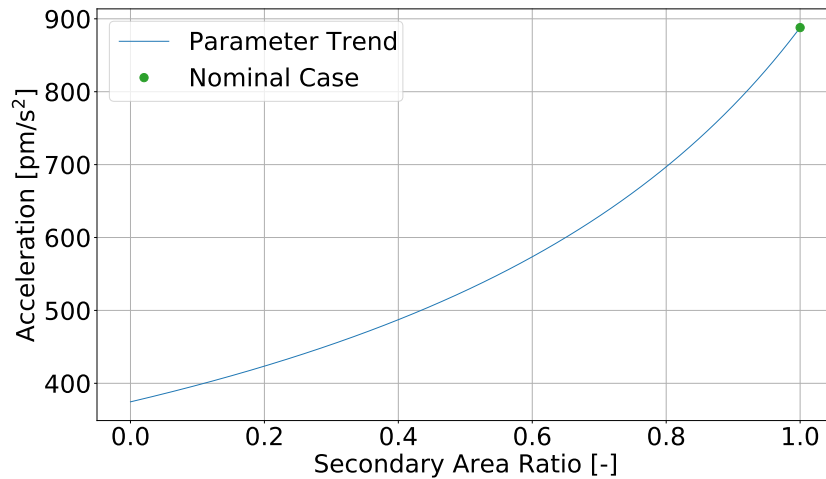
Figure 7.3: Achieved acceleration performance of EDT while varying secondary tether area ratio $k_{A,s}$. The blue line shows the trend, while the green point shows the nominal case.

7.2.4. Slack Coefficient

Figure 7.4 shows that in general, the larger the slack coefficient k_s, the lower the EDT performance; the relationship is linear, with a drop in acceleration of around 50 pm/s^2, per k_s increase of 0.1. This is to be expected, as the more slack there is in the tether, the more material needed and therefore the spacecraft mass must increase. The magnitude of the sensitivity is not negligible, although the performance that can be gained from reducing k_s relative to its nominal value is quite small, being only around 2 or 3 pm/s^2.
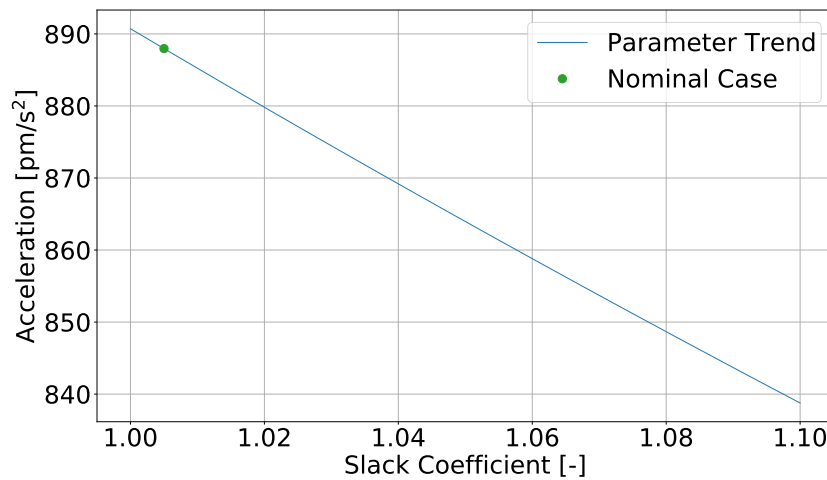
Figure 7.4: Achieved acceleration performance of EDT while varying slack coefficient k_s. The blue line shows the trend, while the green point shows the nominal case.

7.2.5. Shell Resistivity

Figure 7.5 shows that in general, the larger the shell resistivity $\rho_{r,s}$, the higher the EDT performance; the relationship is linear, with a not insignificant increase in acceleration of around 25 pm/s^2, over an increase in $\rho_{r,s}$ of 20 Ωnm.
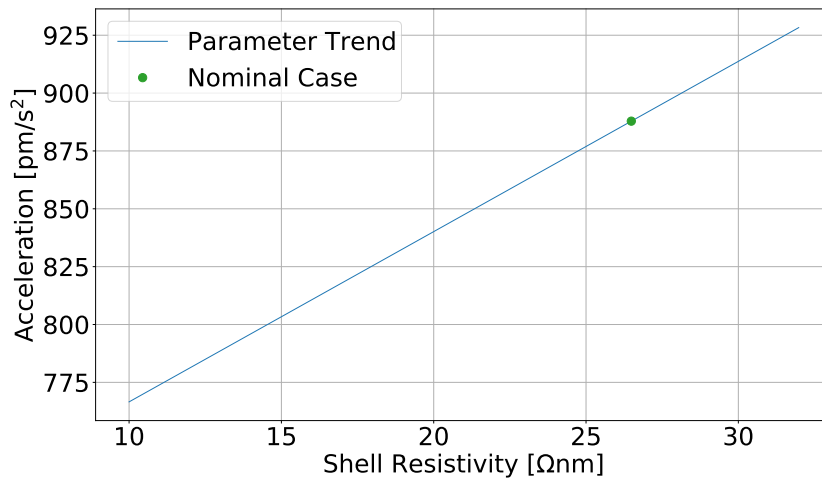

Figure 7.5: Achieved acceleration performance of EDT while varying shell resistivity $\rho_{r,s}$. The blue line shows the trend, while the green point shows the nominal case.

7.2.6. Core Resistivity

Figure 7.6 shows that changing core resistivity $\rho_{r,c}$ has no effect on EDT performance. This is to be expected, since in the nominal case the tether has an area ratio of 1.0, essentially meaning that there is no core material, and so cannot affect performance.
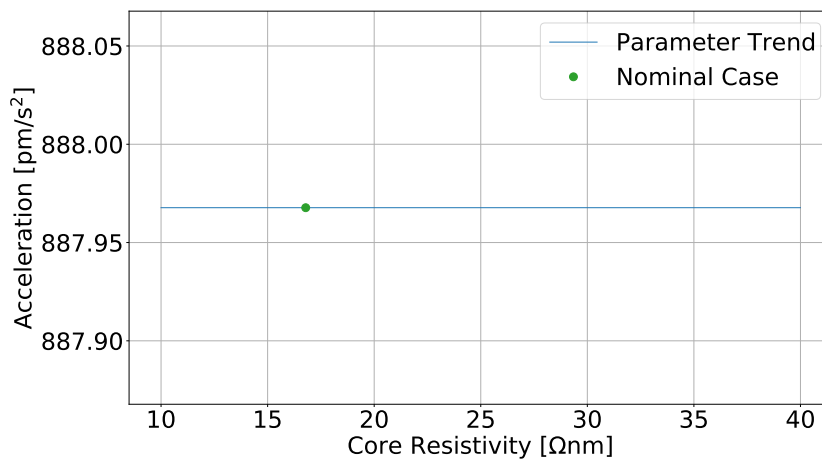

Figure 7.6: Achieved acceleration performance of EDT while varying core resistivity $\rho_{r,c}$. The blue line shows the trend, while the green point shows the nominal case.

7.2.7. Shell Density

Figure 7.7 shows that in general, the larger the shell density ρ_s, the higher the EDT performance; the relationship is non-linear, with the effect on performance being more pronounced at lower values of ρ_s. The magnitude of the sensitivity is quite high, ranging from an EDT acceleration of around 1500 pm/s^2 at lower densities, down to around 300 pm/s^2 at higher densities; the relationship is of course expected, as a higher density tether results in more spacecraft mass, and since the mass is dominated by the tether, this can cause significant changes in performance. These performance changes highlight that the ability to use conducting materials with a density similar to that of carbon fibre for the tether, could help make the concept more feasible.
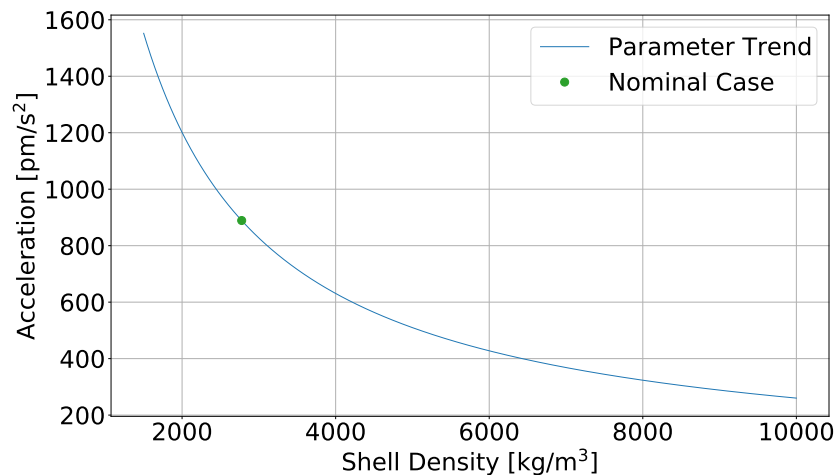

Figure 7.7: Achieved acceleration performance of EDT while varying shell density ρ_s. The blue line shows the trend, while the green point shows the nominal case.

7.2.8. Core Density

Figure 7.8 shows that core density ρ_c has no effect on EDT performance. This is to be expected, for the same reason that $\rho_{r,c}$ has no affect on performance: there is no core material in the nominal case.
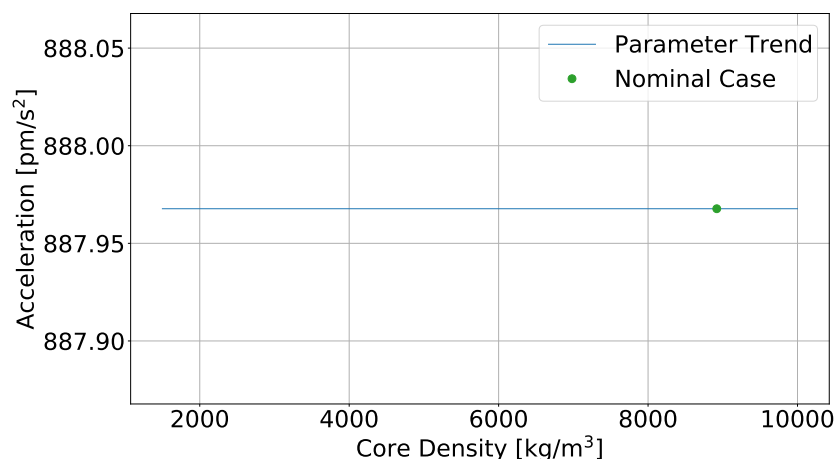

Figure 7.8: Achieved acceleration performance of EDT while varying core density ρ_c. The blue line shows the trend, while the green point shows the nominal case.

7.2.9. Configuration Paramter Sensitivity Analysis Summary

Table 7.4 summarises the above results, qualitatively describing the behaviour and strength of each parameter on EDT performance (evaluated on acceleration). Strength can be "very strong", "strong", "weak", "negligible", or "none"; these are fairly self-explanatory, with the difference between categorisations generally being in orders of magnitude; these categories are highlighted by the use of graduated red and green row filling.

Table 7.4: Sensitivity parameter effects on EDT performance, for configuration parameters. The table qualitatively describes both behaviour and the magnitude (ie strength) of the effect.

Parameter	Symbol	Behaviour	Strength
Primary line separation ratio	k_a	Non-linear decrease	Negligible
Secondary tether diameter	D_s	Non-linear decrease	Very Strong
Secondary tether area ratio	$k_{A,s}$	Non-linear increase	Strong
Slack coefficient	k_s	Linear decrease	Weak
Shell resistivity	$\rho_{r,s}$	Linear increase	Weak
Core resistivity	$\rho_{r,c}$	None	None
Shell density	ρ_s	Non-linear decrease	Very Strong
Core density	ρ_c	None	None

Table 7.4 shows that EDT performance is fairly insensitive to many of the sensitivity parameters, with the exception of Secondary tether diameter D_s, and shell density, ρ_s; these parameters can be used to further focus future applications of EDTs, as well as highlighting that they should be paid particular attention.

7.3. Mission Profile Parameter Sensitivity Results

This section covers the results of the sensitivity analysis for mission profile parameters, as set up in Subsection 7.1.2. Each parameter is individually addressed for each specific mission profile, with a short summary at the end of the section. It should be noted that the InO profile is addressed first, followed by SSO+ and SOKGA; this is done since InO provides fairly clear results, while SSO+ and SOKGA are somewhat less clear, and require a little further explanation, after the initial insights gained from the InO results.

7.3.1. InO Sensitivity Results

Figure 7.9 shows that as expected, the general performance of the EDT decreases as ϕ_0 increases, as the thrust orientation is closer to along-track for lower ϕ_0 values. The data can however be messy in places, especially above around 45°; it is not entirely clear why this is the case, but may be a result of having a very small component of acceleration actually in the along-track direction at these higher values. The magnitude of the effect on performance is still quite small, with a maximum aphelion increase of only around 0.2 mAU between the nominal case and the best case (which is quite unrealistic).
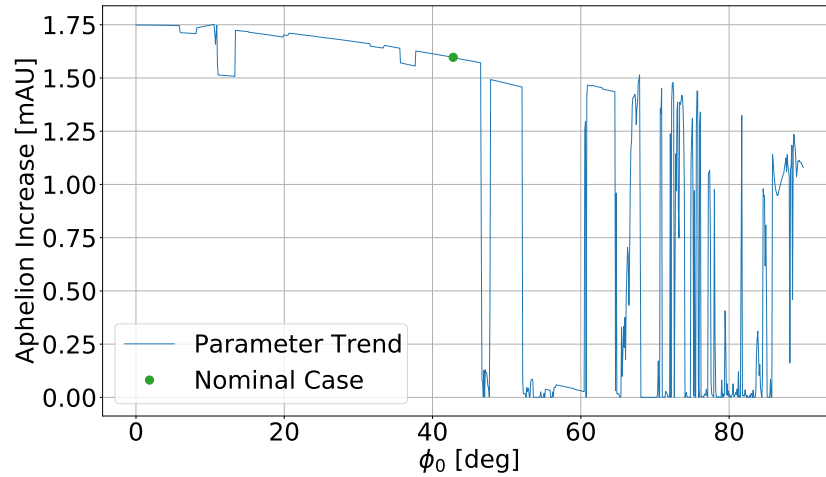

Figure 7.9: Aphelion increase while varying IMF azimuth ϕ_0, for the InO profile type. The blue line shows the trend, while the green point shows the nominal case.

Figure 7.10 shows that as a_1 increases, so too does the performance, with a linear relationship. This can be expected, since a_1 controls the magnitude of the long-period IMF variations, and since the chosen trajectory operates mostly in the peak of one of these oscillations, the performance should increase; the magnitude of the change however is negligible, changing by less than 0.03 mAU.
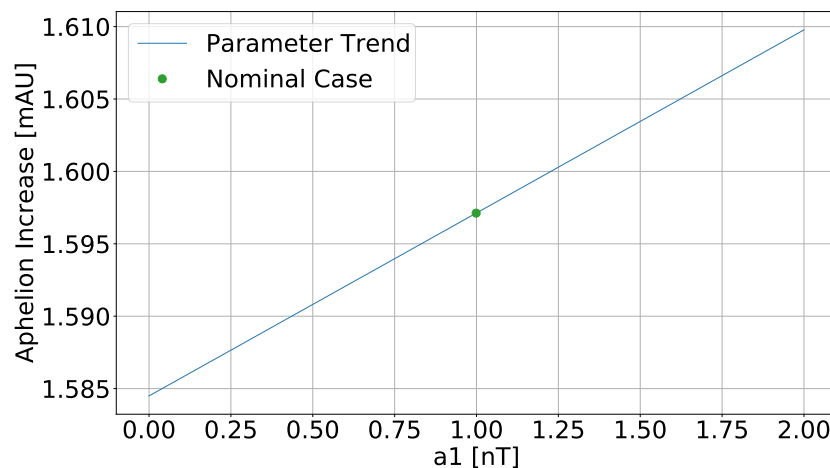

Figure 7.10: Aphelion increase while varying IMF strength estimation parameter a_1, for the InO profile type. The blue line shows the trend, while the green point shows the nominal case.

Figure 7.11 shows that with increasing a_2, EDT performance generally decreases, non-linearly. The reasoning for this is somewhat unclear, but the change is negligible, being less than 0.05 mAU.
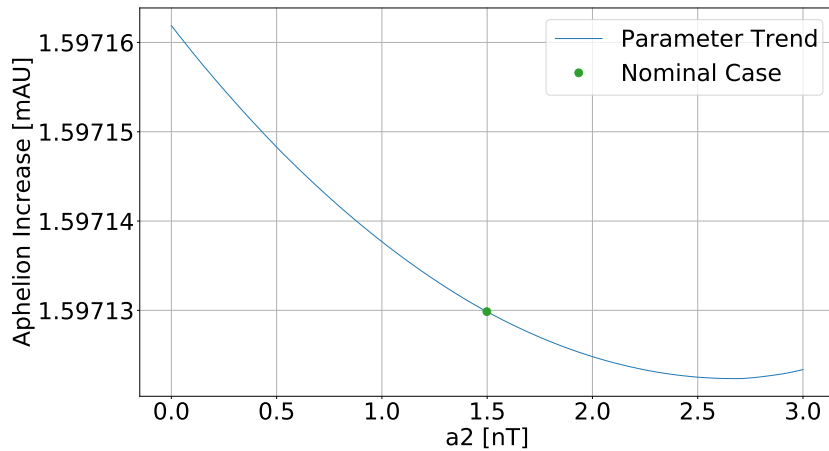

Figure 7.11: Aphelion increase while varying IMF strength estimation parameter a_2, for the InO profile type. The blue line shows the trend, while the green point shows the nominal case.

Figure 7.12 shows a periodic effect on EDT performance, resembling a twin-signal sinusoid, the overall magnitude of which decays with increasing b_1 values. This behaviour makes sense as b_1 controls the period of the long-period IMF strength fluctuations; a smaller b_1 corresponds to a longer period, allowing the spacecraft to stay for a long time in either a peak or trough of IMF strength, causing the extreme variation, while at higher values of b_1 this period is shorter, and so the overall time spent in a peak or trough is more balanced. In the region of the nominal case, the performance is very sensitive, but with a relatively small performance range compared to small b_1 values. Overall the magnitude of the effect of b_1 on EDT performance is quite weak, with a maximum variability of around 0.12 mAU.
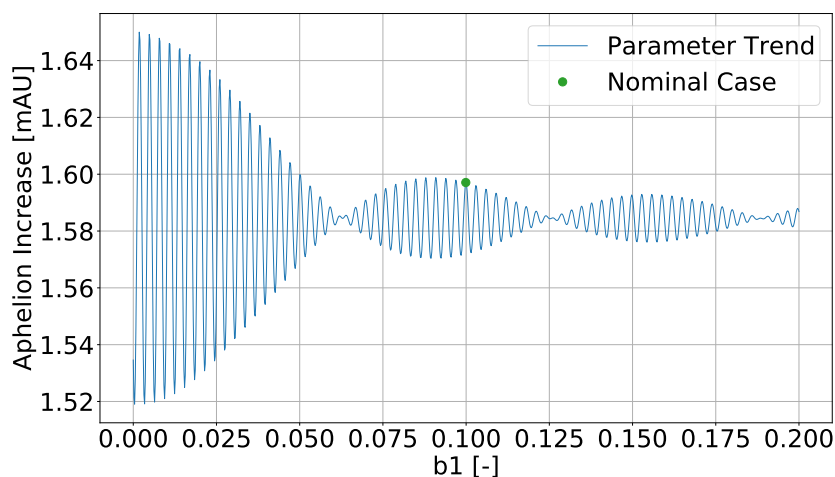

Figure 7.12: Aphelion increase while varying IMF strength estimation parameter b_1, for the InO profile type. The blue line shows the trend, while the green point shows the nominal case.

Figure 7.13 shows a periodic effect on EDT performance while varying b_2, in much the same way as when varying b_1; however, since the oscillations that b_2 controls are naturally higher frequency, the observed oscillations are also of a higher frequency. At very small b_2 values the effect on EDT performance is relatively strong compared to b_1, but at more reasonable values around the nominal case, the variability is negligible, around 0.01 mAU.
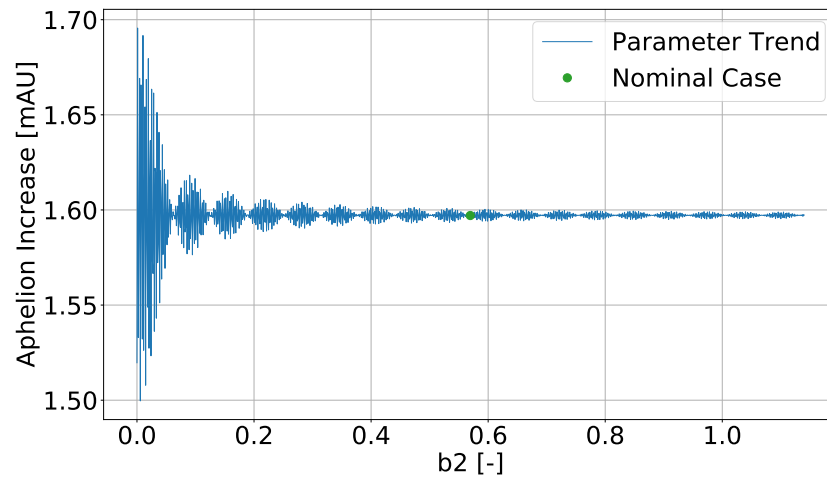

Figure 7.13: Aphelion increase while varying IMF strength estimation parameter b_2, for the InO profile type. The blue line shows the trend, while the green point shows the nominal case.

Figure 7.14 shows a simple sinusoidal periodic effect of c_1 on EDT performance, which is to be expected as it controls the phase of the long-period IMF strength oscillations, forcing the EDT to perform in either peak or trough scenarios. The overall effect on performance is negligible, with the aphelion increase only varying by around 0.02 mAU.
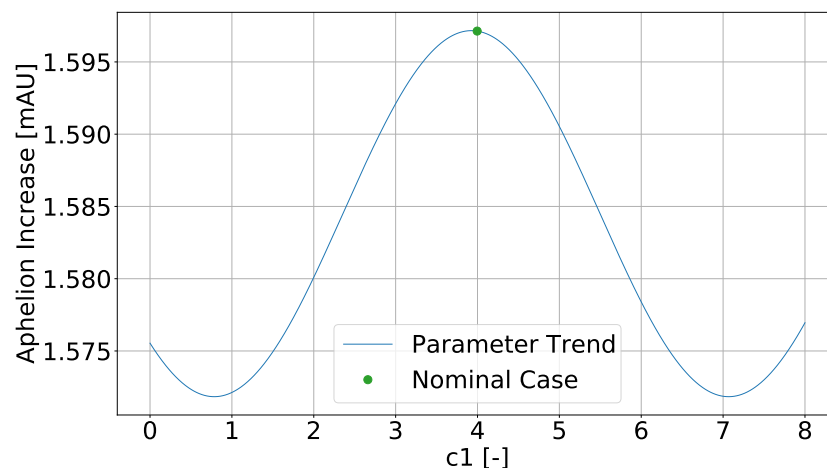

Figure 7.14: Aphelion increase while varying IMF strength estimation parameter c_1, for the InO profile type. The blue line shows the trend, while the green point shows the nominal case.

Figure 7.15 shows a similar behaviour to that of c_1, which is expected as it also controls the phase of the IMF strength variations, but for the short-period variations. However the magnitude of performance change is even weaker, being only around 0.001 mAU.
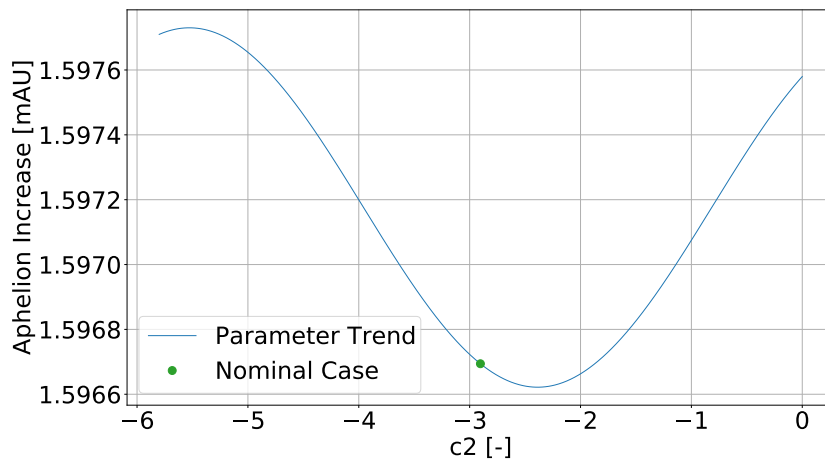

Figure 7.15: Aphelion increase while varying IMF strength estimation parameter c_2, for the InO profile type. The blue line shows the trend, while the green point shows the nominal case.

Figure 7.16 shows that increasing d also increases the EDT performance, in a near-linear fashion; this is to be expected as d controls the overall IMF strength, around which the above estimation parameters control the variation. The magnitude of the effect on performance is also the strongest observed, at around 0.75 mAU, which is also to be expected. There are several spikes at lower values of d which cause lower values of aphelion increase; the reason for these is not readily apparent, but they are uncommon and can be assumed to be anomalous.
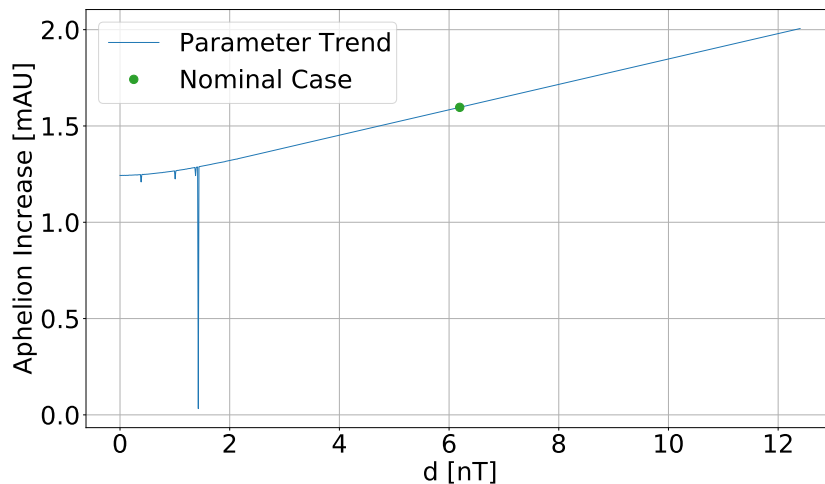

Figure 7.16: Aphelion increase while varying IMF strength estimation parameter d, for the InO profile type. The blue line shows the trend, while the green point shows the nominal case.

Figure 7.17 shows that varying AOP has no effect on overall EDT performance, which is to be expected since the InO simulation operates in a way which is heliospherically symmetric.
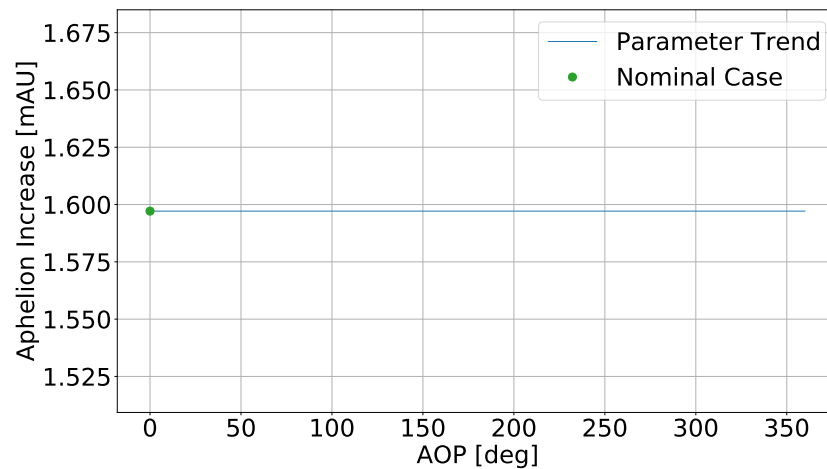

Figure 7.17: Aphelion increase while varying initial AOP, for the InO profile type. The blue line shows the trend, while the green point shows the nominal case.

These sensitivity analysis results for the InO profile are quite clear, and can be satisfyingly explained, providing a basis for the analysis of the remaining profiles.

7.3.2. SSO+ Sensitivity Results

The InO profile case, which operates exclusively in the inner Solar System, where the provided thrust is relatively high, has a clear thrust required to impact the performance in any way; by contrast the SSO+ case is relatively complex, and small factors such as computational errors can impact the results more significantly. This is evident in Figure 7.18, which shows the results of the sensitivity analysis comparing EDT performance with varying ϕ_0.
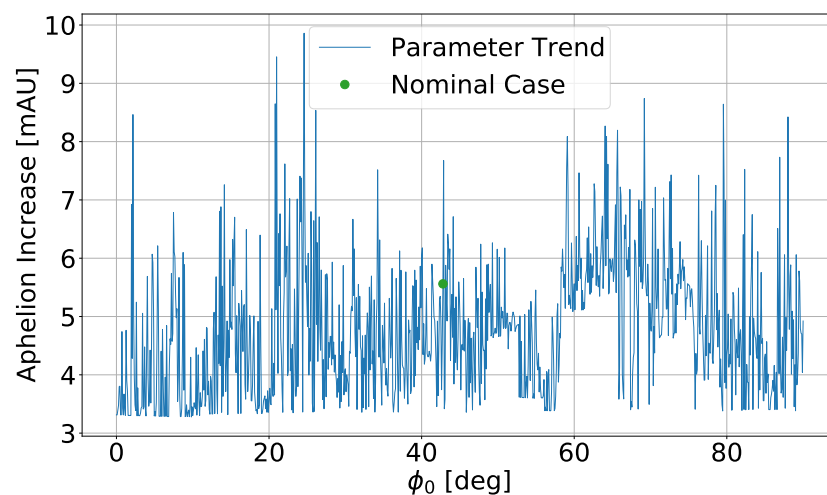

Figure 7.18: Aphelion increase while varying IMF azimuth ϕ_0, for the SSO+ profile type. The blue line shows the trend, while the green point shows the nominal case.

The noise shown here completely overshadows any potential sensitivity analysis, primarily as a result of the fact that EDT acceleration, in the current implementation, is so weak at relatively large Solar distances (i.e. beyond 1 AU). This noisy behaviour is true for all of the sensitivity parameters, and so further analysis will not be done, but the plots can be seen in Appendix A, for reference. It will be assumed however, that the good information obtained from the InO analysis can be extrapolated to also apply to the SSO+ case, in the event that EDT performance could be increased in another implementation.

7.3.3. SOKGA Sensitivity Results

Since the SOKGA profile uses two parameters to gauge performance, this is reflected by making two plots for the sensitivity analysis, one for temination TOF, and one for termination velocity, as the sensitivity parameter is varied.

Similarly to the SSO+ case, the noise from external sources, which can be seen by observing Figure 7.19, combined with the poor performance of the EDT spacecraft, means that any useful sensitivity analysis is effectively impossible. Again, the general trends of the parameters themselves can be extrapolated from the InO case, and the plots for each can be seen in Appendix A.

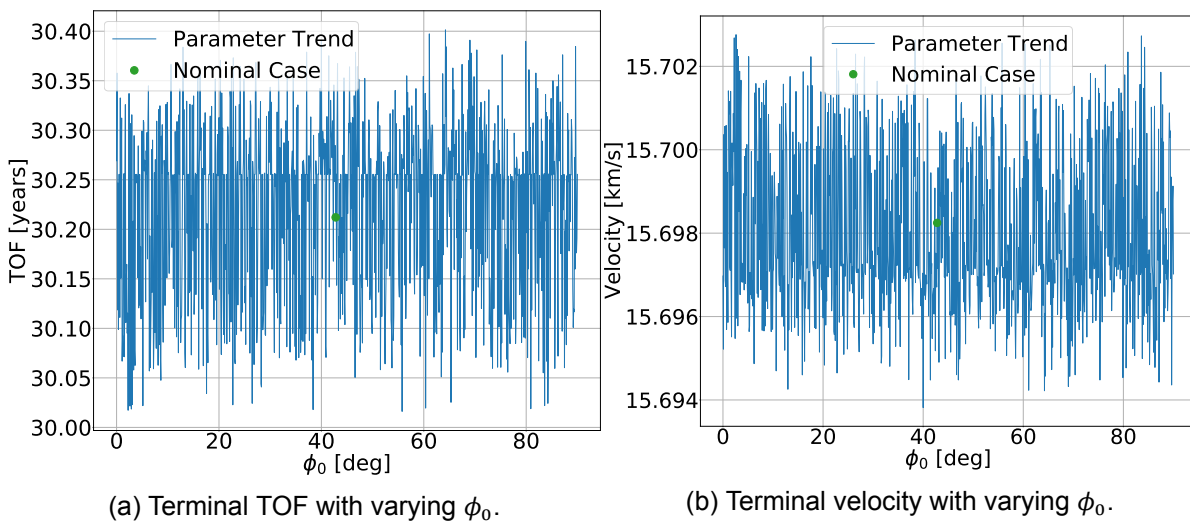(a) Terminal TOF with varying ϕ_0. (b) Terminal velocity with varying ϕ_0.

Figure 7.19: EDT performance with varying IMF azimuth ϕ_0, for the SOKGA profile type. The blue line shows the trend, while the green point shows the nominal case.

7.3.4. Mission Profile Sensitivity Analysis Results Summary

Table 7.5 summarises the results of the InO profile sensitivity analysis, qualitatively describing the bahviour and strength of each parameter on EDT performance, in the same way as Table 7.4, using acceleration as the performance metric.

Table 7.5: Sensitivity parameter effects on EDT performance, for profile parameters in the InO profile case. The table qualitatively describes both behaviour and the magnitude (ie strength) of the effect.

Parameter	Symbol	Behaviour	Strength
IMF Azimuthal Angle	ϕ_0	Non-linear decrease	Weak
IMF Strength (Estimation Parameter 1)	a_1	Linear increase	Negligible
IMF Strength (Estimation Parameter 2)	a_2	Non-linear decrease	Negligible
IMF Strength (Estimation Parameter 3)	b_1	Periodic variation	Weak
IMF Strength (Estimation Parameter 4)	b_2	Periodic variation	Negligible
IMF Strength (Estimation Parameter 5)	c_1	Periodic variation	Negligible
IMF Strength (Estimation Parameter 6)	c_2	Periodic variation	Negligible
IMF Strength (Estimation Parameter 7)	d	Near-linear increase	Strong
Argument of Perihelion	AOP	None	None

It can be clearly seen from Table 7.5 that most of the sensitivity parameters have a negligible or weak effect on the EDT performance, with the exception of IMF Strength estimation parameter d, which is only relatively stronger. This shows that for any future consideration of interplanetary EDTs, the overall IMF strength should be well known, but that the variations in Solar activity for instance, have little effect on performance, at least for a mission on the timescales assessed in this study.

8
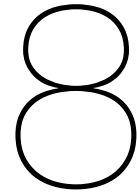
Broader Picture

There are a number of topics that were not directly considered throughout the course of this report, and so those topics are addressed here specifically. It has been quite clear that the EDT applications presented here are not very attractive, with very limited performance, and so firstly a discussion of the alternative applications of an EDT is made, along with a further discussion on some alternative technologies that may be able to facilitate the goals of this study.

Secondly, a few assumptions were implicitly made throughout the setup of this research, and so their validity will also be specifically addressed in this chapter.

8.1. Alternative EDT Applications

Although an EDT propulsion system appears to have very limited performance in the context explored in this study, the concept as a whole is not without merit. For example EDTs are very well suited to deorbit operations in LEO [22], but even remaining in the realm of planetary exploration an EDT may still find suitable ways to operate.

For example the utility of an EDT as a combined propulsion-power generation system for tours around planetary systems with strong magnetospheres such as Jupiter or Saturn is quite evident [38].

Additionally, a relatively small tether has possible application as a power generation mechanism for low-power interplanetary or interstellar probes, which would provide an alternative to Solar or nuclear power generation options. This could facilitate much smaller swarm-like spacecraft for interplanetary and interstellar exploration.

Finally, even though the transient-current method of current generation initially envisioned in this project proved to be a non-starter, research is being done into single-line power transmission methods, which could then be adapted to use in an EDT. Using single-line power transmission would allow a current to flow in one direction through the tether, completely independent of external electron collection and emission, entirely removing the EDTs need for an electron emitter, and its reliance on an ionosphere for electron collection. Additionally, no net power would be required in this configuration, if power was transmitted between for example batteries mounted on the tether ends, potentially only requiring that transmission efficiency losses must be accounted for, allowing for a very low-power propulsion method, even if the thrust would remain rather small.

8.1.1. Alternative Methods and Technologies

The limitations of an EDT propulsion system to the goals of this study - namely long-range interplanetary and interstellar travel - highlight the fact that other methods must be investigated to facilitate such missions. Fortunately there are a number of novel ideas being investigated, most notably NASA's new Interstellar Probe, being investigated by John Hopkins University Applied Physics Laboratory aims to use the new SLS launch system to provide very significant performance gains that could facilitate a conventional gravity-assist based trajectory, or even the use of Solar sails close to the Sun to provide sufficient velocity change [30].

In deep space the main problem for a spacecraft, both operationally and in propulsion systems, is power generation: the recent Juno mission was on the edge of being able to feasibly use solar panels, even at only Jupiters distance of around 5 AU, therefore Solar power would be out of the question for such missions at extreme distance of over 100 AU. One promising alternative is the use of nuclear fission reactors rated for space use [18], although many hurdles both technological and political must be overcome before such nuclear technologies could be employed.

With these considerations, one considerable advantage of using an EDT is its Technology Readiness Level or TRL; having already been flown and tested, the EDT is at a TRL of around 8, whereas nuclear power generation systems and Solar sails which operate very near the Sun are closer to a TRL of 5 or 6.

8.2. Power Supply Assumption Analysis

Throughout the analyses conducted in this study, it was assumed that an electron emitter would be able to provide sufficient current for the EDT to utilise. Fuhrhop [17] shows that a space-based electron emitter can provide currents up to around 4000 mA, with power consumption around 4000 W, this current and power consumption also scales roughly linearly meaning the nominal configuration of a 305 mA emitter would require roughly 305 W of power to operate, clearly showing that current technology supports the required emitter currents.

In addition to this however, it was also assumed that the power requirements for the tether would be modest. Since the voltage across the tether was found to be very low, in the region of 1 mV, and the tether currents are at most 1 A, this implies a power requirement in the order of magnitude of 1 mW, clearly showing that the power requirement is dominated by the electron emitter. This means the EDT power requirements are in the range of 100s of Watts, which are within the realm of using RTGs, and are therefore quite reasonable.

8.3. Tether Rotational Stability and Strength Assumptions

It has previously been mentioned that the implemented EDT spacecraft uses rotation to remain in tension and provide stability, in this section it will be briefly proven that the EDT has the strength for this to occur. According to Williams [53], a typical EDT rotates at about 8 revolutions per orbit to maintain stability, in LEO, equating to a rotational period T_t of around 675 s. According to Sanmartin [37], the average tether tension force F_t in a rotating EDT can be found using Equation 8.1, which can be easily simplified using Equations 8.2 and 8.3. In these equations ω_t, L, ρ_t, h_t, w, m_{tot} and m_t refer to the EDT angular velocity, length, mass density, tape height, tape width, total spacecraft mass, and tether mass respectively; it should be noted that h and w are used here since Sanmartin [37] assumes a tape tether, but it is simplified to be general to any tether concept.

$$F_t = \frac{\omega_t^2 L^2 \rho_t h_t w}{4}\left(\frac{m_{tot}}{m_t} - \frac{2}{3}\right) = \frac{\pi^2 L m_t}{T_t^2}\left(\frac{m_{tot}}{m_t} - \frac{2}{3}\right) \tag{8.1}$$

$$m_t = \rho_t hwL \tag{8.2}$$

$$\omega_t = \frac{2\pi}{T_t} \tag{8.3}$$

Using the above equations using the nominal EDT case outlined in Chapter 5, the average tension in the tether is found to be F_t = 11.65 N, which equates to a tensile stress of around 74 kPa. This value is well below the tensile strength of either copper or aluminium, at around 210 MPa and 90 MPa respectively [51], and therefore the assumption that the tether can handle this stress is a valid one.

9

Conclusions and Recommendations

As efforts to understand space and the wider universe continue to advance, it is often necessary for spacecraft to be sent to further reaches of the Solar System. With current technology, it has been found that the feasibility of long-term adaptable exploration missions at the far reaches of the Solar System and beyond is limited, and so a novel propulsion system taking advantage of the interplanetary magnetic field (IMF) or even the interstellar magnetic field (ISMF) is explored: the electrodynamic tether (EDT).

In order to explore these possibilities, the following research question was proposed:

Investigate the feasibility of electrodynamic space tethers as a means of propulsion applied to possible future interplanetary and/or interstellar missions; also assess the viability of a transient-current solution for the electrodynamic tether.

Which is made up of the following subquestions:

- *What level of performance can realistically be achieved by an EDT in interplanetary and/or interstellar space?*

- *Which regions of space would and EDT spacecraft be suited to operating, and on what kinds of missions?*

- *What design concepts of an EDT are best suited to the above mentioned operating regions?*

- *How competitive is the EDT as a means of propulsion when compared against both conventional chemical propulsion, and other alternative propulsion means?*

This chapter aims to discuss the obtained results, thereby answering these questions, as well as recommendations for future work and a more general discussion of the applications of EDTs to space travel.

9.1. Conclusions

To answer the previously described research questions, a simulation environment was established, using the Tudat simulation toolbox as its base; into which a number of additional custom environment models were implemented, as well as a simple guidance logic, allowing the system to raise or lower its orbit, depending on the chosen mission profile.

Three different mission profiles were then defined, namely Simple-Straight-Out (SSO) which evolved during development into SSO+, Inner Solar System Out (InO), and SOKGA (Straight-Out with Kickstage and Gravity Assist).

The performance analysis was then split into two stages: firstly the EDT configuration parameters were assessed, using a relatively short simulation period of 1 year, in a simple circular orbit at 1 AU, with any orbital perturbations removed. This first stage established a baseline EDT spacecraft, which would then be taken forward for use in the second stage, the mission profile assessment. This second stage analysis considered how each of the described mission profiles could be varied in order to give an idea for the best performance achievable given the baseline spacecraft.

The first stage of analysis concluded that a 1 km tether with a mass of 1412 kg would be used as the baseline, using a bare-tether thrust generation concept with a dedicated electron emitter operating at a current of 305 mA. It should be noted however that this baseline spacecraft was routinely limited by the implementation of the current generation model, where it was necessary to restrict some parameters such as length or emitter current, in order to prevent the assumptions of that implementation from being violated. This first stage also acted as a sort of sensitivity analysis for some of these EDT configuration parameters, showing that the most influential design choices are the tether diameter, emitter current, and number of primary lines (for a Hoytether implementation), with other parameters such as length having surprisingly little effect on the performance; the performance was quantified by the achieved acceleration which was around 0.9 nm/s^2.

The second stage analysis employed the Differential Evolution (DE) optimisation scheme used by PaGMO and PyGMO for the SSO+ and InO mission profiles, using the maximum achieved change in aphelion over a simulation period of 100 years as the optimisation goal. The results of these analyses for the SSO+ and InO profiles clearly highlighted the severe limitations of an EDT propulsion system in its present implementation, providing an aphelion change of only 0.01 AU and 0.002 AU respectively. These results were shown to be insensitive to the launch date.

For the SOKGA case no optimisation scheme was employed, as this was already done in the preliminary analysis. To determine EDT performance, the time of flight (TOF) to reach 100 AU (i.e. the edge of the Solar system), and the velocity at this point, were used. The results showed that the most optimal trajectory employed a Jupiter gravity assist in 2043, and similarly to the SSO+ and InO results, that the limitations of the EDT are clear: without an EDT the spacecraft terminated with a TOF of 30.26 years and velocity 15.697 km/s, while with an EDT the termination TOF is 30.14 years, and velocity 15.7 km/s. This represents an improved TOF to 100 AU of only around 45 days over a decades long journey, and only a 3 m/s improvement in velocity over a ballistic trajectory.

A sensitivity analysis was also conducted for some additional configuration parameters, as well as mission profile parameters. The analysis showed that there is a strong relationship between performance and both secondary tether diameter as the tether shell material density, highlighting areas for possible improvements. There is also a strong relationship between performance and overall IMF strength, while other environment and profile parameters have little or no effect.

To specifically answer the research questions put forward:

- In the present implementation, EDT performance is very poor, with accelerations in the nm/s^2 range for interplanetary regions. The interstellar region was not assessed due to time constraints.

- None of the considered mission profiles provided a suitable operational region for an EDT propulsion system, with the present implementation and technology.

- The transient-current generation model is currently not viable, so a bare-tether solution should be the design concept of choice.

- The EDT in its present implementation is not competitive with alternative means of propulsion, providing velocity changes in the m/s range over decades of mission time.

With these subquestions answered, the overall research statement can also be addressed: the usage of an EDT in interplanetary space using the methods outlined in this research are severely limited, and the proposed transient-current solution is not viable.

9.2. Recommendations

This research has provided additional knowledge to the idea of using an EDT as a means of deep space propulsion, however many lessons have been learned in the process, and the following recommendations can be made for future work:

- As previously mentioned, it was found during development that the chosen analytic method used to model the current generation proved to be far from ideal for a deep space EDT application, with its assumptions regularly restricting design. Therefore any future analysis should utilise a more robust current-generation technique, potentially allowing for better performance and a more feasible design.

- It was found that the transient-current solution originally envisioned is impossible with current technology. However, single-line power transmission methods, could provide incredible performance gains for an EDT system, and so if developed further they should be considered for an EDT application.

- Due to time constraints, a proper model of required power draw of the EDT was not considered, and was simply assumed to be reasonable. Any further EDT studies that might show EDT feasibility should also consider this in their analysis.

- The sensitivity analysis showed considerable performance gains could be achieved with materials with more favourable properties than aluminium and copper used in this study; therefore in further study new materials could be assessed for EDT applications that are conductive, but with densities similar to carbon fibre, for example carbon nanotubes.

- The application of an EDT to interstellar missions could provide a viable use-case for an EDT, and so should be investigated further. Even in the case that the EDT does not provide useful for propulsion, a mission could use an EDT to generate power in the interstellar medium, providing a potential alternative to nuclear options such as RTGs.

- It was assumed that the Solar ionosphere would provide sufficient electron density for the proper operation of a bare-tether EDT, in future studies this should be more rigorously confirmed.

A
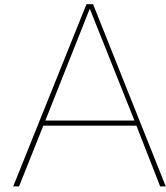
Appendix A - Additional Sensitivity Analysis Plots

As described in Chapter 7, for the SSO+ and SOKGA trajectories, the sensitivity analysis data was quite heavily distorted, making their utility limited in the report itself, however they are shown here for reference. Firs the SSO+ profile plots are shown, followed by the SOKGA profile plots.
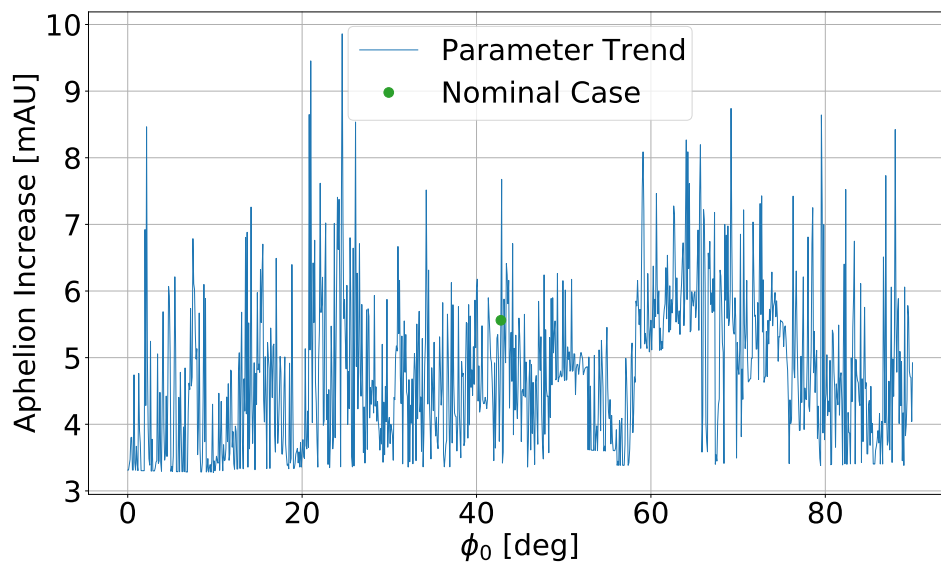
A.1. SSO+ Sensitivity Analsyis Plots

Figure A.1: Aphelion increase while varying IMF azimuth ϕ_0, for the SSO+ profile type. The blue line shows the trend, while the green point shows the nominal case.
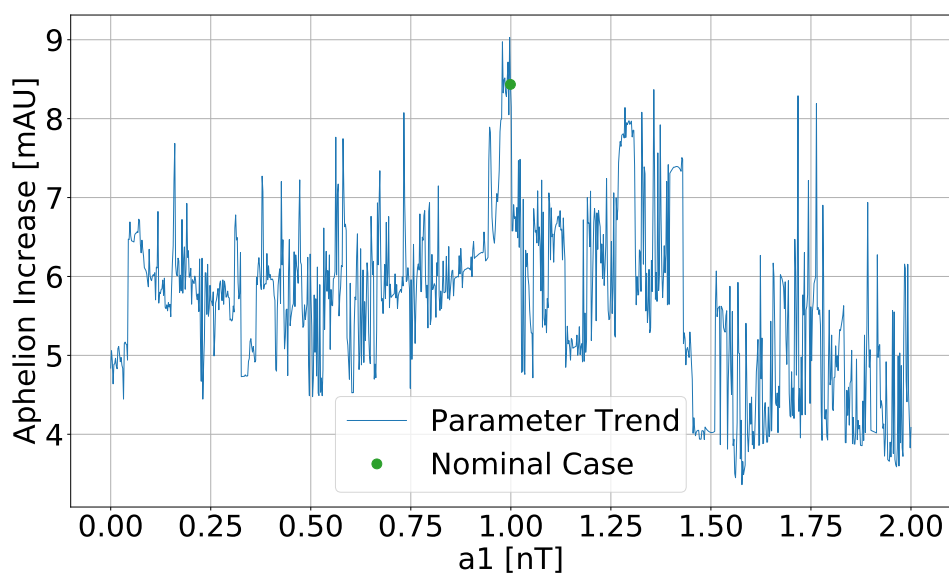
Figure A.2: Aphelion increase while varying IMF strength estimation parameter a_1, for the SSO+ profile type. The blue line shows the trend, while the green point shows the nominal case.
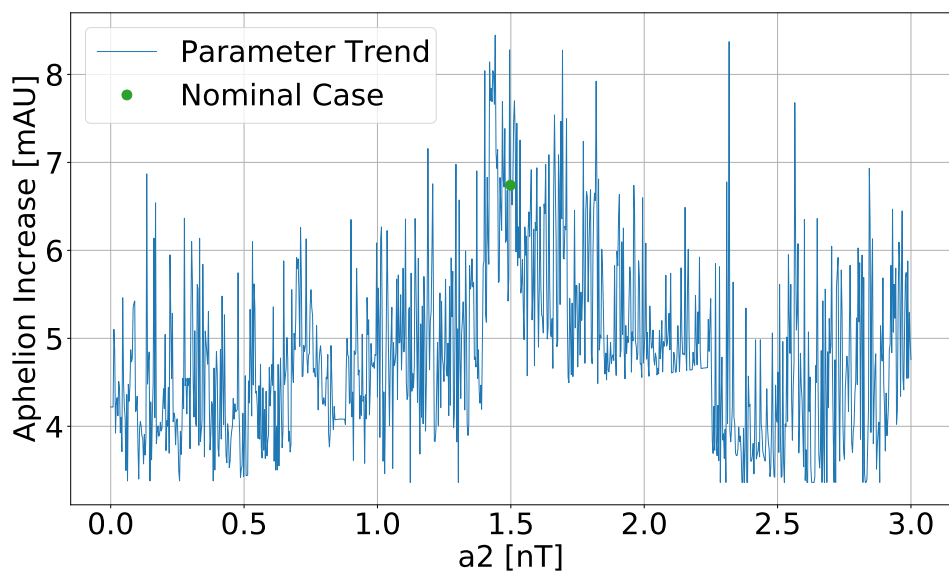

Figure A.3: Aphelion increase while varying IMF strength estimation parameter a_2, for the SSO+ profile type. The blue line shows the trend, while the green point shows the nominal case.

Figure A.4: Aphelion increase while varying IMF strength estimation parameter b_1, for the SSO+ profile type. The blue line shows the trend, while the green point shows the nominal case.

Figure A.5: Aphelion increase while varying IMF strength estimation parameter b_2, for the SSO+ profile type. The blue line shows the trend, while the green point shows the nominal case.
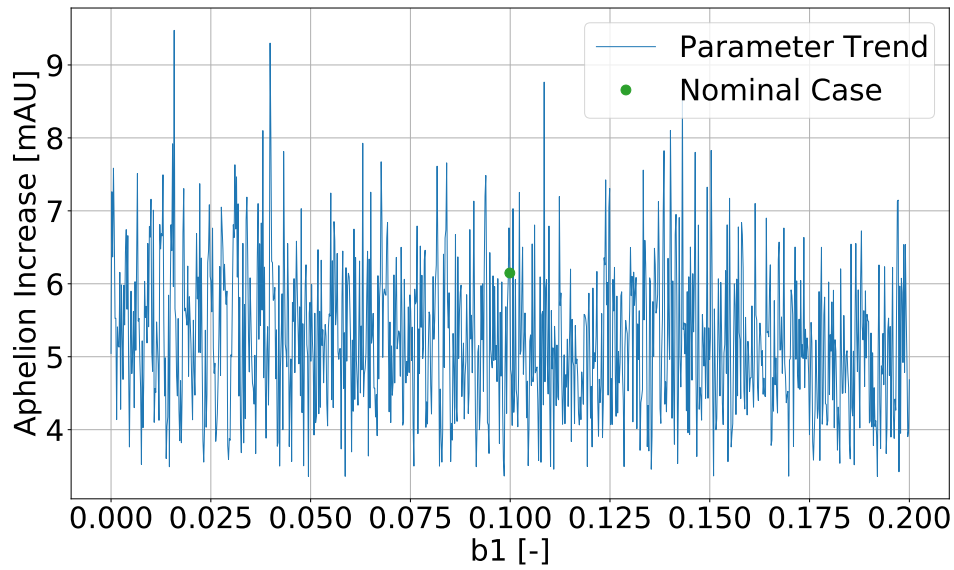
Figure A.6: Aphelion increase while varying IMF strength estimation parameter c_1, for the SSO+ profile type. The blue line shows the trend, while the green point shows the nominal case.
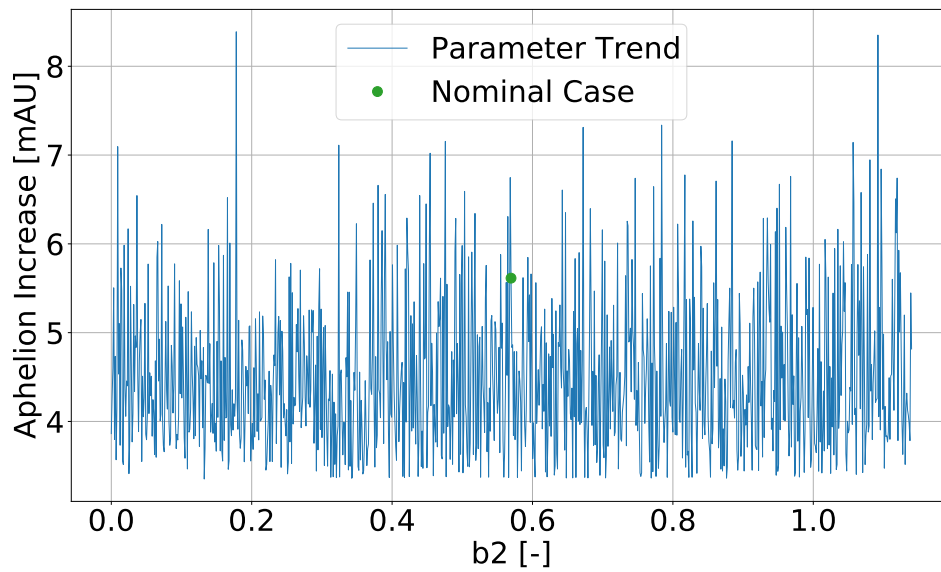

Figure A.7: Aphelion increase while varying IMF strength estimation parameter c_2, for the SSO+ profile type. The blue line shows the trend, while the green point shows the nominal case.

Figure A.8: Aphelion increase while varying IMF strength estimation parameter d, for the SSO+ profile type. The blue line shows the trend, while the green point shows the nominal case.

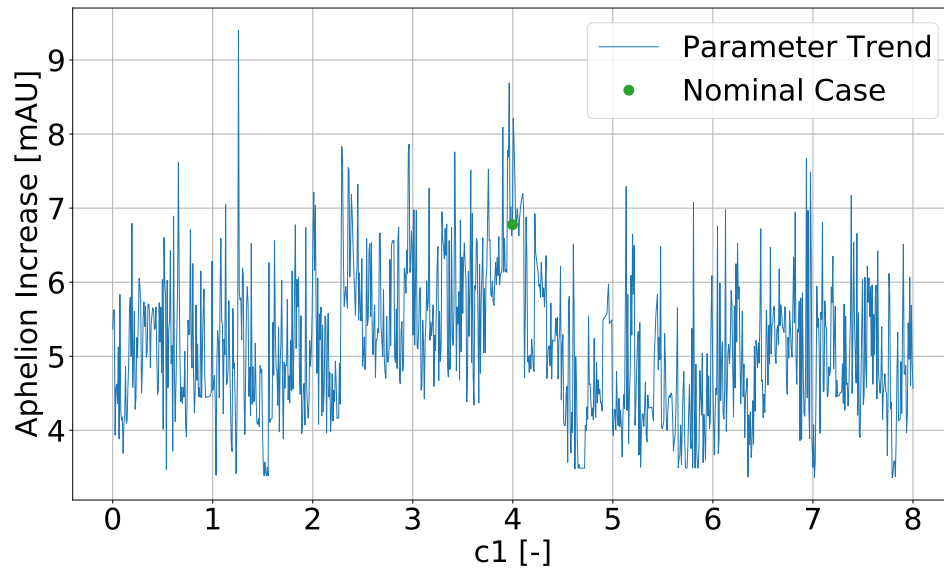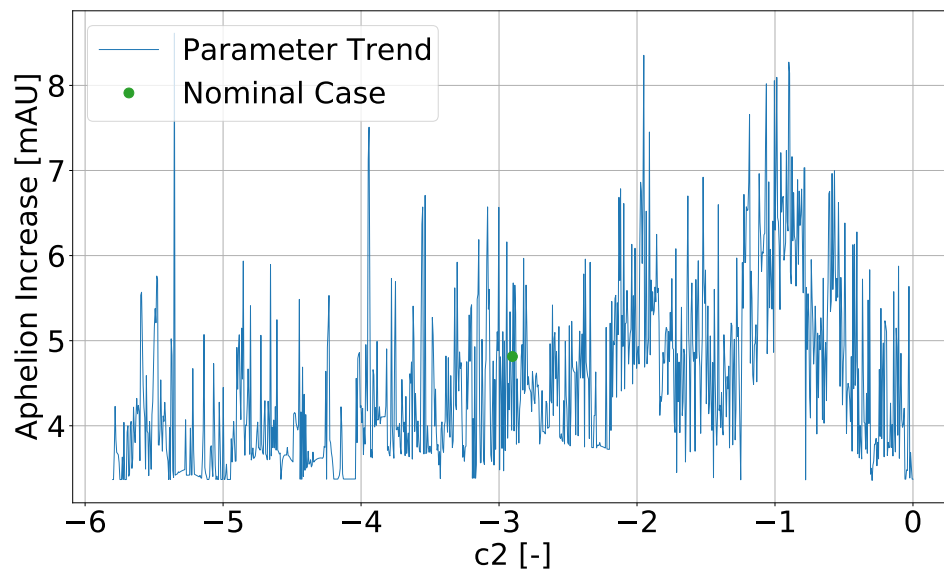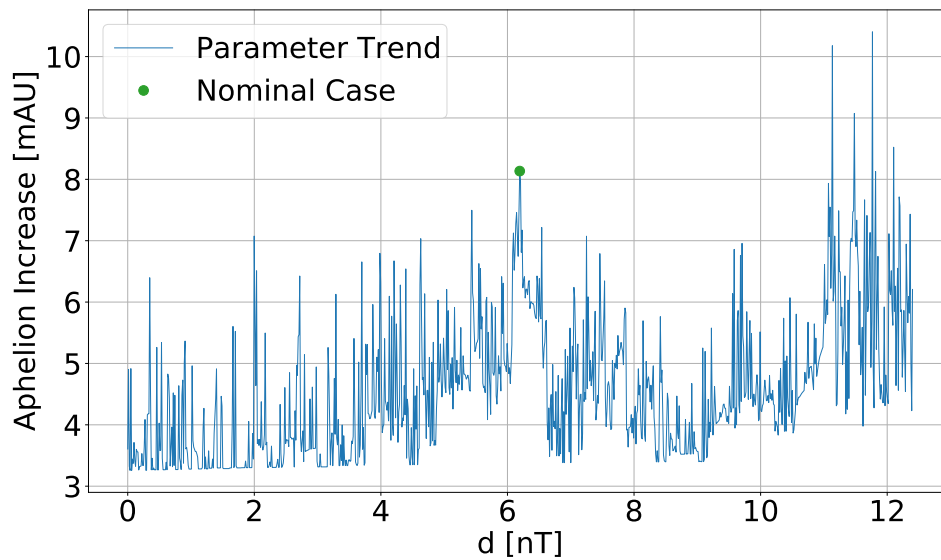

Figure A.9: Aphelion increase while varying initial AOP, for the SSO+ profile type. The blue line shows the trend, while the green point shows the nominal case.

A.2. SOKGA Sensitivity Analysis Plots

(a) Terminal TOF with varying ϕ_0.

(b) Terminal velocity with varying ϕ_0.
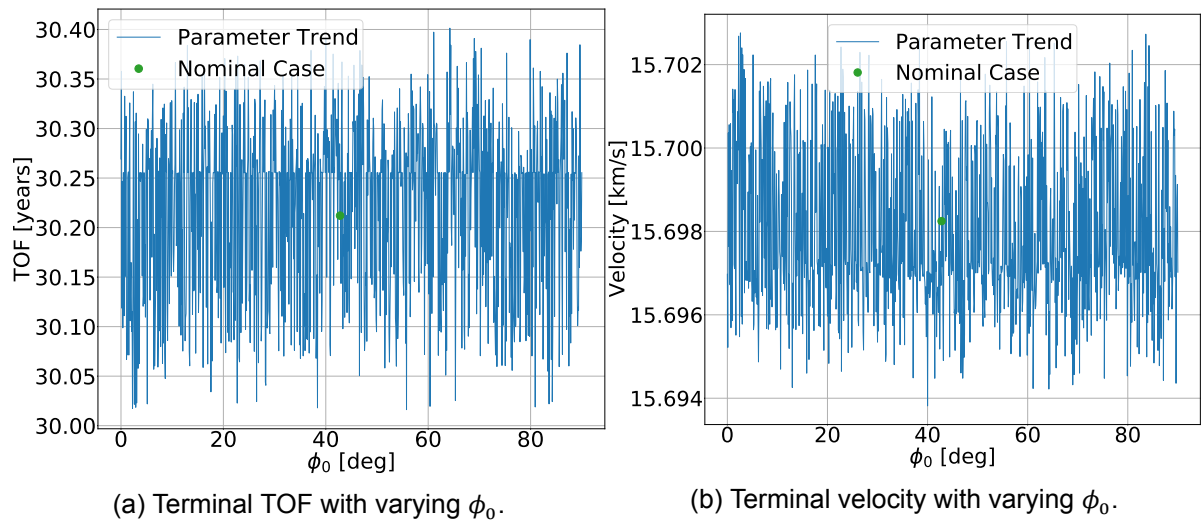
Figure A.10: EDT performance with varying IMF azimuth ϕ_0, for the SOKGA profile type. The blue line shows the trend, while the green point shows the nominal case.

(a) Terminal TOF with varying a_1.

(b) Terminal velocity with varying a_1.

Figure A.11: EDT performance with varying IMF strength estimation parameter a_1, for the SOKGA profile type. The blue line shows the trend, while the green point shows the nominal case.

(a) Terminal TOF with varying a_2.

(b) Terminal velocity with varying a_2.

Figure A.12: EDT performance with varying IMF strength estimation parameter a_2, for the SOKGA profile type. The blue line shows the trend, while the green point shows the nominal case.

(a) Terminal TOF with varying b_1.

(b) Terminal velocity with varying b_1.
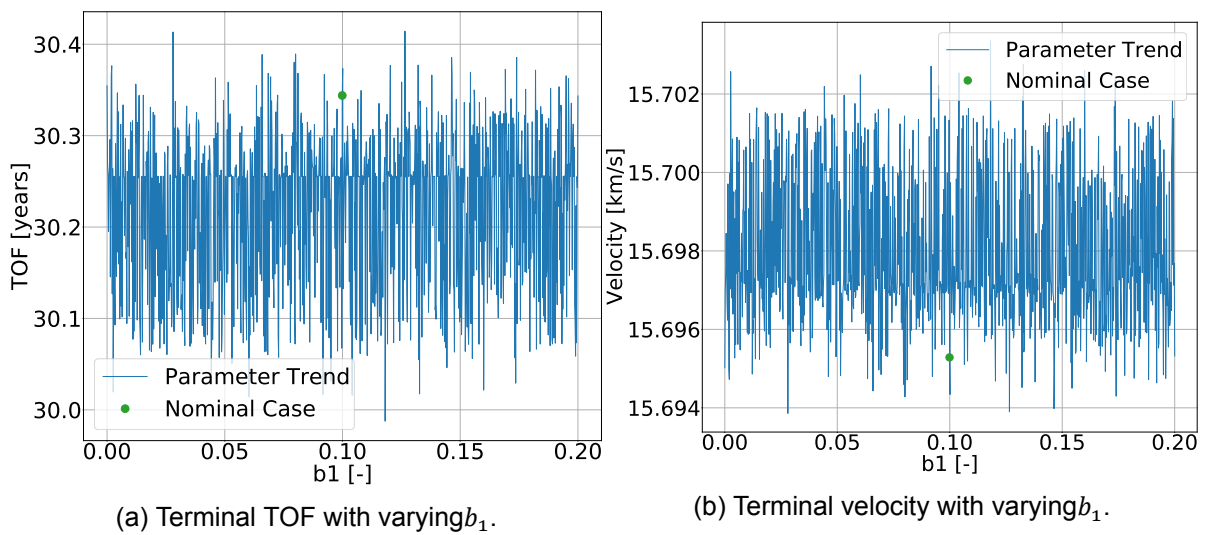
Figure A.13: EDT performance with varying IMF strength estimation parameter b_1, for the SOKGA profile type. The blue line shows the trend, while the green point shows the nominal case.
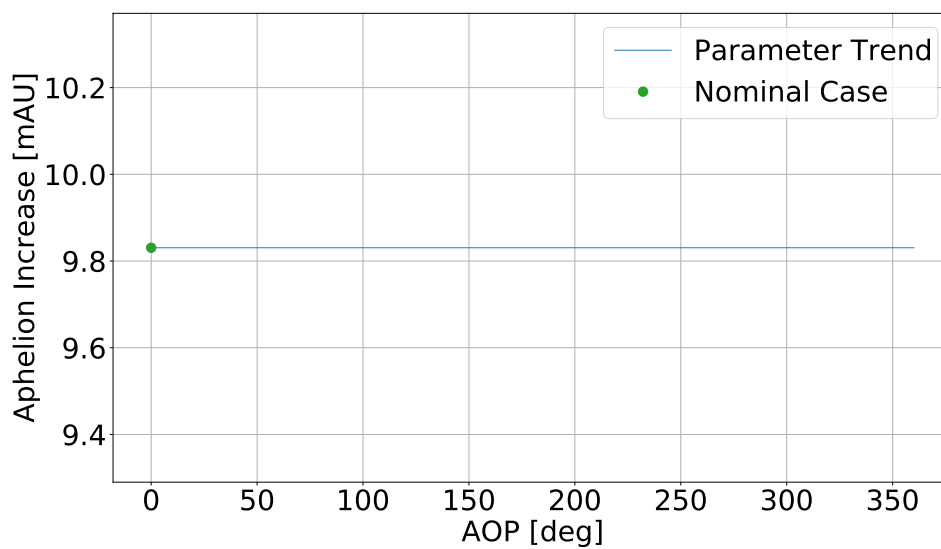
(a) Terminal TOF with varying b_2.

(b) Terminal velocity with varying b_2.
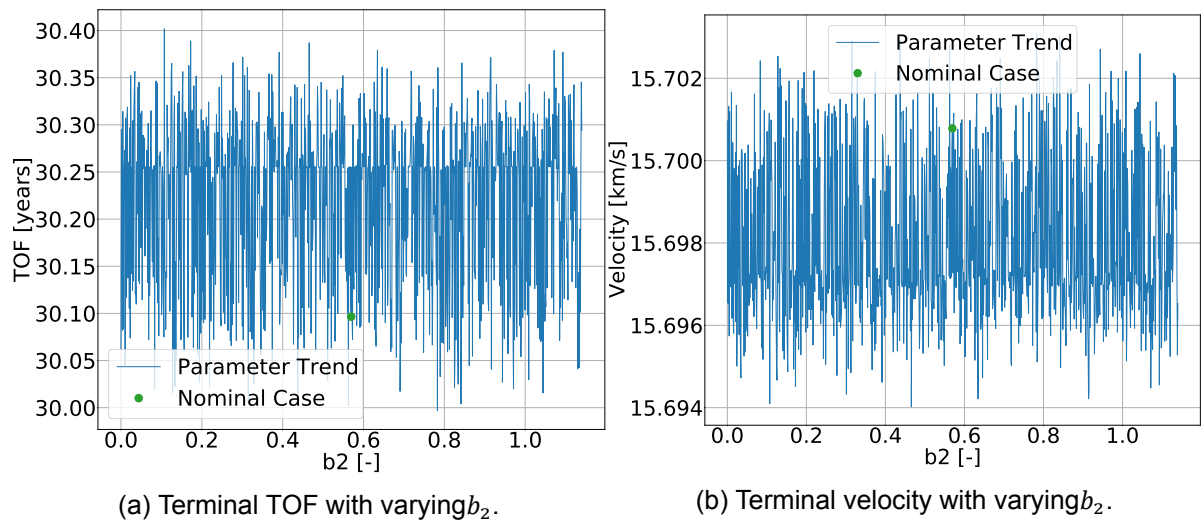
Figure A.14: EDT performance with varying IMF strength estimation parameter b_2, for the SOKGA profile type. The blue line shows the trend, while the green point shows the nominal case.

(a) Terminal TOF with varying c_1.

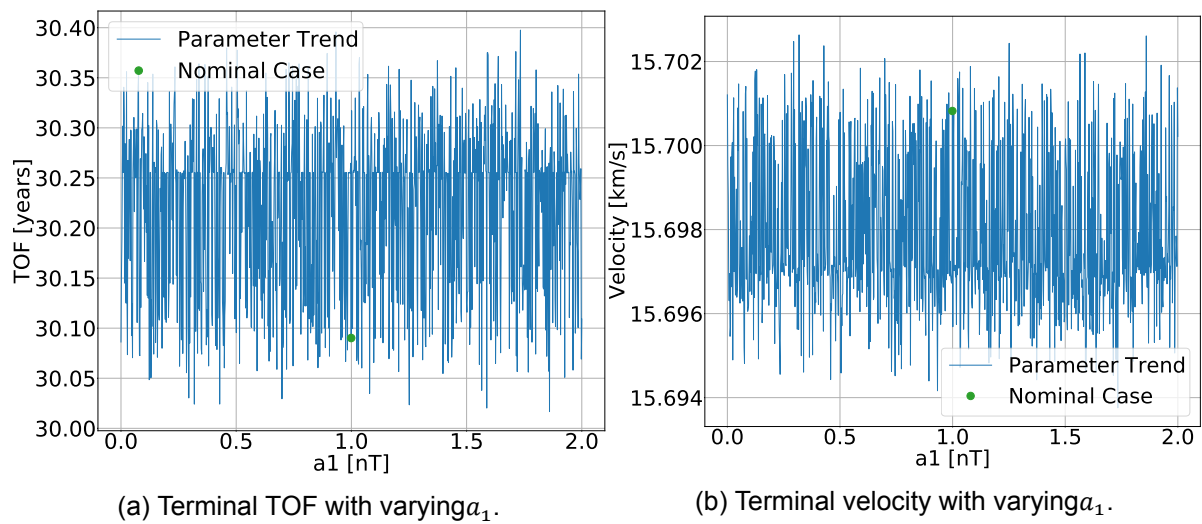(b) Terminal velocity with varying c_1.

Figure A.15: EDT performance with varying IMF strength estimation parameter c_1, for the SOKGA profile type. The blue line shows the trend, while the green point shows the nominal case.

(a) Terminal TOF with varying c_2.

(b) Terminal velocity with varying c_2.

Figure A.16: EDT performance with varying IMF strength estimation parameter c_2, for the SOKGA profile type. The blue line shows the trend, while the green point shows the nominal case.
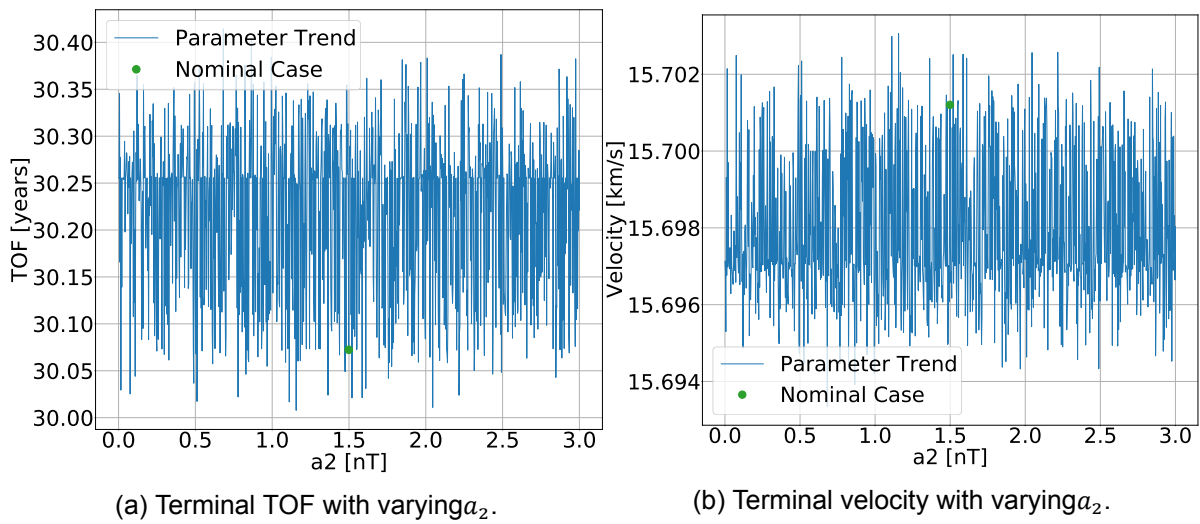

(a) Terminal TOF with varying d.

(b) Terminal velocity with varying d.

Figure A.17: EDT performance with varying IMF strength estimation parameter d, for the SOKGA profile type. The blue line shows the trend, while the green point shows the nominal case.
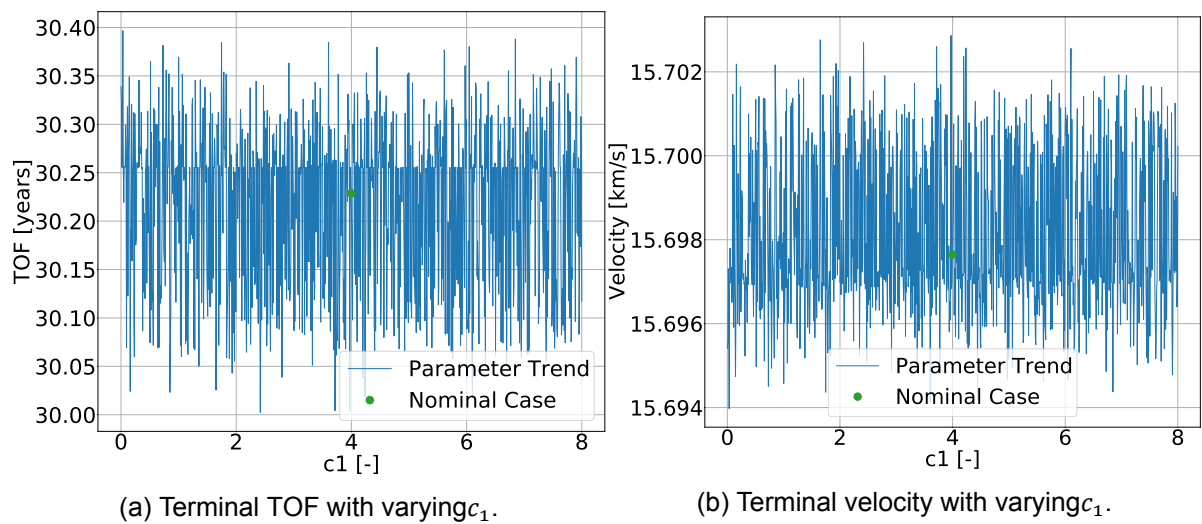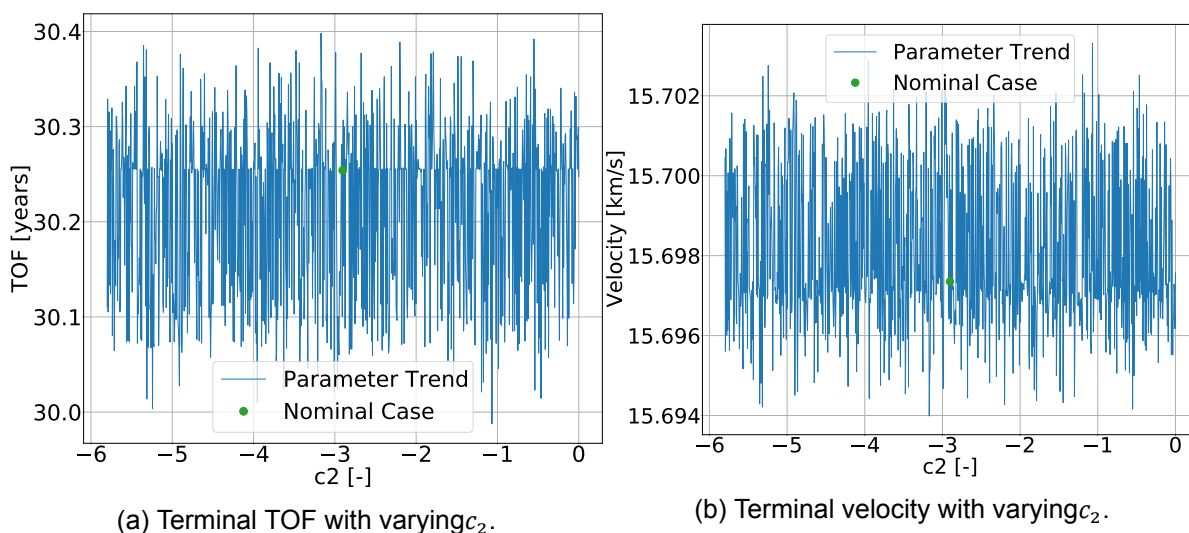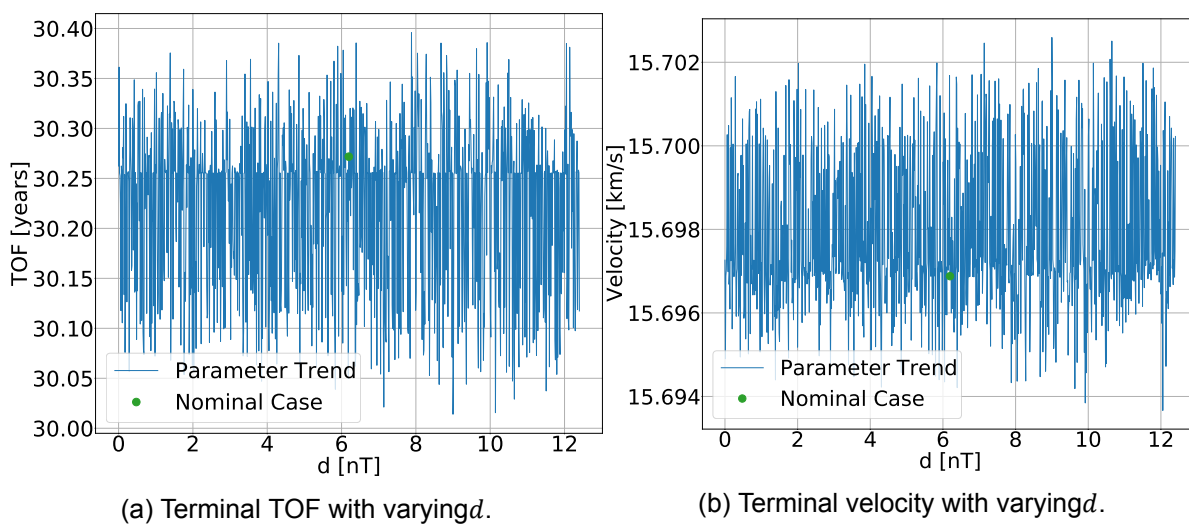
B

Appendix B

Throughout the report various simulations with different settings are used. In order to not continually repeat various common settings, Table B.1 lists all the default simulation settings, and wherever a simulation differs from this, the discrepancies are listed in the report itself; the table lists the simulation parameter name, its symbol and unit (where relevant) and the default value.

Table B.1: Default Simulation Environment Settings.

Parameter	Symbol	Unit	Value
Third Body Perturbations			
Spice Kernel	-	-	de430
Include Mercury 3rd Body	-	-	0
Include Venus 3rd Body	-	-	0
Include Earth 3rd Body	-	-	0
Inlcude Mars 3rd Body	-	-	0
Include Jupiter 3rd Body	-	-	0
Include Saturn 3rd Body	-	-	0
Include Uranus 3rd Body	-	-	0
Include Neptune 3rd Body	-	-	0
Magnetic Field Configurations			
Phi0	ϕ_0	deg	42.748
B0 Estimation Parameter 1	a1	nT	1
B0 Estimation Parameter 2	a2	nT	1.5
B0 Estimation Parameter 3	b1	-	0.1
B0 Estimation Parameter 4	b2	-	0.57
B0 Estimation Parameter 5	c1	-	4
B0 Estimation Parameter 6	c2	-	-2.9
B0 Estimation Parameter 7	d	nT	6.2
ISMF Transition Distance	R_{ISMF}	AU	100
ISMF Strength	$|\mathbf{B}_\infty|$	nT	0.293
Interstellarmagfield Longitudeinf Deg	λ_∞	deg	227.28
Interstellarmagfield Latitudeinf Deg	β_∞	deg	34.62
Impose Magnetic Field	-	-	FALSE
Imposed Magnetic Field x	$B_{x,imp}$	nT	10
Imposed Magnetic Field y	$B_{y,imp}$	nT	10

Imposed Magnetic Field z	$B_{z,imp}$	nT	10
Guidance Configurations			
Thrust Magnitude Config	-	-	Nominal
Thrust Direction Config	-	-	Nominal Prograde
Minimum Perihelion	Pe_{min}	AU	0.1
Initial Timestep	-	years	1
Integrator Type	-	-	RK87DP
Minimum Stepsize	-	s	1.00E-20
Maximum Stepsize	-	s	10^{-20}
Relative Error Tolerance	-	-	10^{-5}
Absolute Error Tolerance	-	-	10^{-5}
Termination Type	-	-	Nominal TOF Termination
TOF Termination	-	years	5
Date Termination	-	calendar year	2200
Proximity Termination Body	-	-	Jupiter
Proximity Termination Value	-	AU	0.1
Distance Termination Value	-	AU	10
Initial State Coordinate Type	-	-	Keplerian
Semi-major Axis	a	AU	1
Eccentricity	e	-	0
Inclination	i	deg	0
Argument of Perihelion	AOP	deg	0
Right Ascension of Ascending Node	RAAN	deg	0
True Anomaly	TA	deg	225
Initial x	x_1	AU	0
Initial y	x_2	AU	0
Initial z	x_3	AU	0
Initial x Velocity	v_1	km/s	0
Initial y Velocity	v_2	km/s	0
Initial z Velocity	v_3	km/s	0
EDT Configurations			
EDT Configuration Type	-	-	CHB
Tether Length	L	km	1
(Primary) Line Diameter	D	mm	10
(Primary) Area Ratio	k_A	-	1
Electron Emitter Current	I_C	mA	305
Rotation Coefficient (Thrust)	k_{Trot}	-	0.8
Secondary Line Diameter	D_s	mm	10
Secondary Line Area Ratio	$k_{A,s}$	-	1
Number of Primary Lines	n	-	2
Primary Line Segment Ratio	k_{lp}	-	0.5
Slack Coefficient	k_s	-	1.005
Primary Line Separation Ratio	k_a	-	100
Rotation Coefficient (SRP)	k_{rot}	-	0.75
SRP Configurations			
Use SRP	-	-	TRUE
Endmass Area 1	A_1	m^2	1.2
Endmass Area 2	A_2	m^2	1.2
Endmass Radiation Coefficient	$k_{rad,end}$	?	1.5

Tether Radiation Coefficient	$k_{rad,teth}$	?	1.5
Occultation Coefficient	k_{occ}	-	0.7
Endmass Mass 1	m_1	kg	50
Endmass Mass 2	m_2	kg	50

Bibliography

[1] Scipy Documentation. URL `https://docs.scipy.org/doc/scipy/reference/`. [Accessed on: 2021-06-20].

[2] Charles Acton, Nathaniel Bachman, Boris Semenov, and Edward Wright. A look towards the future in the handling of space science mission geometry. *Planetary and Space Science*, 150:9–12, jan 2018. ISSN 00320633. doi: 10.1016/j.pss.2017.02.013.

[3] Wolfram Alpha. Parker Spiral Example. URL `https://demonstrations.wolfram.com/TheInterplanetaryMagneticFieldParkerSpiral/`. [Accessed on: 2021-06-20].

[4] Vladimir S. Aslanov and Alexander S. Ledkov. *Dynamics of tethered satellite systems*. Woodhead Publishing Limited, 2012. ISBN 978-0-85709-156-7. doi: 10.1533/9780857096005. URL `http://www.sciencedirect.com/science/book/9780857091567`.

[5] K. W. Behannon, M. H. Acuna, L. F. Burlaga, R. P. Lepping, N. F. Ness, and F. M. Neubauer. Magnetic field experiment for Voyagers 1 and 2. *Space Science Reviews*, 21 (3):235–257, 1977. ISSN 00386308. doi: 10.1007/BF00211541.

[6] Sven Bilen, C. Johnson, Bruce Wiegmann, Leslie Alexander, Brian Gilchrist, Robert Hoyt, Craig Elder, Keith Fuhrhop, Michael Scadera, and Nobie Stone. The PROPEL Electrodynamic Tether Demonstration Mission. In *AIAA SPACE 2012 Conference & Exposition*, Reston, Virigina, sep 2012. American Institute of Aeronautics and Astronautics. ISBN 978-1-60086-940-2. doi: 10.2514/6.2012-5293. URL `http://arc.aiaa.org/doi/10.2514/6.2012-5293https://arc.aiaa.org/doi/10.2514/6.2012-5293`.

[7] Francesco Biscani and Izzo Dario. Pygmo - MOEAD, . URL `https://esa.github.io/pygmo2/tutorials/moo{_}moead.html`. [Accessed on: 2020-06-20].

[8] Francesco Biscani and Izzo Dario. Pagmo Documentation - Algorithms, . URL `https://esa.github.io/pagmo2/docs/cpp/algorithms/de.html`. [Accessed on: 2021-06-21].

[9] Joseph E. Borovsky. On the variations of the solar wind magnetic field about the Parker spiral direction. *Journal of Geophysical Research: Space Physics*, 115(A9):n/a–n/a, sep 2010. ISSN 01480227. doi: 10.1029/2009JA015040. URL `http://doi.wiley.com/10.1029/2009JA015040`.

[10] L. F. Burlaga. Heliospheric magnetic field strength and polarity from 1 to 81 AU during the ascending phase of solar cycle 23. *Journal of Geophysical Research*, 107(A11):1410, 2002. ISSN 0148-0227. doi: 10.1029/2001JA009217. URL `http://doi.wiley.com/10.1029/2001JA009217`.

[11] Ben Burress. NASA's 40-year Voyage Continues, 2017. URL `https://www.kqed.org/science/1914502/nasas-40-year-voyage-continues`. [Accessed on: 2021-06-20].

[12] Yi Chen, Rui Huang, Xianlin Ren, Liping He, and Ye He. History of the Tether Concept and Tether Missions: A Review. *ISRN Astronomy and Astrophysics*, 2013(May 2015): 1–7, 2013. ISSN 2090-4746. doi: 10.1155/2013/502973. URL `https://www.hindawi.com/archive/2013/502973/`.

[13] Howard D Curtis. *Preface BT - Orbital Mechanics for Engineering Students (Third Edition)*. 2014. ISBN 978-0-08-097747-8. doi: http://dx.doi.org/10.1016/B978-0-08-097747-8.05001-5. URL `http://www.sciencedirect.com/science/article/pii/B9780080977478050015`.

[14] TU Delft. Tudat Documentation - Home. URL `https://tudat.tudelft.nl/`. [Accessed on: 2021-06-20].

[15] S. E. S. Ferreira, M. S. Potgieter, and K. Scherer. Modeling of the Heliospheric Interface, Magnetic Field, and Cosmic Ray Transport. *The Astrophysical Journal*, 659 (2):1777–1783, apr 2007. ISSN 0004-637X. doi: 10.1086/512848. URL `https://iopscience.iop.org/article/10.1086/512848`.

[16] Robert Forward and Robert Hoyt. Failsafe multiline Hoytether lifetimes. In *31st Joint Propulsion Conference and Exhibit*, Reston, Virigina, jul 1995. American Institute of Aeronautics and Astronautics. ISBN 9780000000002. doi: 10.2514/6.1995-2890. URL `http://arc.aiaa.org/doi/10.2514/6.1995-2890`.

[17] Keith R. Fuhrhop, Dave Morris, and Brian E. Gilchrist. Electron emission for electrodynamic tether systems in space. *40th AIAA/ASME/SAE/ASEE Joint Propulsion Conference and Exhibit*, (July 2014), 2004. doi: 10.2514/6.2004-3495.

[18] Marc A. Gibson, Steven R. Oleson, David I. Poston, and Patrick McClure. NASA's Kilopower reactor development and the path to higher power missions. In *2017 IEEE Aerospace Conference*, volume 2017-June, pages 1–14. IEEE, mar 2017. ISBN 978-1-5090-1613-6. doi: 10.1109/AERO.2017.7943946. URL `http://ieeexplore.ieee.org/document/7943946/`.

[19] Mario D. Grossi. Plasma Motor Generator (PMG) electrodynamic tether experiment. Technical report, NASA, 1995. URL `https://ntrs.nasa.gov/search.jsp?R=19960002041`.

[20] Lars Hoving. Optimisation Strategies for Galilean Moon Tours, MSc Thesis, TU Delft, 2015.

[21] Robert Hoyt, Jeffrey Slostad, and Robert Twiggs. The multi-application survivable tether (MAST) experiment. In *39th AIAA/ASME/SAE/ASEE Joint Propulsion Conference and Exhibit*, pages 2–8, Reston, Virigina, jul 2003. American Institute of Aeronautics and Astronautics. ISBN 9781624100987. doi: 10.2514/6.2003-5219. URL `http://arc.aiaa.org/doi/10.2514/6.2003-5219`.

[22] Les Johnson and Melody Herrmann. International Space Station electrodynamic tether reboost. In *AIP Conference Proceedings*, number July 1998, pages 490–495. AIP, 1999. doi: 10.1063/1.57614. URL `http://aip.scitation.org/doi/abs/10.1063/1.57614`.

[23] J.H. King and N.E. Papitashvili. Solar wind spatial scales in and comparisons of hourly Wind and ACE plasma and magnetic field data, 2005. URL `https://omniweb.gsfc.nasa.gov/ow.html`.

[24] Greg Kopp and Judith L. Lean. A new, lower value of total solar irradiance: Evidence and climate significance. *Geophysical Research Letters*, 38(1):n/a–n/a, jan 2011. ISSN 00948276. doi: 10.1029/2010GL045777. URL http://doi.wiley.com/10.1029/2010GL045777.

[25] Michiel Kruijff. Tethers in Space, A propellantless propulsion in-orbit demonstration. *Uitgeverij BOXPress, Oisterwijk*, (November), 2011. URL https://www.researchgate.net/publication/228107637{%}0ATethers.

[26] Christoph Lhotka and Yasuhito Narita. Kinematic models of the interplanetary magnetic field. *Annales Geophysicae*, 37(3):299–314, may 2019. ISSN 1432-0576. doi: 10.5194/angeo-37-299-2019. URL https://angeo.copernicus.org/articles/37/299/2019/.

[27] E C Lorenzini and M L Cosmo. *Tethers in space handbook*. National Aeronautics and Space Administration, 3rd edition, 1997.

[28] A. Lyngvi, P. Falkner, and A. Peacock. The interstellar heliopause probe technology reference study. *Advances in Space Research*, 35(12):2073–2077, jan 2005. ISSN 02731177. doi: 10.1016/j.asr.2005.07.083. URL https://linkinghub.elsevier.com/retrieve/pii/S0273117705010203.

[29] L.H. Ma. Gleissberg cycle of solar activity over the last 7000 years. *New Astronomy*, 14(1):1–3, jan 2009. ISSN 13841076. doi: 10.1016/j.newast.2008.04.001. URL https://linkinghub.elsevier.com/retrieve/pii/S1384107608000511.

[30] NASA. NASA Interstellar Probe Mission. URL http://interstellarprobe.jhuapl.edu/. [Accessed on: 2020-06-20].

[31] NASA. TSS-1R Mission Failure Investigation Board, Final Report. Technical report, 1996. URL https://core.ac.uk/download/pdf/42774798.pdf.

[32] NASA. A Little Physics and A Lot of String, 2000. URL https://science.nasa.gov/science-news/science-at-nasa/2000/ast09jun{_}1. [Accessed on: 2020-01-23].

[33] Mathew J. Owens and Robert J. Forsyth. The Heliospheric Magnetic Field. *Living Reviews in Solar Physics*, 10, 2013. ISSN 1614-4961. doi: 10.12942/lrsp-2013-5. URL http://link.springer.com/10.12942/lrsp-2013-5.

[34] E. N. Parker. Dynamics of the Interplanetary Gas and Magnetic Fields. *The Astrophysical Journal*, 128(8):664, nov 1958. ISSN 0004-637X. doi: 10.1086/146579. URL http://adsabs.harvard.edu/doi/10.1086/146579http://arxiv.org/abs/1011.1669http://dx.doi.org/10.1088/1751-8113/44/8/085201https://iopscience.iop.org/article/10.1088/1751-8113/44/8/085201.

[35] The Tether Physics. Tether Physics and Survivability (TiPS) Fact Sheet. Technical report, NRO, 1996. URL http://www.nro.gov/news/press/1996/1996-08.pdf.

[36] Christian Röken, Jens Kleimann, and Horst Fichtner. An Exact Analytical Solution For The Interstellar Magnetic Field In The Vicinity Of The Heliosphere. *The Astrophysical Journal*, 805(2):173, jun 2015. ISSN 1538-4357. doi: 10.1088/0004-637X/805/2/173. URL http://dx.doi.org/10.1088/0004-637X/805/2/173https://iopscience.iop.org/article/10.1088/0004-637X/805/2/173.

[37] Juan R. Sanmartin, Mario Charro, Enrico C. Lorenzini, and Henry B. Garrett. Electrodynamic Tether Microsats at the Giant Planets. Technical report, Universidad Politécnica de Madrid, 2006.

[38] Juan R. Sanmartin, Mario Charro, Enrico C. Lorenzini, Henry B. Garrett, Claudio Bombardelli, and Cristina Bramanti. Electrodynamic tether at jupiter - II: Fast moon tour after capture. *IEEE Transactions on Plasma Science*, 37(4 PART 2):620–626, 2009. ISSN 00933813. doi: 10.1109/TPS.2009.2013955.

[39] Maximilian M. Schadegg, Ryan P. Russell, and Gregory Lantoine. Jovian orbit capture and eccentricity reduction using electrodynamic tether propulsion. *Journal of Spacecraft and Rockets*, 52(2):506–516, 2015. ISSN 00224650. doi: 10.2514/1.A32962.

[40] Shizuoka University and M Nohmi. Initial Orbital Performance Result of Nano-Satellite STARS-II. In *Proceedings of the International Symposium on Artificial Intelligence, RObotics and Automation in Space (I-SAIRAS)*, 2014.

[41] O. Sternal, N. E. Engelbrecht, R. A. Burger, S. E. S. Ferreira, H. Fichtner, B. Heber, A. Kopp, M. S. Potgieter, and K. Scherer. Possible Evidence For A Fisk-Type Heliospheric Magnetic Field. *The Astrophysical Journal*, 741(1):23, nov 2011. ISSN 0004-637X. doi: 10.1088/0004-637X/741/1/23. URL https://iopscience.iop.org/article/10.1088/0004-637X/741/1/23.

[42] N.H. Stone, W.J. Raitt, and K.H. Wright. The TSS-1R electrodynamic tether experiment: Scientific and technological results. *Advances in Space Research*, 24(8):1037–1045, jan 1999. ISSN 02731177. doi: 10.1016/S0273-1177(99)00551-7. URL https://linkinghub.elsevier.com/retrieve/pii/S0273117799005517.

[43] TEMA 19. Slingshots and Space Shots. page 6, may 2005. URL http://www.ams.org/publicoutreach/feature-column/fcarc-slingshot.

[44] TU Delft. Tudat Documentation - Earth Mars Transfer, . URL https://tudat.tudelft.nl/tutorials/applicationWalkthroughs/earthMarsTrans.html. [Accessed on: 2020-07-02].

[45] TU Delft. Tudat Documentation - Integrators, . URL https://tudat.tudelft.nl/tutorials/tudatFeatures/mathTools/integrators.html. [Accessed on: 2020-07-02].

[46] Matthew Turnock. Deep Space Propulsion With Electromagnetic Tethers, A Literature Study, TU Delft. 2020.

[47] Atsuko Uchida and Masahiro Nohmi. Stars-Ii Mission Design for Space Experiment of Tethered Robotic System. In *I-SAIRAS*, number September, pages 2–5, Turin, Italy, 2012.

[48] Karel F. Wakker. *Fundamentals of Astrodynamics*. TU Delft, Delft, 2015. ISBN 9789461864192.

[49] Takeo Watanabe, Hironori A Fujii, Hironori Sahara, Takuji Ebinuma, and Hirohisa Kojima. [Special Issue of In-Space Flight Experiments of Electrodynamic Tether] Deployment of Bare Electro-Dynamic Tape Tether on Sounding Rocket S520-25. *Aerospace Technology Japan, The Japan Society For Aeronautical And Space Sciences*, 11:1–6, 2012. ISSN 1884-0477. doi: 10.2322/astj.11.1. URL http://joi.jlc.jst.go.jp/JST.JSTAGE/astj/11.1?from=CrossRef.

[50] Wikipedia. CowellPropagator, . URL `https://commons.wikimedia.org/wiki/File:Cowells{_}method.png`. [Accessed on: 2021-06-20].

[51] Wikipedia. Ultimate Tensile Strength, . URL `https://en.wikipedia.org/wiki/Ultimate{_}tensile{_}strength{#}cite{_}note-15`. [Accessed on: 2020-01-24].

[52] Wikipedia. Heliocentric Reference Frame, . URL `https://commons.wikimedia.org/wiki/File:Heliocentric{_}rectangular{_}ecliptic.png`. [Accessed on: 2021-06-20].

[53] Paul Williams, Steven Tragesser, and Wubbo Ockels. Orbital Maneuvering with Spinning Electrodynamic Tethers. *Advances in the Astronautical Sciences*, 134:2177–2196, 2009. ISSN 00653438.

[54] Z. H. Zhu and Rui Zhong. Deorbiting Dynamics of Electrodynamic Tether. *International Journal of Aerospace and Lightweight Structures (IJALS)*, 01(01):47, 2011. ISSN 2010-4286. doi: 10.3850/2010428611000043. URL `http://rpsonline.com.sg/journals/102-ijals/2011/0101/S2010428611000043.xml`.

[55] E. J. Zirnstein, J. Heerikhuisen, H. O. Funsten, G. Livadiotis, D. J. McComas, and N. V. Pogorelov. Local Interstellar Magnetic Field Determined From The Interstellar Boundary Explorer Ribbon. *The Astrophysical Journal*, 818 (1):L18, feb 2016. ISSN 2041-8213. doi: 10.3847/2041-8205/818/1/L18. URL `http://dx.doi.org/10.3847/2041-8205/818/1/L18https://iopscience.iop.org/article/10.3847/2041-8205/818/1/L18`.